Molecular Simulation Study of Transport and Separation of Gas through Nanoporous Graphene Membranes

Juncheng Guo

University of Pau et des Pays de l'Adour-Ecole Doctorale des Sciences Exactes et leurs Applications

THESIS
Molecular Simulation Study of Transport and Separation of Gas through Nanoporous Graphene Membranes

presented by

Juncheng GUO

for the degree of Doctor of Philosophy

Petroleum Engineering

Defense Date : 17/12/2020

Reporters

Laurent Joly PR / University of Lyon 1

Jean-Marc Simon MC HDR / University of Bourgogne

Examiners

Ania Conchi DR / CNRS

Benjamin Rotenberg DR / CNRS-University of Sorbonne

Germain Vallverdu MC / IPREM-UPPA

Directors of thesis

Guillaume Galliero PR / LFCR-UPPA

Romain Vermorel MC / LFCR-UPPA

Table of Contents

List of Figures

List of Tables

Acknowledgment

This thesis work was carried out in the "Thermophysical Properties" research team of the Laboratoire des Fluides Complexes et leurs Réservoirs (LFCR) at the Université de Pau et des Pays de l'Adour.

I would first like to thank Laurent JOLY and Jean-Marc SIMON who have honored me by accepting to be the reporters of this thesis. Also, I thank Ania CONCHI, Benjamin ROTENBERG and Germain VALLVERDU for having accepted to examine this work and to be part of the defense jury.

I would especially like to thank my thesis directors, Guillaume GALLIERO and Romain VERMOREL, for their supervision, their availability, the advice and such a precious experience they have given me throughout these years of thesis. My thanks also gives to Hai Hoang, for his useful help in my work.

It is also an opportunity for me to thank all my colleagues and friends that I have met during these years of thesis: Abdoul, Mohamed, Ezequiel, Deneb, Bich Ngoc, Dihya, Daoud, Samy, Nelson, Patrick, Amael, Catherine, Véronique, Blandine, Patricia, Sophie, Djamel, Jean-Patrick, Karzyna, Kristina, Xin, José, Sujun, Chengyi, Jingyi, Huiting, Xingtong, Shuaiqian, Huaiyuan, Wanqing.

Finally, my most sincere thanks go to all my family, and in particular my parents, for the sacrifices they made and all the values they instilled in me: this thesis work is especially dedicated to them!

Abstract

In this work, we show that gas permeation through single-layer nanoporous graphene membranes can be divided into three regimes: molecular sieving, crossover regime and effusion. Currently, most of the researches focus on the molecular sieving regime and the analytical frameworks are expressed using Arrhenius-type equations. Nevertheless, we show that Arrhenius-type equations are too simple to predict the diffusive transport coefficient correctly. Thus, we propose a theoretical framework to explain the mechanisms and predict the diffusive transport coefficient over the whole range of permeation regimes. In our framework, the transport coefficient is related to parameters which can be computed from the potential of mean force (PMF) between permeating gas molecules and the membrane atoms. By means of Equilibrium (EMD) and Non Equilibrium (NEMD) molecular dynamics simulations, we explore the permeation of pure compounds through nanoporous graphene membranes exhibiting different pore sizes and geometry. We also investigate the effect of thermodynamic conditions (pressure and temperature) on the transport coefficient. Simulated transport coefficients are in good agreement with the predictions of our theory over the whole range of permeation regimes. Furthermore, based on the knowledge acquired on the permeation of pure compounds, we explore the relation with the selectivity concept in mixtures. By comparing the results of molecular simulations performed with gas mixtures, we show in which cases the results we obtained for pure compounds, and consequently our theoretical framework, allow us to predict the selectivity of mixtures.

Key words: gas permeation, separation, nanoporous graphene, molecular simulation

Résumé

Dans ce travail, nous montrons que la perméation des gaz à travers les membranes de graphène nanoporeux mono-couche peut être divisée en trois régimes : le tamisage moléculaire, un régime de transition et le régime d'effusion. Actuellement, la plupart des recherches se concentrent sur le régime de tamisage moléculaire et les cadres analytiques sont exprimés à l'aide d'équations de type Arrhenius. Néanmoins, nous montrons que les équations de type Arrhenius sont trop simples pour prédire correctement le coefficient de transport diffusif. Donc, nous proposons un cadre théorique pour expliquer les mécanismes et prédire le coefficient de transport diffusif pour tous les régimes de perméation. Dans notre formalisme théorique, le coefficient de transport est lié aux paramètres qui peuvent être calculés à partir du potentiel de force moyenne (PMF) entre les molécules de gaz diffusantes et les atomes de la membrane. Au moyen de simulations de dynamique moléculaire en équilibre (EMD) et en non-équilibre (NEMD), nous explorons la perméance de composés purs à travers des membranes de graphène nanoporeux présentant des pores de taille et de géométrie différentes. Nous étudions également l'effet des conditions thermodynamiques (pression et température) sur le coefficient de transport. Les coefficients de transport simulés sont en bon accord avec les prédictions de notre théorie et ce pour tous les régimes de perméation. En outre, sur la base des connaissances acquises sur la perméance des composés purs, nous explorons la relation avec le concept de sélectivité dans les mélanges. En comparant les résultats des simulations moléculaires réalisées avec des mélanges de gaz, nous montrons dans quels cas les résultats obtenus pour les composés purs, et par conséquent notre cadre théorique, nous permettent de prédire la sélectivité des mélanges.

Mots clés: perméance de gaz, séparation, graphène nanoporeux, simulation moléculaire

Introduction

0.1 État de l'art du processus de séparation des gaz

La séparation des gaz est une technique largement utilisée dont l'objectif est la séparation d'un ou plusieurs gaz d'un mélange. Elle est cruciale pour plusieurs procédés industriels tels que le traitement des fumées des centrales à charbon, visant notamment à filtrer le CO_2 pour réduire l'effet de serre. Les procédés concernés, comme la distillation, représentent 10 à 15 % de la consommation mondiale d'énergie[2]. Un intérêt croissant est également accordé à d'autres applications telles que la séparation et la purification de gaz à valeur commerciale comme le CH_4 ou même le H_2 et le He contenus dans le gaz naturel. Dans cette section, nous présentons les trois méthodes les plus courantes pour effectuer la séparation des gaz :

- Séparation par distillation cryogénique
- Séparation par absorption/adsorption
- Séparation avec les membranes

Parmi ces méthodes, la séparation par distillation cryogénique est la plus utilisée dans l'industrie de la séparation de l'air. Cependant, elle est basée sur la transition de phase, entrainant une grande consommation d'énergie et par conséquent des émissions de CO_2. Dans l'industrie pétrolière et gazière, le marché mondial de la séparation était évalué à 7 milliards de dollars en 2017 et devrait atteindre 14 milliards en 2025, avec un TCAC (taux de croissance annuel composé) de 4,6 % entre 2017 et 2025. Il est donc important de développer des technologies de séparation qui soient à la fois économiques et pratiques. Malheureusement, les alternatives à la distillation, telles que la séparation des molécules en fonction de leurs propriétés chimiques ou de leur taille, sont peu développées ou coûteuses à mettre en œuvre.

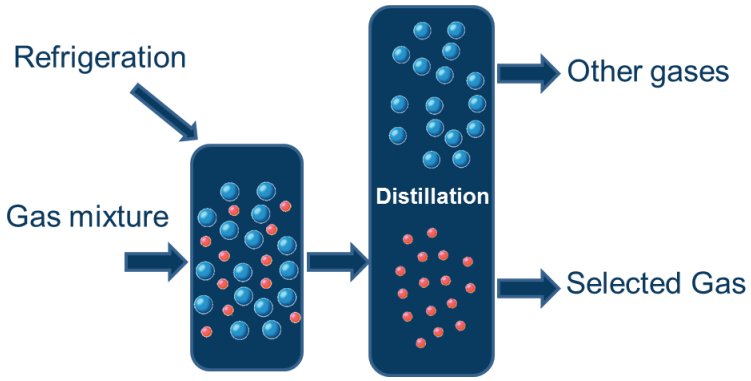

Figure 1: Représentation schématique de la distillation cryogénique[1].

0.1.1 Séparation par distillation cryogénique

La distillation cryogénique est basée sur le fait que dans un mélange de gaz, les composants ont tous des points d'ébullition différents et qu'ils pourraient être séparés en diminuant/augmentant la température et la pression du système dans lequel ils sont stockés[1]. Le mélange gazeux est refroidi à une basse température. Une fois sous forme liquide, les composants du gaz peuvent être dirigés dans une colonne de distillation et, par une série d'étapes de compression, de refroidissement et d'expansion, ils peuvent être distribués dans différents canaux, en fonction de leur point d'ébullition[3]. Au siècle dernier, la distillation est devenue le procédé de séparation dominant à l'échelle industrielle suite au développement des industries pétrolières et chimiques. Aujourd'hui, la distillation s'effectue principalement en continu (Figure 1.1) dans des colonnes/tours creuses verticales, avec les tuyauteries, les échangeurs de chaleur, les pompes, les cuves de stockage, les structures de support associées[4, 5, 6]. Compte tenu des flux de produits et d'alimentation, la séparation par distillation nécessite une diminution de l'entropie et ne peut donc pas se produire spontanément[7]. Par conséquent, l'ajout de chaleur est utilisé dans la pratique pour rendre ce processus possible sur le plan thermodynamique. Par conséquent, l'efficacité globale de la distillation est plutôt faible en raison des pertes irréversibles liées à la chute de pression, au transfert de masse (par exemple, le mélange après séparation) et au transfert de chaleur[8, 9, 10].

Actuellement, la distillation est la méthode de séparation la plus utilisée à l'échelle industrielle, avec plus de 40 000 colonnes en service dans le monde. C'est une technique largement utilisée pour les flux qui ont déjà une concentration élevée en gaz souhaité (généralement plus de 90 %), mais elle n'est pas très appropriée pour les flux de gaz plus dilués.

À l'heure actuelle, le principal mode de transport du gaz naturel est en phase liquide. Le

principal avantage de la séparation cryogénique du gaz est donc de permettre la production directe de gaz liquide. Un inconvénient majeur est lié à la grande quantité d'énergie nécessaire pour la réfrigération, en particulier pour les flux de gaz dilués. Pour améliorer la méthode de distillation cryogénique, plusieurs développements de la distillation visant à résoudre les problèmes liés aux coûts élevés d'investissement et d'exploitation sont en cours d'étude : utilisation d'autres sources d'énergie (par exemple l'énergie solaire)[11], combinaison de la distillation avec la réaction ou d'autres séparations (séparation par membrane ou distillation)[12], utilisation d'un mode de fonctionnement différent basé sur le mouvement séparé des phases pour augmenter l'efficacité de la séparation, ou intégration de plus de fonctions dans une seule unité de fonctionnement[6].

0.1.2 Séparation par absorption/adsorption

La séparation par absorption/adsorption est basée sur l'affinité du gaz pour un absorbant/adsorbant spécifique. Pour le processus d'absorption, une variété de solvants liquides est utilisée comme absorbants pour éliminer un gaz spécifique des flux de mélange gazeux. De cette façon, le processus d'absorption peut généralement être divisé en catégories chimiques et physiques. Les processus dans lesquels le solvant réagit chimiquement avec le gaz dissous sont appelés processus d'absorption chimique.

Les processus d'absorption physique sont des processus dans lesquels le solvant n'interagit physiquement qu'avec le gaz dissous. Ici, un solvant est utilisé comme absorbant avec des propriétés thermodynamiques telles que l'absorption relative d'un gaz spécifique est favorisée par rapport aux autres composants du mélange gazeux. Ce type de technologie est souvent utilisé dans le processus de capture de CO_2 en postcombustion[14]. Dans de nombreuses applications industrielles, des combinaisons de solvants physiques et de solvants réactifs peuvent être utilisées en tandem. Cependant, dans tous les cas, le recyclage des solvants est une activité gourmande en énergie et couteuse.

L'adsorption est le nom du phénomène spontané d'attraction qu'une molécule d'une phase fluide subit lorsqu'elle est proche de la surface d'un solide, appelé adsorbant[15, 16, 17, 18, 19]. Par rapport à l'absorbant, l'adsorbant est un solide poreux, ayant de préférence une grande surface de pores par unité de masse[20]. Dans le processus d'adsorption, le flux d'alimentation est mis en contact avec l'adsorbant qui est normalement placé dans des lits fixes. Le composant (léger) le moins adsorbé traversera la colonne plus rapidement que les autres [21, 22, 23, 24, 25]. Afin de réaliser la séparation, avant que les autres composants (lourds) ne traversent la colonne, l'alimentation doit être arrêtée et l'adsorbant doit être régénéré en désorbant les composés lourds. Comme l'équilibre d'adsorption est donné par des conditions de fonctionnement spécifiques

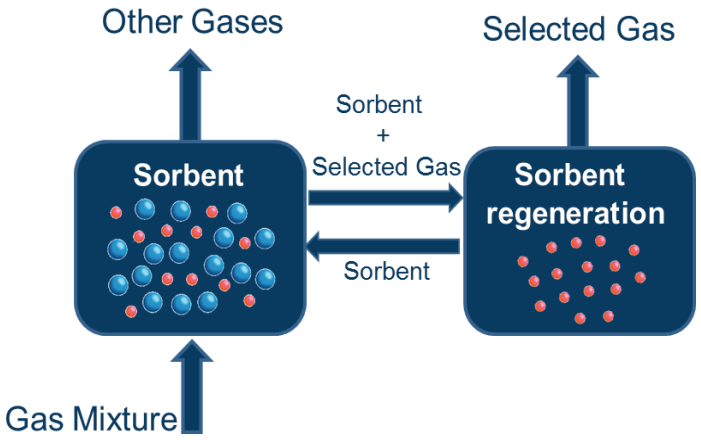

Figure 2: Représentation schématique du procédé dit de Pressure Swing Adsorption[1].

(composition, T et P), en modifiant l'un de ces paramètres du procédé, il est possible de régénérer l'adsorbant. Dans le procédé de séparation des gaz industriels, trois techniques sont utilisées :

- Adsorption à pression alternée : L'adsorption à pression alternée (Pressure swing adsorption - PSA) met sous pression et dépressurise le gaz autour d'un support adsorbant pour adsorber sélectivement certains composants d'un gaz, permettant d'en éliminer d'autres de manière sélective.

- Adsorption alternée sous vide : L'adsorption modulée par le vide (VSA) utilise le même principe que la PSA mais oscille entre les pressions du vide et la pression atmosphérique. Les deux techniques peuvent être combinées et sont appelées dans ce cas "Adsorption à pression alternée sous vide" (VPSA).

- Adsorption à température alternée : L'adsorption modulée en température (TSA) utilise une technique similaire aux autres techniques d'adsorption modulée, mais elle fait varier la température plutôt que la pression.

Lorsque la régénération de l'adsorbant est effectuée en réduisant la pression totale du système, processus appelé adsorption modulée en pression (AMP), la pression totale du système oscille entre la haute pression d'alimentation et la basse pression de régénération. La technologie PSA est utilisée dans la plus grande variété d'applications, telles que la purification de l'hydrogène[29, 30], l'extraction de CO_2 [31, 32, 33], la séparation de l'air[34, 35] et la production de gaz naturel[36, 37, 38]. Les principaux avantages de cette technique sont la grande pureté du gaz séparé, tandis que

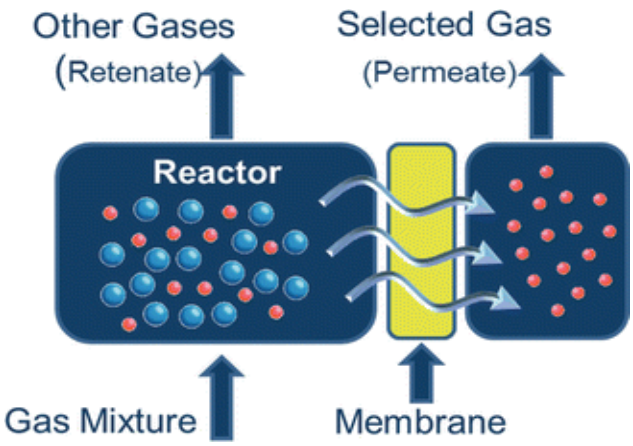

Figure 3: Représentation schématique de la séparation de gaz par membrane[1].

l'inconvénient consiste en la grande énergie nécessaire au fonctionnement du système, notamment pour la régénération des adsorbants.

0.1.3 Séparation avec les membranes

La séparation des gaz avec les membranes repose sur les différentes affinités d'un ou de plusieurs gaz envers le matériau de la membrane, ce qui fait qu'un gaz pénètre plus rapidement (ou plus lentement) que les autres. La science et la technologie des membranes sont aujourd'hui reconnues comme des outils puissants pour résoudre certains problèmes mondiaux importants, en développant de nouveaux procédés industriels nécessaires à une croissance industrielle durable. Au cours des dernières années, les membranes dites perm-sélectives, qui présentent des perméabilités différentes pour différentes espèces chimiques, suscitent de plus en plus d'intérêt dans le processus de séparation des gaz. En concurrence avec des procédés classiques telles que l'absorption à pression alternée et la distillation cryogénique, le développement des membranes perm-sélectives vise à réduire les coûts de production mais aussi la taille des équipements, l'utilisation de l'énergie et la production de déchets[40].

Contrairement aux autres procédés de séparation classiques, la séparation des gaz par membrane ne nécessite pas de changement de phase. Le processus est illustré dans la figure 1.3. Le mélange gazeux est dirigé dans un récipient et mis en contact avec le matériau de la membrane qui se trouve à l'interface avec un autre récipient. On laisse le mélange se diffuser dans le deuxième récipient sous l'effet d'un gradient de pression qui favorise le transport de masse à travers la membrane séparant le rétentat (gaz plus lent) du perméat (gaz plus rapide). Le mécanisme de séparation des gaz avec la membrane est basé sur le mécanisme de transport par diffusion. Presque

tous les procédés de séparation de gaz avec membrane ont le même mécanisme : l'adsorption du gaz dans la membrane, la perméation par diffusion à travers la membrane et la désorption du côté basse pression de la membrane[39].

L'utilisation de la membrane dans les procédés de séparation se développe à un rythme lent mais régulier. Au cours des 20 dernières années, les ventes d'équipements de séparation des gaz par membrane ont augmenté pour atteindre 150 millions de dollars par an et plus de 90 % de cette activité concerne la séparation de gaz non condensables[41]. On s'attend à ce que la séparation des gaz par membrane joue un rôle de plus en plus important dans la réduction de l'impact environnemental et des coûts des processus industriels[42]. L'utilisation de membranes pour la séparation des gaz offre plusieurs avantages, le plus précieux étant probablement le rapport coût-efficacité élevé (tant pour la simplicité mécanique du système que pour la régénération à faible énergie). En fait, elles ne nécessitent pas de régénération thermique, de changement de phase ou de pièces mobiles actives dans leur fonctionnement. En outre, l'absence de pièces mobiles rend les systèmes de séparation des gaz particulièrement adaptés à une utilisation dans des endroits difficiles d'accès où la fiabilité est essentielle ; de plus, leur faible encombrement les rend très attrayantes pour les applications telles que les plateformes de traitement de gaz en mer[43].

La plus grande limitation des membranes pour la séparation des gaz provient probablement du compromis entre perméabilité et sélectivité pour un composant gazeux requis. La perméabilité caractérise la vitesse à laquelle un composé quelconque traverse une membrane, toujours exprimée par la définition de la perméance en unités de $mol\ Pa^{-1}\ s^{-1}$[44]. La sélectivité est la capacité d'une membrane à accomplir une séparation donnée. Elle est généralement décrite comme le rapport des perméabilités pour une paire de gaz donnée. La relation de compromis signifie que les membranes hautement perméables ont une faible sélectivité, nécessitant plusieurs passages pour une bonne séparation, et que les membranes hautement sélectives ont une faible perméabilité, ce qui signifie de longues périodes de fonctionnement. Ce compromis a été bien décrit par Robeson dans plusieurs articles[45, 46]. La séparation des gaz par membrane a le potentiel de se développer énormément si nous pouvons trouver des matériaux membranaires plus sélectifs. Une variété de matériaux dont la membrane pourrait être composée sont disponibles, comprenant les MOF[i][47, 48], les polymères[49, 50], les zeolites[51, 52] et les matériaux à base de carbone[53, 54, 55].

La figure 1.4 montre les résultats des tracés de Robeson pour la séparation de paires de gaz CO_2/CH_4 avec différents matériaux de membrane. Il est à noter que la membrane de graphène nanoporeux a le potentiel de dépasser la limite supérieure des autres matériaux. De plus amples détails sur le graphène nanoporeux seront présentés dans la prochaine section.

[i]Metal Organic Framework

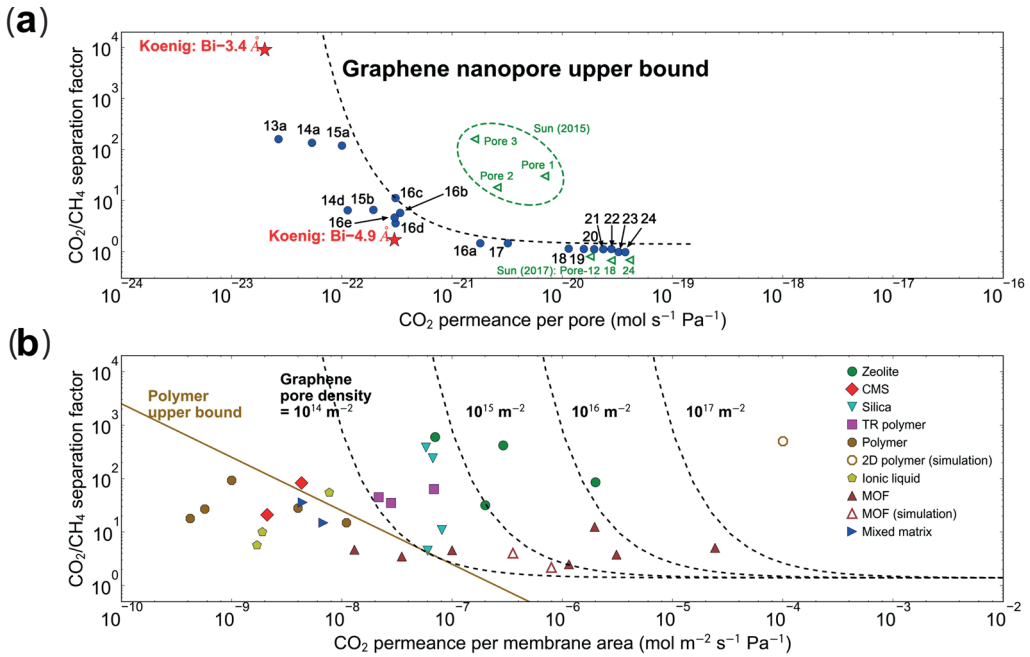

Figure 4: (a) Graphique de Robeson (facteur de séparation vs perméance par pore) caractérisant la séparation CO_2/CH_4 à travers divers pores sub-nanométriques en graphène à 300 K. (b) Comparaison entre une membrane en graphène poreux et d'autres membranes pour les séparations CO_2/CH_4[44].

0.2 Le matériau graphène nanoporeux

L'isolement du graphène a été réalisé pour la première fois par Geim et al. en 2004 par l'exfoliation mécanique du graphite[57]. L'Académie royale des sciences de Suède a décidé d'attribuer le prix Nobel de physique en 2010 à Andre Geim et Konstantin Novoselov, "pour des expériences révolutionnaires concernant le graphène bidimensionnel". Le graphène est une feuille 2D dense composée d'atomes de carbone hybrides sp^2 disposés en un réseau en nid d'abeille, formant deux sous-réseaux équivalents d'atomes de carbone liés entre eux par une liaison σ, et chaque atome de carbone du réseau a une orbite π qui contribue à un réseau délocalisé d'électrons[58, 59, 60, 57]. Avec sa faible épaisseur atomique, le graphène est considéré comme le matériau carboné le plus important de ces dernières décennies. Il présente un fort effet de champ électrique ambipolaire avec une densité de porteurs de charge allant jusqu'à $10^{13} cm^2$[61]. La mobilité électronique à température ambiante d'une feuille de graphène peut dépasser 200 000 $cm^2 V^{-1} s^{-1}$, comme à l'état suspendu ou en charge sur un substrat approprié[57, 62, 63]. En même temps, il possède une grande surface spécifique théorique ($2630 m^2 g^{-1}$), d'excellentes résistance mécanique et stabilité chimique[57, 64, 65].

Comme nous l'avons vu dans la section précédente, la technique des membranes gagne en importance dans le processus de séparation, où le paramètre le plus important de cette technique est le matériau poreux utilisé. Avec ses caractéristiques, le graphène a le potentiel d'être l'un des matériaux poreux les plus performants. Une feuille de graphène vierge est parfaitement imperméable, même aux plus petites molécules, comme l'hélium[66], il est donc essentiel de générer des nanopores pour permettre les applications en tant que matériau poreux. Avec la génération de nanopores, les matériaux en graphène nanoporeux ont reçu une attention considérable dans les applications universitaires et industrielles[56], comme le montre la figure 1.5.

0.2.1 Synthèse du graphène nanoporeux

Dans les études expérimentales, de nombreuses méthodes, outre l'exfoliation mécanique, ont été développées pour isoler la feuille de graphène à couche unique. Par exemple, la croissance épitaxiale sur des substrats[67] tels que SiO_2, le dépôt de couche atomique ou le dépôt chimique en phase vapeur[68], et l'oxydation thermique du graphite[69] permettent de produire du graphène vierge à grande échelle et de haute qualité.

Ces dernières années, de nombreuses expériences ont été menées pour générer des nanopores dans une seule couche de graphène. Les méthodes les plus utilisées comprennent à la fois des méthodes physiques, telles que l'ablation par faisceau d'électrons focalisés[70, 71], l'irradiation par faisceau d'ions focalisés[72], la gravure oxydative induite par ultraviolets[73], le bombardement

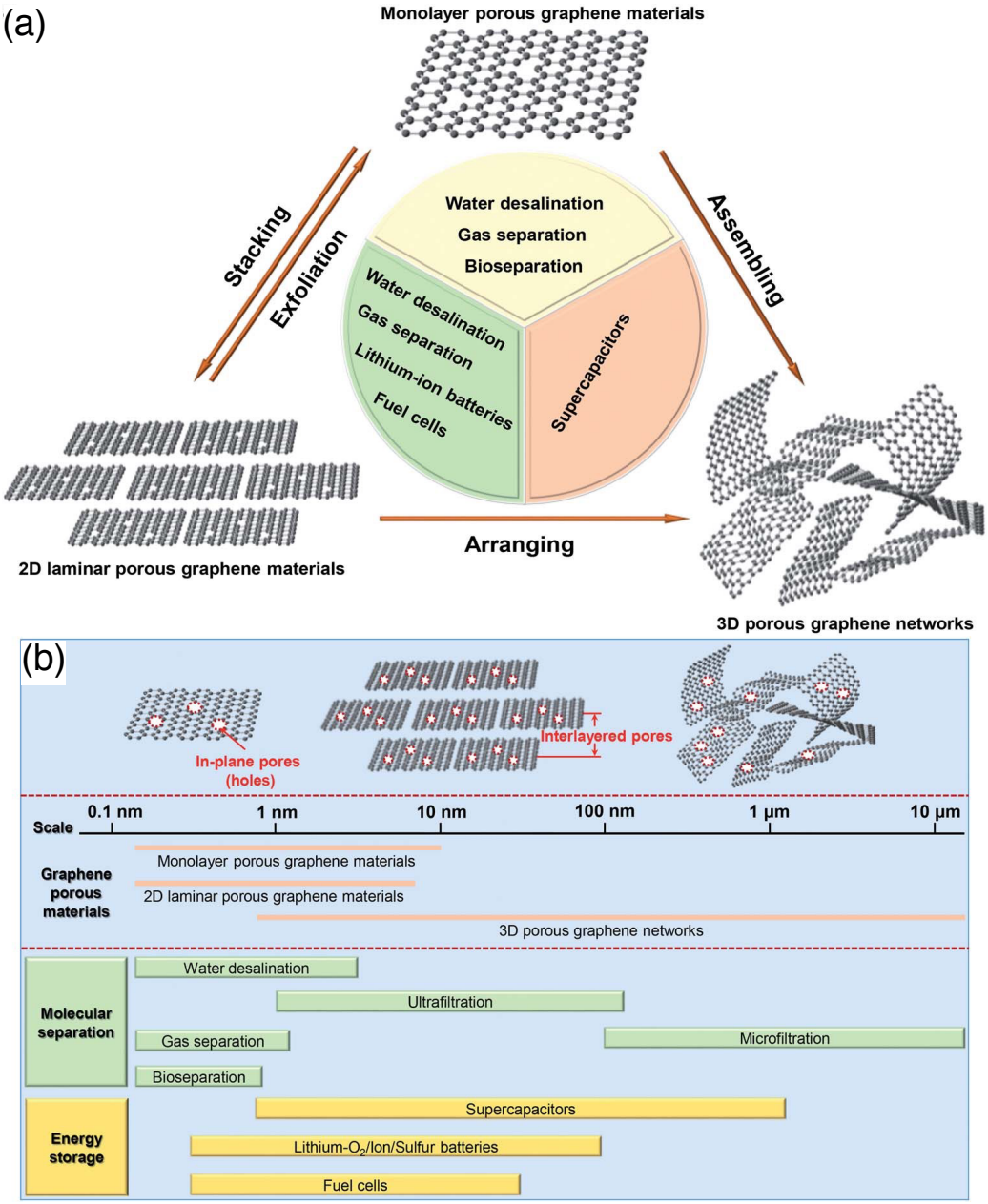

Figure 5: (a) Matériaux à base de graphène nanoporeux et leurs applications. (b) Classification des matériaux à base de graphène nanoporeux, définition des pores dans le plan et des pores inter-feuillets dans les matériaux à base de graphène nanoporeux et leurs applications en fonction de la taille des pores[56].

ionique suivi d'une gravure oxydative[74], la gravure par plasma d'oxygène[75], et des méthodes chimiques, telles que le couplage aryle-aryle[76] et la gravure MnO_2[77]. Selon les techniques de production utilisées, la taille des pores (le diamètre des pores) s'étend de la précision atomique à l'échelle du nanomètre. En raison des pores dans le plan du graphène, le graphène poreux présente des propriétés distinctes de celles du graphène vierge, ce qui ouvre la porte à de nombreuses applications.

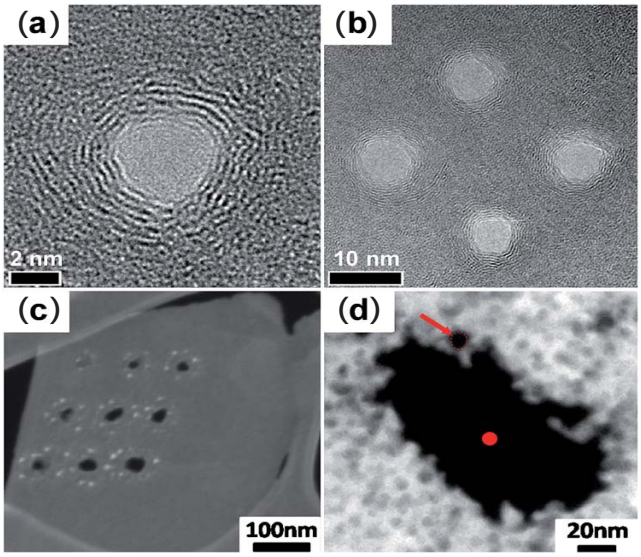

Figure 6: (a) Image des nanopores générés par un faisceau d'électrons focalisé dans le graphène. (b) Multiples nanopores réalisés à proximité les uns des autres par faisceau d'électrons focalisés[70]. (c) Image de neuf trous gravés dans un flocon de graphène. (d) Image de perte d'énergie par plasma avec contraste de l'épaisseur du matériau, le point au centre du trou indique le diamètre nominal du faisceau d'électrons utilisé pour graver le trou (environ 5,9 nm)[71]

.

Dans le tableau 1.1, nous résumons les différentes méthodes pour générer des nanopores dans le graphène et dans la figure 1.6, nous montrons les images de nanopores générés par ces méthodes. En fonction des exigences en matière d'applications scientifiques, différentes méthodes peuvent être utilisées. Néanmoins, parmi ces méthodes, la taille des pores et la distribution des formes ne sont pas encore bien caractérisées dans les échantillons synthétisés. En ce qui concerne les applications industrielles réelles, l'extensibilité à des processus de plus grande échelle semble être un problème.

Méthodes	Taille des pores (nm)	Surface (μm^2)	Densité	Avantages	Limitations
Irradiation par faisceau d'électrons focalisé[70]	3.5	n/a	n/a	Tunable et taille de pore bien définie	Petite surface
Irradiation par faisceau d'électrons assistée par l'azote[71]	5.9	n/a	n/a	Taille des pores contrôlée	Petite surface
Gravure oxydative induite par les ultraviolets[73]	0,4-10	19,63	n/a	Echantillons de grande surface	Large distribution de taille
Bombardement ionique et gravure chimique oxydative[74]	0,4	n/a	n/a	Grande surface, taille de pore contrôlée	densité de pore modérée
Irradiation par faisceau d'ions focalisés[72]	5-100	12,57	10^3-10^6 par membrane	Taille de pore accordable et bien définie	Petite surface
Gravure au plasma d'oxygène[75]	1	12.57	$1/100nm^2$	Echantillons de grande surface, taille de pore accordable	Densité de pore modérée
Couplage aryle-aryle assisté en surface du bloc conçu[76]	0,4	n/a	n/a	Simple, rentable	Difficile à transférer
MnO_2 etching[77]	2.4	n/a	n/a	Simple	Difficile de contrôler la taille des pores

Table 1: Résumé des différentes méthodes de pointe pour la génération de nanopores dans le graphène.

0.2.2 Avantages du graphène nanoporeux dans le procédé de séparation des gaz

Le graphène nanoporeux peut être considéré comme l'un des matériaux membranaires les plus performants dans le processus de séparation des gaz. Comme nous l'avons présenté dans la section précédente, le procédé membranaire présente plusieurs avantages, notamment des coûts énergétiques plus faibles, un investissement en capital moins important et une complexité mécanique moindre[39]. En outre, le graphène nanoporeux est un excellent matériau de départ pour le développement de nouvelles membranes, avec ses avantages spécifiques[78, 79] :

- La haute résistance mécanique du graphène peut assurer la stabilité du réseau de pores.
- Les importantes stabilités chimiques et thermiques du graphène permettent à ce matériau poreux de résister à des environnements extrêmes.
- Les nanopores permettent le passage de petites molécules et bloquent les plus grosses molécules afin d'assurer une haute sélectivité.
- L'épaisseur atomique de la membrane permet de consommer moins d'énergie pour maintenir le flux et elle est adaptée à la diffusion rapide des ions et des molécules.

Sheng et al. ont d'abord proposé l'utilisation de graphène nanoporeux comme membrane atomique mince, très efficace et sélective pour la séparation des gaz[80]. Les autres études ont également prédit que le graphène nanoporeux peut être appliqué pour la purification du méthane[81], et la séparation de CO_2/N_2[82] ou H_2/N_2[83]. Certains chercheurs tels que Hauser, Schrier et Schwerdtfeger ont même suggéré que le graphène nanoporeux peut être utilisé pour séparer les isotopes He^3/He^4[84, 85]. Dans des études expérimentales, Koenig et al. ont utilisé le graphène nanoporeux comme tamis moléculaire[73]. Une ampoule pressurisée et une résonance mécanique ont été utilisées pour mesurer le transport de divers gaz (H_2, CO_2, Ar, N_2, CH_4 et SF_6) à travers les pores. Comme prévu, le graphène nanoporeux a montré une sélectivité moléculaire et les taux de fuite mesurés ont diminué avec l'augmentation des tailles moléculaires, ce qui correspond bien aux modèles basés sur la diffusion moléculaire à travers des pores de la taille de quelques angström[73].

0.3 Motivations et plan de la thèse

0.3.1 Motivations

Comme nous l'avons présenté, le graphène nanoporeux est un matériau intéressant pour concevoir des membranes pour le processus de séparation des gaz. La production à grande échelle de feuilles de graphène nanoporeux à pores contrôlés est attendue dans un futur proche. En ce qui concerne les études expérimentales, nous avons mis en lumière les difficultés à évaluer la taille et la forme des pores et leur influence sur les propriétés de transport et de séparation mesurées. Néanmoins, en raison des progrès réalisés en matière de puissance de calcul et de précision des champs de force, les simulations moléculaires peuvent être considérées comme un complément aux études expérimentales.

Afin d'obtenir une grande sélectivité pour la séparation des gaz, le diamètre des pores doit être proche du diamètre cinétique des molécules de gaz. Pour décider de la taille de pore appropriée et guider la conception des pores, de nombreux auteurs ont réalisé un travail considérable pour calculer le coefficient de transport et la sélectivité du gaz par des simulations de dynamique moléculaire (MD). Yuan et al[44] ont démontré une relation de compromis entre la perméabilité et la sélectivité d'une paire de gaz donnée, montrant que le graphène nanoporeux a le potentiel de dépasser la limite supérieure de Robeson lorsque la densité surfacique de pores est suffisamment importante. Ainsi, d'une part, un cadre théorique est nécessaire pour prédire le coefficient de transport et obtenir une prédiction quantitative de la sélectivité. D'autre part, il n'existe pas de compréhension précise et universelle de l'impact de paramètres tels que la taille et la géométrie des pores, la densité du gaz et la température sur le transport et la séparation du gaz.

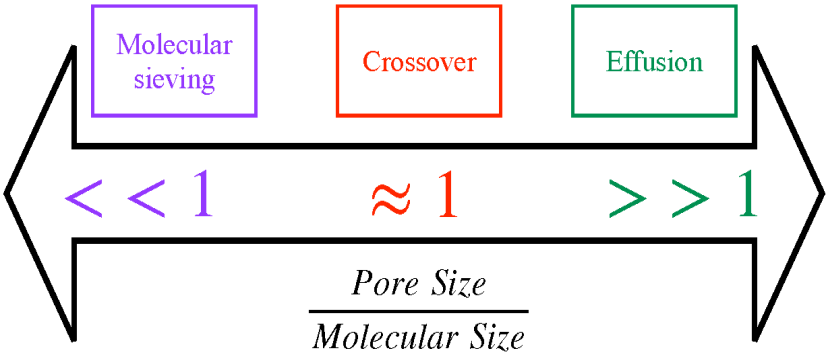

Figure 7: Régime de diffusion moléculaire selon le rapport entre la taille des pores et la taille moléculaire

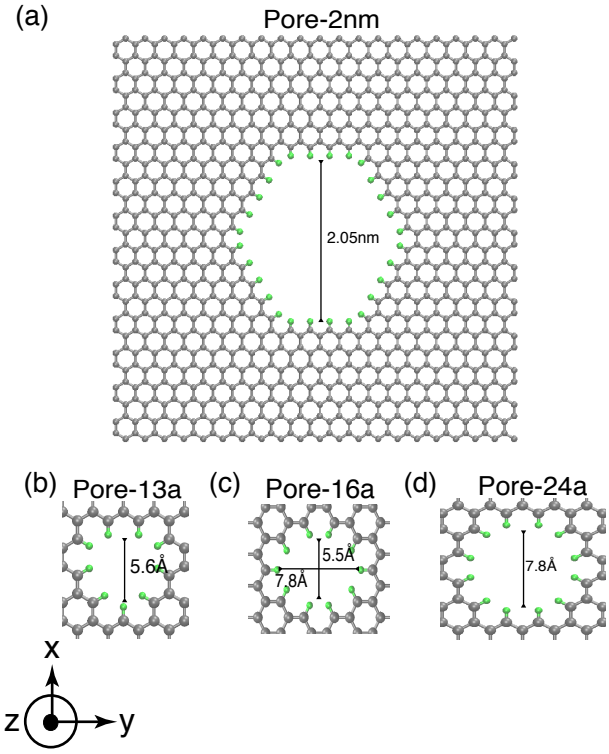

Figure 8: Zoom en vue du Pore-2nm (a), Pore-13a (b), Pore-16a (c), Pore-24a (d) dans le plan $xy - plane$

Sur la base du rapport entre la taille des pores et la taille moléculaire, le régime de perméation des gaz peut être divisé en trois régimes. Comme le montre la figure 1.7, le régime de perméation des gaz évolue continuellement du tamisage moléculaire[86] (taille des pores $<$ taille moléculaire), pour lequel le franchissement des barrières d'énergie libre contrôle le flux, à l'effusion[87] (taille des pores $>>$ taille moléculaire), pour lequel on observe un flux moléculaire libre. Entre ces deux régimes, le mécanisme de perméation est également influencé par la cinétique d'adsorption/désorption dans le pore, car les barrières d'énergie libre répulsives sont moins prononcées et le pore n'est pas assez grand pour empêcher les molécules de gaz diffusantes d'interagir avec les atomes de la membrane. Nous appelons ce régime d'écoulement intermédiaire le régime de crossover. Dans notre travail, nous avons étudié quatre géométries de pores (voir la figure 1.8) afin d'étudier les différents régimes de perméation des gaz à travers les membranes de graphène nanoporeux. Dans le tableau 1.2, nous comparons le rapport de taille entre les quatre géométries de pores et les quatre espèces de gaz. Pour les tailles de pores sub-nanométriques, telles que Pore-13a, Pore-16a et Pore-24a, le régime de perméation des gaz est plus susceptible d'être de l'ordre du tamisage moléculaire ou du crossover, car le rapport est proche de 1. Pour les

pores de taille nanométrique, Pore-2nm, il est plus probable que le régime soit proche de l'effusion dû au rapport > 1.

$Gas - Pore$	$\frac{Pore-13a}{cintique\ diamtre}$	$\frac{Pore-16a}{cintique\ diamtre}$	$\frac{Pore-24a}{cintique\ diamtre}$	$\frac{Pore-2nm}{cintique\ diamtre}$
CO_2	1,69	1,69-2,36	2,36	6,21
CH_4	1,47	1,47-2,05	2,05	5,39
O_2	1.62	1.62-2.25	2.25	5.92
N_2	1.53	1.53-2.14	2.14	5.63

Table 2: Résumé du rapport entre la taille des pores et le diamètre cinétique moléculaire.

Ce travail de doctorat vise à améliorer la connaissance du transport et de la séparation des gaz par le graphène nanoporeux. Plus précisément, trois questions scientifiques sont abordées dans ce travail :

- Pouvons-nous modéliser les différents régimes de perméation avec des simulations de dynamique moléculaire ?
- Pouvons-nous proposer un modèle mécanistique quantitatif pour le transport de gaz à travers des membranes de graphène nanoporeuses monocouches qui serait valable pour tous les régimes de perméation ?
- Pouvons-nous utiliser un tel modèle théorique pour prédire la sélectivité de la membrane avec différents mélanges de gaz ?

Pour répondre à ces questions, nous avons eu recours à de nombreuses simulations de dynamique moléculaire réalisées pour une variété de tailles de pores, de molécules de gaz et de conditions thermodynamiques. L'objectif principal de cette thèse est de proposer un cadre théorique qui aidera à la conception de membranes de graphène nanoporeuses pour des applications de séparation des gaz.

0.3.2 Plan du manuscript de thèse

Voici les grandes lignes de ce travail :

- Le chapitre 2 est consacré à la description des méthodes et des techniques de simulation utilisées dans cet ouvrage. Tout d'abord, des informations générales sur la thermodynamique, les simulations moléculaires et la mécanique statistique sont fournies. Ensuite, nous présentons des définitions, des méthodes et des algorithmes spécifiques utilisés dans cet ouvrage.

- Le chapitre 3 est consacré à la description d'un modèle théorique proposé dans cet ouvrage pour prédire la perméance des membranes 2D. Nous présentons les bases théoriques de ce modèle, puis nous introduisons les méthodes utilisées pour calculer les prédictions du modèle.

- Le chapitre 4 est consacré à l'étude d'une membrane simplifiée 2D. Nous utilisons ce système simplifié pour évaluer nos méthodes et vérifier comment le modèle théorique fonctionne avec des systèmes moléculaires simples.

- Le chapitre 5 est consacré aux systèmes graphène-gaz réalistes. Nous documentons les régimes de perméation obtenus pour une variété de géométries de pores, d'espèces de gaz et de conditions thermodynamiques. Nous montrons comment étendre le modèle théorique proposé pour les systèmes simplifiés au cas des systèmes graphène nanoporeux-gaz réalistes .

- Le chapitre 6 est consacré à l'étude de la séparation de mélanges gazeux binaires par le graphène nanoporeux. Après avoir donné une définition de la sélectivité de la membrane, nous étudions différents scénarios de séparation, en fonction de l'idéalité du mélange et des régimes de perméation du composé pur. Nous montrons comment notre cadre théorique est bien adapté à la description de la séparation par le graphène nanoporeux.

- Au chapitre 7, nous discutons des principales conclusions de ce travail. Après avoir fourni un résumé complet de nos résultats, nous discutons des perspectives et des extensions potentielles de cette thèse.

Conclusions et Perspectives

Dans ce chapitre, nous présentons des conclusions générales et des commentaires sur les travaux rapportés dans ce manuscrit. En outre, les perspectives et les extensions potentielles de ce travail sont discutées.

0.4 Conclusions Générales

Dans ce travail, nous avons utilisé des simulations moléculaires pour étudier la perméation et la séparation des gaz à travers des membranes de graphène nanoporeuses à couche unique. Nous avons montré que la perméation des gaz peut être typiquement découplée en deux étapes : le franchissement de la barrière et la désorption de la région de l'embouchure des pores. La combinaison des techniques EMD et NEMD nous a permis d'analyser séparément les contributions du franchissement de la barrière et de la désorption. En tenant compte de ces deux mécanismes, nous avons proposé l'expression suivante pour le coefficient de transport : $\Lambda = P_{des}\Lambda_{cross}$, où Λ_{cross} est un coefficient de transport lié aux événements de franchissement de barrière, et P_{des} est la probabilité qu'une molécule de gaz perméable se désorbe de l'embouchure des pores du côté aval de la membrane. Ce formalisme est motivé par les résultats de simulations effectuées sur des systèmes simplifiés, comme indiqué au chapitre 4.

Dans nos simulations moléculaires, nous avons observé que le régime de perméation évolue continuellement du régime de tamisage moléculaire (pour les petites tailles de pores) au régime d'effusion (pour les grandes tailles de pores). Les résultats de nos simulations montrent que la probabilité de désorption P_{des} approche la valeur de 1 dans le régime de tamisage moléculaire en raison des barrières énergétiques élevées qui empêchent les molécules de gaz de retraverser la membrane. Même si nous n'avons pas atteint la limite du régime d'effusion dans nos simulations, lorsque la taille des pores est plusieurs fois supérieure au diamètre des molécules de gaz, le rapport de Λ/Λ_{cross} tend vers l'unité à mesure que la taille des pores augmente. P_{des} peut théoriquement être considéré comme égal à 1 dans le régime d'effusion car le processus de désorption ne concerne qu'une minorité de molécules traversant la membrane près du bord du pore. Dans le régime dit

de "crossover", intermédiaire entre le tamisage moléculaire et l'effusion, l'influence de la cinétique de la désorption ne peut être négligée car la barrière d'énergie répulsive est moins prononcée et les molécules de gaz sont adsorbées dans le plan du pore. Dans ce régime, P_{des} est nettement inférieure à 1.

Pour la séparation des gaz, dans le cas d'un mélange gazeux idéal, le mélange n'a aucun effet sur le mécanisme de perméation. Les sélectivités de paires de gaz données peuvent donc être prédites à partir des perméabilités des composés purs. Dans nos simulations, les mélanges O_2/N_2 se comportent comme des mélanges gazeux idéaux. Pour les mélanges CO_2/CH_4, le mélange présente un comportement non idéal lorsque la température est proche du point critique du CO_2. Dans de telles conditions, nous ne pouvons pas prédire la sélectivité à partir des résultats obtenus pour les composés purs.

En ce qui concerne le coefficient de transport Λ, nous avons proposé un cadre théorique pour calculer la valeur de Λ_{cross}. Selon ce modèle, Λ_{cross} dépend du PMF entre une molécule de gaz diffusante et les atomes de la membrane. Quant à la probabilité de désorption, nous n'avons pas encore élaboré de modèle théorique. Pour proposer un cadre théorique pour P_{des}, nous pensons qu'il est nécessaire d'étudier la PMF 3D aux limites de la région de l'embouchure des pores.

Sur la base de la formule proposée pour Λ_{cross}, notre modèle devrait être prédictif pour les coefficients de transport et les facteurs de séparation dans le régime de tamisage moléculaire ($P_{des} = 1$) tant que la loi des gaz parfaits reste valable. Dans le régime intermédiaire de crossover, le cadre théorique du coefficient de transport reproduit bien les résultats des simulations, à condition que nous multipliions Λ_{cross} par la valeur de P_{des} obtenue à partir des simulations. Nous pouvons cependant prévoir les facteurs de séparation des mélanges de gaz dans le régime de crossover lorsque les deux espèces de gaz présentent des valeurs similaires de P_{des}.

Ces résultats valident le cadre théorique proposé, qui s'applique à tous les régimes de perméation.

0.5 Perspectives Générales

Dans ce qui suit, nous énumérons plusieurs extensions possibles de ce travail :

1. Dans ce travail, nous avons proposé une formule théorique pour le Λ_{cross}, qui tient compte du mécanisme de franchissement de la barrière. Nous avons montré que ce coefficient de transport n'est pas suffisant pour prédire la perméance de la membrane dans le régime de crossover. En effet, lorsque la taille des pores est comparable à celle de la molécule de gaz diffusante, la prédiction de la perméance nécessite un paramètre supplémentaire : la probabilité de désorption. Pour modéliser ce paramètre, nous allons étudier le PMF sur les limites de la région de l'embouchure

des pores définie aux chapitres 4 et 5. Nous pensons que P_{des} peut être déduit des théories traitant des problèmes de premiers temps de passage.

2. Une autre extension possible de ce travail réside dans l'étude du couplage entre les différentes forces motrices. Par exemple, nous étudierons comment la combinaison des gradients de pression et de température pourrait améliorer les performances des membranes de graphène nanoporeux. Selon le mélange étudié, le refroidissement ou le chauffage de la feuille de graphène peut permettre d'augmenter la séparation en favorisant ou en réduisant l'adsorption près du pore tout en introduisant une séparation thermo-diffusionnelle dans les réservoirs (effet Soret).

3. Si le graphène nanoporeux monocouche est considéré comme l'un des matériaux membranaires les plus prometteurs dans le processus de séparation de gaz, le graphène multicouches peut être synthétisé de manière plus économique que ce dernier. À l'heure actuelle, on ignore largement comment l'interaction entre les nanopores des différentes couches influencerait le processus de perméation et de séparation des gaz. Il est donc essentiel de comprendre les mécanismes physiques de la perméation des gaz à travers le graphène nanoporeux multicouches. Cela pourrait améliorer la viabilité technique et industrielle des membranes de graphène.

4. Dans ce travail, notre cadre théorique a été validé par des simulations moléculaires. Pour valider davantage notre théorie et l'appliquer aux procédés de séparation industrielle, il est nécessaire de comparer nos résultats à des résultats expérimentaux. Nous chercherons donc des collaborations possibles avec des équipes de recherche spécialisées dans les expériences nanofluidiques.

Enfin, il est important de souligner que le cadre théorique proposé dans ce travail ne se limite pas à la membrane de graphène. Nous pensons qu'il peut être utilisé pour traiter d'autres types de membranes 2D (polymère, MOF, silicène, etc.).

Chapter 1

Introduction

Contents

1.1 State of the Art in Gas Separation Process

Gas separation is a widely used technique in which the objective is the separation of one or more gases from a mixture[1]. It is becoming crucial for several industrial processes such as the treatment of fumes from coal-fired plants, in particular, aiming for the removal of CO_2 to reduce the greenhouse effect. The processes involved, such as distillation, account for 10-15% of the world energy consumption[2]. Growing interest is also given to other applications such as the separation and purification of commercially important gases such as CH_4 or even H_2 and He from natural gas. In this section, we presented three most common methods to perform gas separation:

- Separation by cryogenic distillation
- Separation by absorption/adsorption
- Separation with membranes

Among these methods, separation by cryogenic distillation is the most widely used method in the industry of air separation. However, it is based on phase transition, in other words, it is not environmentally friendly with more consumption of energy and emission of CO_2. In the oil and gas industry, the global separation market was valued at 7 billion dollars in 2017 and is expected to reach 14 billion by 2025, expanding at a CAGR[i] of 4.6% from 2017 to 2025. So it is important to find separation technologies which are both economical and practical. Unfortunately, alternatives to distillation, such as separating molecules according to their chemical properties or size, are under developed or expensive to scale up.

1.1.1 Separation by Cryogenic Distillation

Cryogenic distillation is based on the fact that in a mixture of gases they all have different boiling points and they could be separated by decreasing/increasing the temperature and pressure of the system in which they are stored, so that they can be divided into their single components[1]. The gas mixture is cooled down to a low temperature. Once in the liquid form, the components of the gas can be directed in a distillation column and through a series of compression, cooling and expansion steps, they can be distributed to different channels, depending on their boiling points[3]. In the past century, distillation became the dominant separation process at industrial scale following the development of the petroleum and chemical industries. Presently, distillation is carried out mainly continuously (Figure 1.1) in vertical hollow columns/towers, with associated piping, heat exchangers, pumps, storage vessels, support structures[4, 5, 6]. Considering the product and feed streams, the separation by distillation requires a decrease of the entropy so it can not happen spontaneously[7]. Consequently, addition of heat is used in practice to make this process thermodynamically possible. Hence, the overall efficiency of distillation is rather low due to irreversible losses related to the pressure drop, mass transfer (e.g. re-mixing in separations) and heat transfer[8, 9, 10].

Currently, distillation is the most widely used separation method at industrial scale with over 40 000 columns in operation worldwide. It is a widely used technique for streams that already have a high concentration of desired gas (typically over 90%) but it is not very appropriate for more dilute gas streams.

[i]Compound Annual Growth Rate

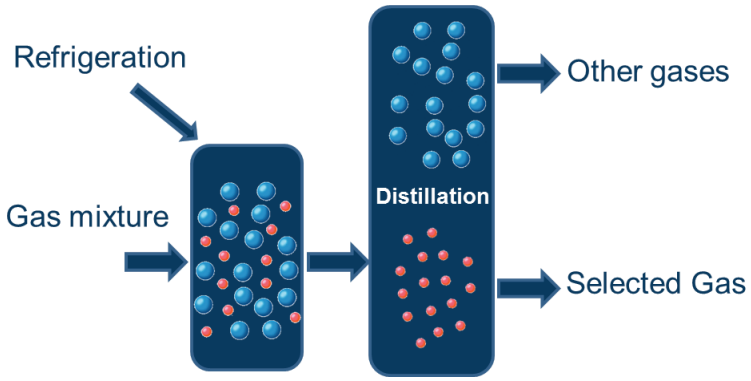

Figure 1.1: Schematics representation of cryogenic distillation method[1].

At this moment, the main transport option of natural gas is in the phase of liquid. So the main advantage of the cryogenic gas separation is that it enables direct production of liquid gas. A major disadvantage is connected with the high amount of energy required for the refrigeration especially for dilute gas streams. To improve the method of cryogenic distillation, several developments of distillation aiming to solve the problems related to the high investment and operating costs are improved in several aspects: use of other energy sources (e.g. solar energy)[11], combine distillation with reaction or other separations (membrane separation or distillation)[12], use a different operating mode based on separate phase movement to increase the separation efficiency, or integrate more functions into a single operating unit[6].

1.1.2 Separation by Absorption/Adsorption

The separation by absorption/adsorption is based on the affinity of the gas towards specific absorbent/adsorbent. For absorption process, a variety of liquid solvent is used as absorbents to remove specific gas from gas mixture streams. In this way, absorption process can usually be divided into chemical and physical categories[13]. Processes where the solvent chemically reacts with the dissolved gas are referred to as chemical absorption processes.

Physical absorption processes are processes where the solvent only interacts physically with the dissolved gas. Here a solvent is used as an absorbent with thermodynamic properties such that the relative absorption of specific gas is favored over the other components of the gas mixture. This kind of technology is often used in the post-combustion CO_2 capture process[14]. In many industrial applications, combinations of physical solvents and reactive solvents may be used in

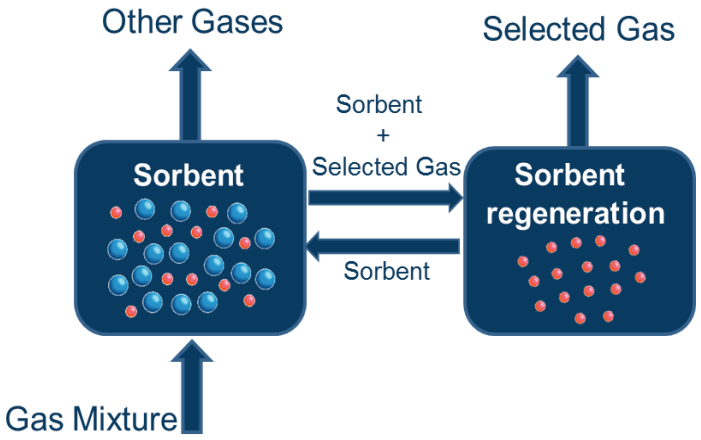

Figure 1.2: Schematics representation of pressure swing adsorption method[1].

tandem. However, in all cases, solvent recycling is energy and capital intensive.

Adsorption is the name of the spontaneous phenomenon of attraction that a molecule from a fluid phase experiences when it is close to the surface of a solid, named adsorbent[15, 16, 17, 18, 19]. Comparing with absorbent, adsorbent is porous solid, preferably having a large surface area per unit mass[20]. In adsorption process, the feed stream is put into contact with the adsorbent that is normally placed in fixed beds. The less adsorbed (light) component will break through the column faster than the other(s)[21, 22, 23, 24, 25]. In order to achieve separation, before the other (heavy) component(s) breaks through the column, the feed should be stopped and the adsorbent should be regenerated by desorbing the heavy compound. Since the adsorption equilibrium is given by specific operating conditions (composition, T and P), by changing one of these process parameters it is possible to regenerate the adsorbent[26]. In industrial gas separation process, three techniques are used:

- Pressure swing adsorption: Pressure swing adsorption (PSA) pressurizes and depressurizes gas around an adsorbent media to selectively adsorb certain components of a gas, allowing others to be selectively discarded.

- Vacuum swing adsorption: Vacuum swing adsorption (VSA) uses the same principle as PSA but swings between vacuum pressures and atmospheric pressure. The two techniques may be combined and are called ”vacuum pressure swing adsorption” (VPSA) in this case.

- Temperature swing adsorption: Temperature swing adsorption (TSA) uses a similar technique to other swing adsorption techniques but cycles temperature instead of pressure.

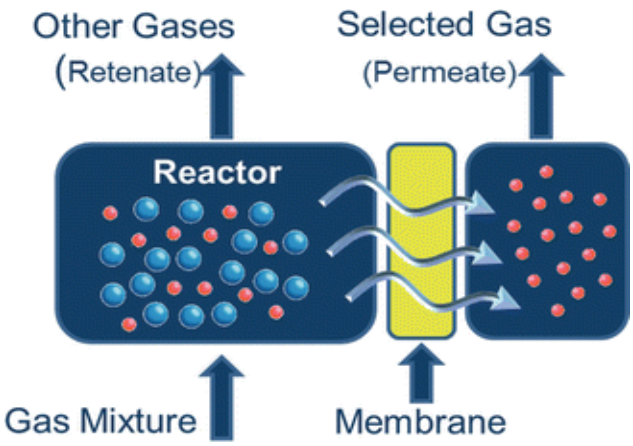

Figure 1.3: Schematics representation of membrane gas separation method[1].

When the regeneration of the adsorbent is performed by reducing the total pressure of the system, the process is termed pressure swing adsorption (PSA), the total pressure of the system swings between high pressure in feed and low pressure in regeneration[27, 28]. The PSA technology is used in the largest variety of applications, such as hydrogen purification[29, 30], CO_2 removal[31, 32, 33], air separation[34, 35] and natural gas production[36, 37, 38]. The main advantages of this technique is the high purity of the separated gas, the disadvantage consists in the high energy required for running the system, especially for the regeneration of the adsorbents.

1.1.3 Separation with Membranes

Separation of gases with membranes relies on the different affinities of one or more gases towards the membrane material, causing one gas to permeate faster (or slower) than others. Membrane science and technology are recognized today as powerful tools in solving some important global problems, developing new industrial processes needed for a sustainable industrial growth[39]. In the last few years, perm-selective membranes, which show different permeabilities for different chemical species, are gaining attentions in the gas separation process. Competing with consolidated operations such as pressure swing absorption and cryogenic distillation, the development of perm-selective membranes aims to decrease the production costs but also equipment size, energy utilization, and waste generation[40].

On the contrary to other conventional separation operations, gas separation with membrane does not require a phase change. The process is illustrated in Figure 1.3. The gas mixture is directed into a vessel and put in contact to the membrane material which is at the interface with another vessel. The mixture is allowed to diffuse into the second vessel under a pressure gradient

which promotes the mass transport through the membrane separating the retentate (slower gas) from the permeate (faster gas). The mechanism of gas separation with membrane is based on diffusion transport mechanism. Almost all the gas separation with membrane process have the same mechanism: adsorption of the gas into the membrane, permeation by diffusion through the membrane and desorption at low pressure side of the membrane[39].

The use of membrane in separation process is growing at a slow but steady rate[41]. During the past 20 years, sales of membrane gas separation equipment have grown to become a 150 million dollars per year business and more than 90% of this business involves the separation of non-condensable gases[41]. It is expected that membrane gas separation will play an increasingly important role in reducing the environmental impact and costs of industrial processes[42]. The use of membranes for gas separation offers several benefits, probably the most valuable is the high cost-efficiency (both for the mechanical simplicity of the system and for low energy regeneration). In fact, they do not require thermal regeneration, a phase change or active moving parts in their operation. Moreover, the absence of moving parts makes gas separation systems particularly suited for use in remote locations where reliability is critical; in addition, the small footprint makes them very attractive for remote applications such as offshore gas-processing platforms[43].

Probably the greatest limitation of membranes for gas separation derives from their trade-off relationship between permeability and selectivity for a required gas component. Permeability is the rate at which any compound permeates through a membrane, which is always expressed with the definition of permeance in units of $mol\ Pa^{-1}\ s^{-1}$[44]. Selectivity is the ability of a membrane to accomplish a given separation. It is usually described as the ratio of permeabilities for a given gas pair. The trade-off relationship means that high permeable membranes have low selectivity, requiring several run for a good separation, and highly selective membranes have low permeability, meaning long operational times. This trade-off was well addressed by Robeson in several articles[45, 46]. Gas separation with membrane has the potential to grow enormously if we can find more selective membrane materials. A variety of materials which the membrane could be composed of, including MOF[ii][47, 48], polymers[49, 50], zeolites[51, 52] and carbon-based materials[53, 54, 55] are available.

Figure 1.4 shows the results of Robeson plots for the separation of CO_2/CH_4 gas pair with different membrane materials. It is worth noting that the nanoporous graphene membrane has the potential to exceed the upper bound of other membrane materials. More details of nanoporous graphene material will be introduced in the next section.

[ii]Metal Organic Framework

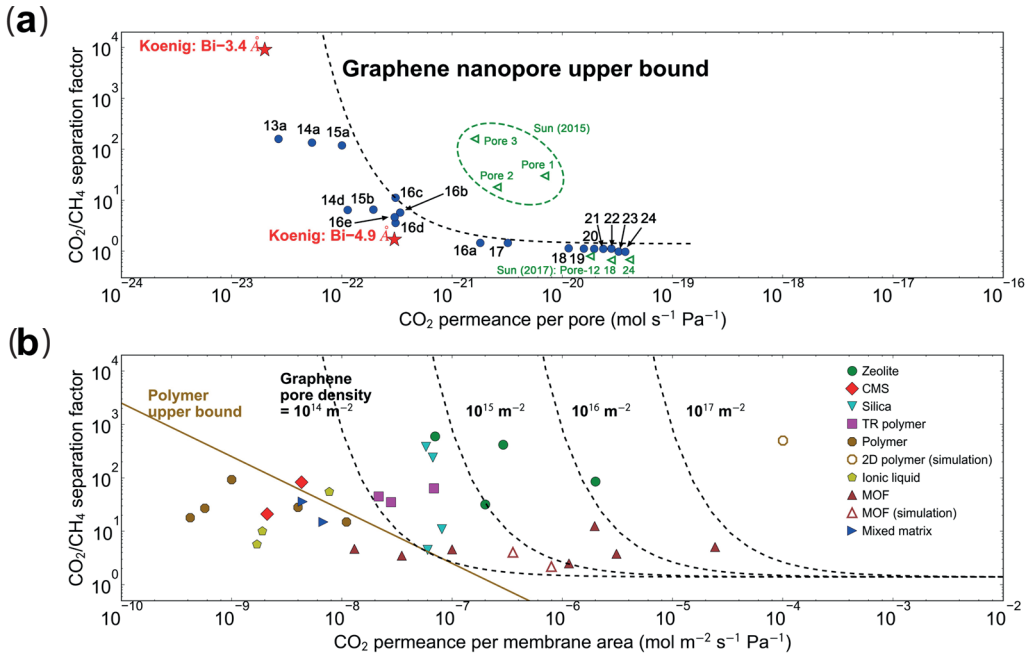

Figure 1.4: (a) Robeson plot (separation factor vs permeance per pore) characterizing the CO_2/CH_4 separation through various graphene sub-nanometer pores at 300 K. (b) Comparison between a porous graphene membrane and other membranes for CO_2/CH_4 separations[44].

1.2 Nanoporous Graphene Material

The isolation of graphene was first succeeded by Geim et al. in 2004 through mechanical exfoliation of graphite[57]. The Royal Swedish Academy of Sciences has decided to award the Nobel Prize in Physics in 2010 to Andre Geim and Konstantin Novoselov, "for groundbreaking experiments regarding the two-dimensional material graphene". Graphene is a densely packed 2D sheet of sp^2 hybridized carbon atom arranged in a honeycomb lattice, which composes two equivalent sub-lattices of carbon atoms bonded together with σ bond, and each carbon atom in the lattice has a π orbit that contributes to a delocalized network of electrons[58, 59, 60, 57]. With its atom-thin thickness, it is considered as the most significant carbon material over the last decades. It exhibits a strong ambipolar electric field effect with a density of charge carriers up to $10^{13} cm^2$[61]. The room temperature electron mobility of a graphene sheet can exceed 200,000 $cm^2 V^{-1} s^{-1}$, as in a suspended state or loading on a proper substrate[57, 62, 63]. At the same time, it has a large theoretical specific surface area ($2630 m^2 g^{-1}$), excellent mechanical strength and chemical stability[57, 64, 65].

As we have discussed in the previous section, membrane technique is gaining attention in separation process, where the most important parameter in this technique is the porous material used. With its characteristics, graphene has the potential to be one of the most favorable porous material. A pristine graphene sheet is perfectly impermeable, even to the smallest molecules, such as helium[66], so it is essential to generate nanopores to enables the applications as porous material. With the generation of nanopores, nanoporous graphene material have received tremendous attention in both academic and industrial applications[56], as shown in Figure 1.5.

1.2.1 Synthesis of Nanoporous Graphene

In the experimental studies, many methods besides mechanical exfoliation have been developed to isolate single layer graphene sheet. For instance, epitaxial growth on substrates[67] such as SiO_2, including atomic layer deposition or chemical vapor deposition[68], and thermal oxidation of graphite[69] is able to produce large scale pristine graphene with high quality.

In recent years, enormous experiments have been applied to generate nanopores in single layer graphene. The most widely used methods include both physical methods, such as focused electron beam ablation[70, 71], focused ion bean irradiation[72], ultraviolet induced oxidative etching[73], ion bombardment followed by oxidative etching[74], oxygen plasma etching[75], and chemical methods, such as surface-assisted aryl-aryl coupling of designed block[76] and MnO_2 etching[77]. Depending on the production techniques used, the pore size (the diameter of the pores) ranges from atomic precision to nanometer scale. As a result of the pores in the graphene plane, porous

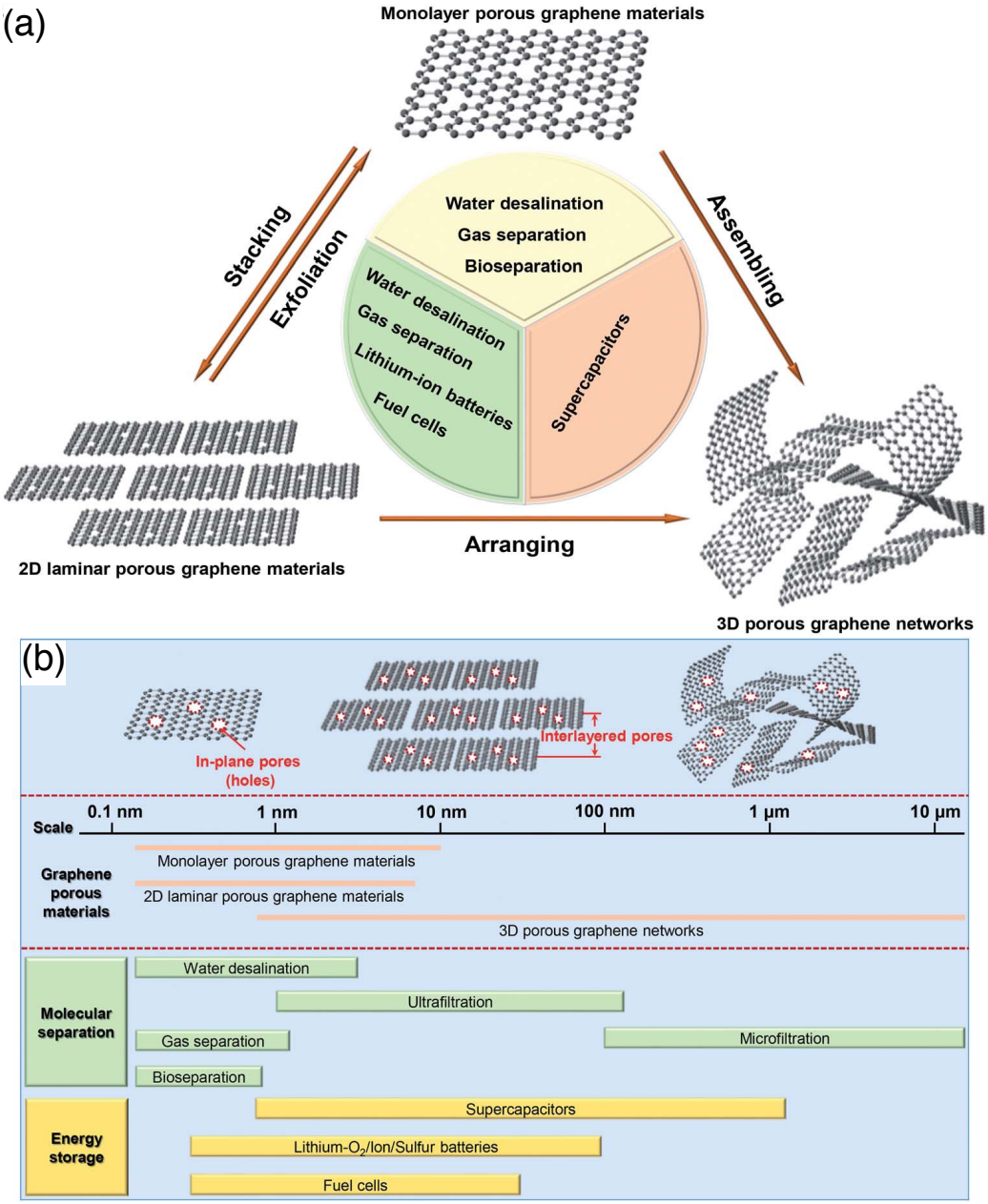

Figure 1.5: Type of nanoporous graphene-based materials and their broad applications. (a) Nanoporous graphene-based materials and their applications. (b) Classification of nanoporous graphene-based materials, definition of in-plane pores and interlayered pores in nanoporous graphene-based materials and broad applications based on pore sizes[56].

graphene exhibits properties distinct from those of pristine graphene, enabling many potential applications in numerous fields.

Methods	Pore size (nm)	Area (μm^2)	Density	Advantages	Limitations
Focused electron beam irradiation[70]	3.5	n/a	n/a	Tunable and well-defined pore size	Small area
Nitrogen assisted electron beam irradiation[71]	5.9	n/a	n/a	Controlled pore size	Small area
Ultraviolet induced oxidative etching[73]	0.4-10	19.63	n/a	Large area samples	Wide size distribution
Ion bombardment and chemical oxidative etching[74]	0.4	n/a	n/a	Large area, Controlled pore size	Moderate pore density
Focused ion beam irradiation[72]	5-100	12.57	10^3-10^6 per membrane	Tunable and well-defined pore size	Small area
Oxygen plasma etching[75]	1	12.57	$1/100nm^2$	Large area samples, tunable pore size	Moderate pore density
Surface assisted aryl-aryl coupling of the designed block[76]	0.4	n/a	n/a	Simple, cost effective	Difficult to transfer
MnO_2 etching[77]	2.4	n/a	n/a	Simple	Difficult to control pore sizes

Table 1.1: Summary of different state-of-the-art methods for nanopore generation in graphene.

In Table 1.1, we summarize the different methods to generate nanopores in graphene and in Figure 1.6, we show the images of nanopores generated by these methods. Depending on our requirements of scientific applications, we can employ appropriate methods. Nevertheless, among these methods, pore size and shape distribution is still not well characterized in synthesized samples. When it comes to the real industrial applications, the scalability to larger processes seems to be an issue.

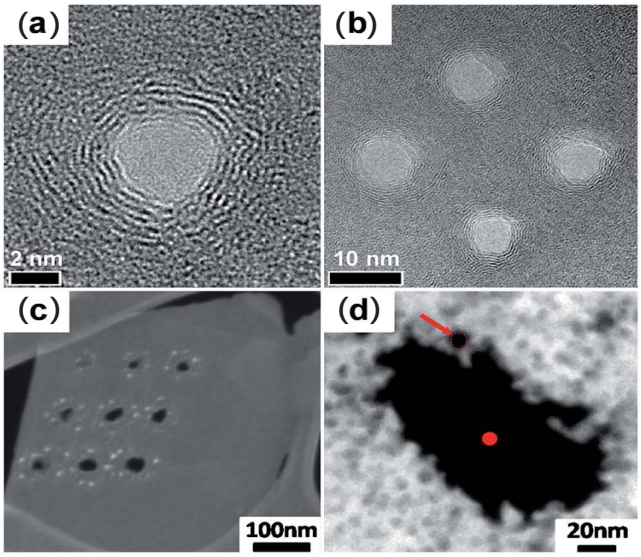

Figure 1.6: (a) Image of the nanopores generated by focused electron beam in graphene. (b) Multiple nanopores made in close proximity to each other by focused electron beam[70]. (c) Image of nine holes etched in a graphene flake. (d) Plasmon energy loss image with material thickness contrast, the dot at the hole center shows the nominal diameter of the electron beam used to etch the hole (about 5.9nm)[71]

1.2.2 Advantages of Nanoporous Graphene in Gas Separation Process

The nanoporous graphene can be considered as one of the most favorable membrane materials in gas separation process. As we have introduced in previous section, membrane process has several advantages including lower energy costs, smaller capital investment, and less mechanical complexity[39]. Moreover, nanoporous graphene is an existing excellent starting material for development of membrane with its specific advantages[78, 79]:

- The high mechanical strength of graphene can ensure the stability of porous frameworks, and thus prevents the deformation of the porous structures.
- The prominent chemical and thermal stabilities of graphene enable this porous material to withstand rigorous environments.
- The nanopores allow smaller molecules to pass through and block larger molecules to provide high selectivity.
- The one-atom thickness allows to consume less energy to maintain the flow and it is suitable

for the rapid diffusion of ions and molecules.

Sheng et al. first proposed the use of nanoporous graphene as an atomic-thin, highly efficient, and selective membrane for gas separation[80]. The other studies also predicted that nanoporous graphene can be applied for the purification of methane[81], and the separation of CO_2/N_2[82] or H_2/N_2[83]. Some researchers such as Hauser, Schrier, and Schwerdtfeger even suggested that nanoporous graphene can be used to separate He^3/He^4 isotopes[84, 85]. In experimental studies, Koenig et al. used nanoporous graphene as molecular sieve[73]. A pressurized blister and mechanical resonance were used to measure the transport of various gas (H_2, CO_2, Ar, N_2, CH_4 and SF_6) through the pores. As expected, the nanoporous graphene showed molecular selectively and the measured leak rates decreased with the increasing molecular sizes, which agreed well with models based on molecular diffusion through a small number of angstrom-sized pores[73].

1.3 Motivations and Outline of Thesis

1.3.1 Motivations

As we have introduced, nanoporous graphene is an attractive material to design membranes for gas separation process and large scale production of nanoporous graphene sheets with controlled pores are expected. As far as experimental studies are concerned, we have enlightened the difficulties in assessing the pores sizes and shapes and their influence on the measured transport and separation properties. Nevertheless, due to the advance in computational power and force fields accuracy, molecular simulations can be considered as a complement to experimental studies.

In order to achieve high selectivity for gas separation, the pore diameter should be commensurate with the kinetic diameter of gas molecules. To decide the proper pore size and guide the pore design, numerous authors have put a tremendous amount of work to compute transport coefficient and selectivity of gas by molecular dynamic (MD) simulations. Yuan et al[44] demonstrated a trade-off relationship between permeability and selectivity of a given gas pair, and that nanoporous graphene has the potential to surpass the Robeson upper bound when the areal pore density is large enough. Thus, on the one hand, a theoretical framework is needed to predict the transport coefficient and obtain a quantitive prediction of selectivity. On the other hand, there is no precise and universal understanding how the parameters such as pore size and geometry, gas density and temperature impact the transport and separation of gas.

On the basis of the ratio between pore size and molecular size, the gas permeation regime can be divided into three regimes. As shown in Figure 1.7, the gas permeation regime continuously evolves from molecular sieving[86] (pore size $<$ molecular size), for which the crossing of the

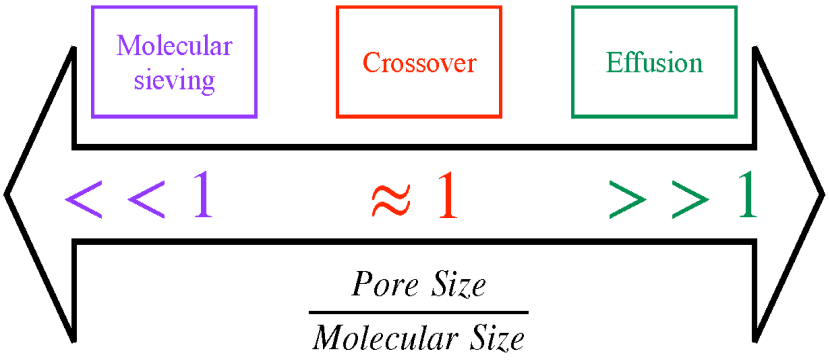

Figure 1.7: Molecular diffusion regime according to the ratio between pore size and molecular size

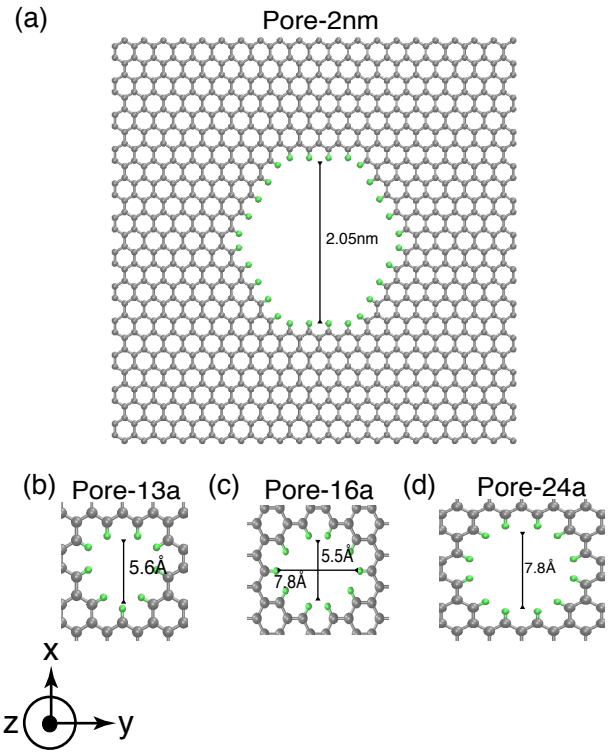

Figure 1.8: Zoom in view of Pore-2nm (a), Pore-13a (b), Pore-16a (c), Pore-24a (d) in the $xy-$ *plane*

free energy barriers controls the flow, to effusion[87] (pore size >> molecular size), for which free molecular flow are observed. Between these two regimes, the permeation mechanism is also

influenced by the kinetics of adsorption/desorption in the pore, as repulsive free energy barriers are less pronounced and the pore is not large enough to prevent permeating gas molecules to interact with the membrane atoms. We refer to this intermediate flow regime as the crossover regime. In our work, we investigated four pore geometries (see Figure 1.8) to address the different regimes of gas permeation through nanoporous graphene membranes. In Table 1.2, we compare the ratio of size between the four pore geometries and four gas species. For sub-nanometer pore sizes, such as Pore-13a, Pore-16a and Pore-24a, the gas permeation regime is more likely to be molecular sieving and crossover as the ratio is close to 1. For nanometer pore size, Pore-2nm, it is more likely to approach the effusion regime as the ratio > 1

$Gas - Pore$	$\frac{Pore-13a}{kinetic\ diameter}$	$\frac{Pore-16a}{kinetic\ diameter}$	$\frac{Pore-24a}{kinetic\ diameter}$	$\frac{Pore-2nm}{kinetic\ diameter}$
CO_2	1.69	1.69-2.36	2.36	6.21
CH_4	1.47	1.47-2.05	2.05	5.39
O_2	1.62	1.62-2.25	2.25	5.92
N_2	1.53	1.53-2.14	2.14	5.63

Table 1.2: Summary of ratio between pore size and molecular kinetic diameter.

This PhD work aims to improve the knowledge of gas transport and separation through nanoporous graphene. More precisely, there are three scientific questions addressed in this work:

- Can we model the different permeation regimes with molecular dynamics simulations?
- Can we propose a quantitative mechanistic model for gas transport through single-layer nanoporous graphene membranes, which would be valid for all permeation regimes?
- Can we use such a theoretical model to predict the selectivity of the membrane to different gas mixtures?

To answer to these questions, we used extensive molecular dynamics simulations performed for a variety of pore sizes, gas molecules and thermodynamic conditions. The main objective of this thesis is to come up with a theoretical framework that will help the design of optional nanoporous graphene membranes for gas separation applications.

1.3.2 Outlines of Thesis

The outline of this work is as follows:

- Chapter 2 is devoted to the description of the methods and simulation techniques used in this work. First, general information on thermodynamics, molecular simulations and statistical mechanics is provided. Then we present specific definitions, methods and algorithms used in this work.

- Chapter 3 is devoted to the description of a theoretical model proposed in this work to predict 2D membrane permeance. We present the theoretical basis of this model, then we introduce the methods used to compute model predictions.

- Chapter 4 is devoted to the study of a simplified graphene-like 2D membrane. We use this simplified system to benchmark our methods and check how the theoretical model performs with simple molecular systems.

- Chapter 5 is devoted to realistic graphene-gas systems. We document the permeation regimes obtained for a variety of pore geometries, gas species and thermodynamic conditions. We show how to extend the theoretical model proposed for simplified systems to the case of realistic nanoporous graphene-gas systems.

- Chapter 6 is devoted to the study of binary gas mixtures separation through nanoporous graphene. After providing a definition of the selectivity of the membrane, we investigate different separation scenarios, depending on the ideality of the mixture and permeation regimes of the pure compound. We show how our theoretical framework is well-suited to the description of separation by nanoporous graphene.

- In chapter 7, we discuss the key findings of this work. After providing a comprehensive summary of our results, we discuss the perspectives and potential extensions of this thesis.

Chapter 2

Molecular Simulations and Methodology

Contents

2.1 Introduction

This chapter is dedicated to a brief description of the basic thermodynamics definitions, general methodology and classical molecular simulations techniques used in this work. It is organized in six sections :

- The first section is devoted to generalities on thermodynamics properties, this section can help us to understand better how to describe a system from a macroscopic point of view.
- In the second section, theoretical notions of statistical physics are discussed. Knowledge of their principles and their assumptions allows us to understand the interest and application of molecular simulations. These notions are therefore considered as a prerequisite for the understanding of molecular simulations.
- The third section of this chapter is devoted to the description of the Monte Carlo and molecular dynamics simulations used in this work.
- The fourth section is dedicated to the description of the force fields used to model the fluid-solid and fluid-fluid molecular interactions in our simulations.
- The fifth section is dedicated to the description of two techniques used to compute chemical potential and energy barriers in molecular dynamics used in this work, namely the widom method and the Adaptive Biased Force (ABF) technique.
- The sixth section is a comparison between Non Equilibrium Molecular Dynamics or NEMD and Equilibrium Molecular Dynamics or EMD simulations. It is also devoted to the definition of the transport coefficient and the description of post-treatment algorithm used in NEMD and EMD methods.

2.2 Classical Thermodynamics

This section introduces the important acknowledgement of thermodynamics, which is highly related to other chapters. The application of thermodynamics to any real problem starts with the specification of a particular region of space or body of matter designated as the system. Everything outside the system is called the surroundings. The system and surroundings interact through transfer of material and energy across the system boundaries, but the system is the focus of attention.

Once a system has been selected, we must describe its state. There are two possible points of view, the macroscopic and the microscopic. The former is defined as classical thermodynamics, relating to quantities such as composition, density, temperature, and pressure. These macroscopic coordinates require no assumptions regarding the structure of matter. They are few in number, are suggested by our sense perceptions, and are measured with relative ease. A macroscopic description thus requires specification of a few fundamental measurable properties. The macroscopic point of view, as adopted in classical thermodynamics, reveals nothing of the microscopic (molecular) mechanisms of physical, chemical, or biological processes. For more details, we refer to the references[88, 89, 90]

2.2.1 Fundamental Equations of Thermodynamics with Closed Systems

To describe a state of a system, there are usually eight functions of state: thermodynamic temperature T, pressure P, volume V, internal energy E, entropy S, enthalpy H, Helmholtz free energy A and Gibbs free energy G. Among them, T and P are intensive properties of systems and the others are extensive properties. In these functions, T, P, V, E and S are fundamental functions, which have clear physical meanings. Meanwhile, H, A and G are derived functions. Their relationships with other functions are:

$$H = E + PV \tag{2.1}$$

$$A = E - TS \tag{2.2}$$

$$G = H - TS = A + PV \tag{2.3}$$

According to the first and second laws of thermodynamics, for a homogeneous closed system, where the compositions do not change and there only exists volume work, it exists four funda-

mental equations of thermodynamics as followed:

$$dE = TdS - PdV \tag{2.4}$$

$$dH = TdS + VdP \tag{2.5}$$

$$dA = -SdT - PdV \tag{2.6}$$

$$dG = -SdT + VdP \tag{2.7}$$

As mentioned above, these thermodynamic properties are all functions of state, so the four fundamental equations are always correct for reversible and irreversible processes.

2.2.2 Fundamental Equations of Thermodynamics with Open Systems

For a homogeneous open system, the compositions of system change. In this situations , the fundamental equations of thermodynamics:

$$dE = TdS - PdV + \sum_{i=1}^{K} \mu_i dn_i \tag{2.8}$$

$$dH = TdS + VdP + \sum_{i=1}^{K} \mu_i dn_i \tag{2.9}$$

$$dA = -SdT - PdV + \sum_{i=1}^{K} \mu_i dn_i \tag{2.10}$$

$$dG = -SdT + VdP + \sum_{i=1}^{K} \mu_i dn_i \tag{2.11}$$

where μ_i is the chemical potential of component i. Chemical potential μ_i is an important thermodynamic property. According to equation 2.8 to equation 2.11, we can obtain:

$$\mu_i = (\frac{\partial E}{\partial n_i})_{S,V,n_j \neq n_i} \tag{2.12}$$

$$\mu_i = (\frac{\partial H}{\partial n_i})_{S,P,n_j \neq n_i} \tag{2.13}$$

$$\mu_i = (\frac{\partial A}{\partial n_i})_{T,V,n_j \neq n_i} \tag{2.14}$$

$$\mu_i = (\frac{\partial G}{\partial n_i})_{T,P,n_j \neq n_i} \tag{2.15}$$

where $n_j \neq n_i$ represents that other compositions n_j do not change while n_i is changing.

Equation 2.14 is practical in statistical physics to compute chemical potential. Meanwhile equation 2.15 is often considered as the basis to compute chemical potential in classical thermodynamics.

In the computation of thermodynamics, partial molar quantity $\overline{B_i}$ is frequently used. It represents the contribution of 1mol component i to the thermodynamic property B in an infinite system. It can be defined as:

$$\overline{B_i} = (\frac{\partial B}{\partial n_i})_{T,P,n_j \neq n_i} \tag{2.16}$$

With this definition, μ_i can be considered as the partial molar quantity of G.

The fundamental equations of thermodynamics for closed and open system express the general relationships between different thermodynamic functions of state. These equations are not limited by the specific characteristics of systems. They are widely used for computations of thermodynamic properties.

2.3 Statistical Mechanics

A microscopic description depends on the existence and behavior of molecules, is not directly related to our sense perceptions, and treats quantities that cannot routinely be directly measured. Nevertheless, it offers insight into material behavior and contributes to evaluation of thermodynamic properties. Bridging the length and time scales between the microscopic behavior of molecules and the macroscopic world is the subject of statistical mechanics or statistical thermodynamics, which applies the laws of quantum mechanics and classical mechanics to large ensembles of atoms, molecules, or other elementary objects to predict and interpret macroscopic behavior.

For a macroscopic system which consists of a large amount of microscopic particles about Avogadro Number, i.e. $\approx 10^{24}$, the system has certain macroscopic state, also called macrostate and the thermodynamic properties have certain values when the system reaches equilibrium. At the molecular level, however, a large number of states still exist because the microscopic state is always changing with time. At this scale, each atom is defined by 6 variables: 3 for its position ($\overrightarrow{r}$) and 3 for its momentum ($\overrightarrow{q}$), giving a total number of $6N_A$ variables for a system of N

particles. The space of all possible states is called the phase space. A given realization of the system $(\overrightarrow{r}, \overrightarrow{q})$ is called microstate and the total number of possible microstates is noted as Ω.

Herein, at the microscopic scale, a mole of system contains at least $6N_A$ degrees of freedom, where N_A is Avogadro's number with an order of 10^{23}. To describe such a system, by means of classical mechanics, we need to solve $6N_A$ differential equations of first order. It is obviously unpractical. Ludwig Boltzmann formulated in 1871[91] the fundamental ergodic hypothesis of statistical physics. It was initially formulated for the needs of the kinetic theory of gases. This hypothesis asserts that at equilibrium, the mean value of a quantity calculated over time (which is close to experimental measurements) is equivalent to its ensemble mean given by statistical physics. The ergodic hypothesis is therefore fundamental for a good reconciliation between theory and experience. In our case, this hypothesis is applicable to the two classical molecular simulation methods, the Monte Carlo "MC" which allows to emit statistical averages and the Molecular Dynamics "MD" which allows us to average the properties over time. We will introduce more details about molecular simulations in the next section.

In statistical mechanics, all the possible configurations of the system form a statistical ensemble. It should be noted that the Ω microstates correspond to a unique macrostate. Depending on the thermodynamic variables measured and the exchanged quantities of the system with the outside, several statistical ensembles are defined:

- Canonical ensemble: a closed system with constant temperature, where there is energy exchange but no mass exchange. In this system, the number of particles N, the volume V and the temperature T are fixed.

- Grand canonical ensemble: an open system with constant temperature, where there are both mass and energy exchange. In this system, the chemical potential μ, the volume V and the temperature T are fixed.

- Micro canonical ensemble: an isolated system with no mass and energy exchange. In this system, the number of particles N, the volume V and the energy E are fixed.

- Isothermal-isobaric ensemble: a closed system with constant temperature and pressure, where there is energy exchange but no mass exchange.In this system, the number of particles N, the pressure P and the temperature T are fixed.

Depending on the point of view of engineering applications, canonical ensemble, grand canonical ensemble and isothermal-isobaric ensemble are more widely used. For more details, we refer to reference[92, 93, 94, 95, 96, 97].

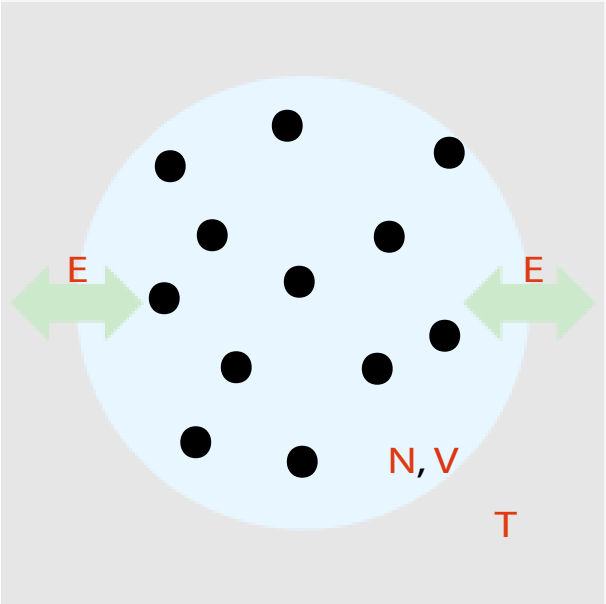

Figure 2.1: Canonical situation : the system, materialized by the blue sphere and black points, is in equilibrium with the bath in grey. The number of particles N and volume V are fixed, whilst temperature T is being imposed by exchanging energy E with a heat bath.

2.3.1 Canonical Ensemble: NVT

Canonical ensemble, referred thereafter as NVT ensemble, corresponds to the system which is coupled to a thermostat and held at a fixed temperature T, as seen on Figure 2.1. For this system, the total energy E, corresponding to the sum of kinetic energy K and potential energy U, is a variable that fluctuates around its average. At the microscopic scale, E can be expressed as:

$$E = \sum_{i=1}^{\Omega} p(i) E_i \tag{2.17}$$

where E_i corresponds to the energy of the microstate i an p(i) is the probability of observing microstate i. The sum of all the probabilities equals to 1. Using the Lagrange multipliers and Stirling's approximation formula, we can obtain the expression of p(i) in the NVT ensemble:

$$p(i) = \frac{\exp(-\beta E_i)}{Z_{NVT}} \tag{2.18}$$

where $\beta = 1/k_bT$, k_b being the Boltzmann constant[i], Z_{NVT} is the canonical partition function. It is defined as the sum of the Boltzmann factor $\exp(-\beta E_i)$ over all possible microstates Ω :

$$Z_{NVT} = \sum_{i=1}^{\Omega} \exp(-\beta E_i) \tag{2.19}$$

The sum over all possible microstates Ω can be replaced by an integral of over all configurations in phase space:

$$Z_{NVT} = \frac{1}{N!} \int_{\overrightarrow{r}^N} \int_{\overrightarrow{q}^N} \frac{d\overrightarrow{r}^N d\overrightarrow{q}^N}{h^{3N}} \exp(-\beta E(\overrightarrow{r}^N, \overrightarrow{q}^N)) \tag{2.20}$$

where h is the Planck constant, h^3 can be seen as a normalization factor which represents the volume of an individual quantum microstate $d\overrightarrow{r} \cdot d\overrightarrow{q}$ in the phase space. In the case of indistinguishable particles, $1/N!$ is introduced to account for $N!$ permutations of these particles which lead to the same microstate i. The integration over momentum can be performed analytically, thus equation 2.20 can be reduced to:

$$Z_{NVT} = \frac{\Lambda^{-3N}}{N!} \int_{\overrightarrow{r}^N} \exp(-\beta U(\overrightarrow{r}^N)) \tag{2.21}$$

where Λ is the de Broglie thermal wavelength. The partition function is the bridge between microscopic and macroscopic scale. In canonical ensemble, the most important relationship is expressed with Helmoltz free energy A:

$$A = -k_bT \ln Z_{NVT} \tag{2.22}$$

With the fundamental equations of thermodynamics, we can obtain other thermodynamic properties:

$$E = k_bT^2 (\frac{\partial \ln Z_{NVT}}{\partial T})_{V,N} \tag{2.23}$$

$$S = k_b \ln Z_{NVT} + k_bT (\frac{\partial \ln Z_{NVT}}{\partial T})_{V,N} \tag{2.24}$$

$$\mu = -k_bT (\frac{\partial \ln Z_{NVT}}{\partial N})_{V,T} \tag{2.25}$$

$$P = k_bT (\frac{\partial \ln Z_{NVT}}{\partial V})_{T,N} \tag{2.26}$$

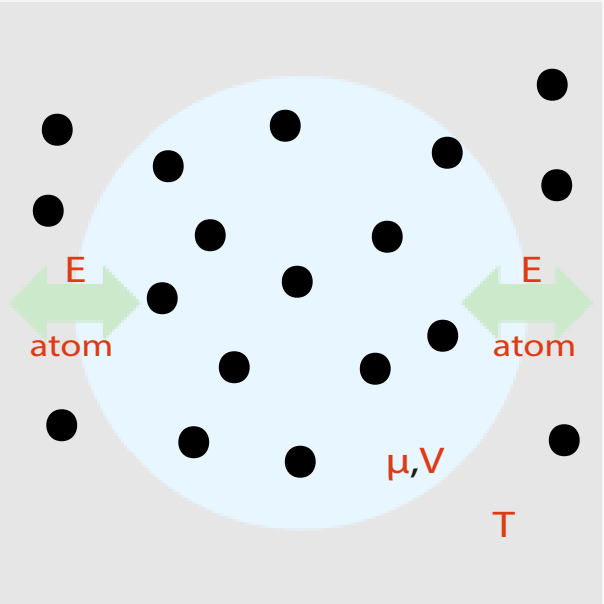

Figure 2.2: Grand canonical situation : the system, materialized by the blue sphere and black points, is in equilibrium with the bath in grey. The chemical potential μ and volume V are fixed, whilst temperature T is being imposed by exchanging energy E with a heat bath.

2.3.2 Grand Canonical Ensemble: μVT

Each system of this ensemble is in equilibrium with an external heat bath and reservoir of particles, at constant temperature and volume, referred thereafter as μVT ensemble. This formalism should be therefore applied when the number of particles as well as the energy of the system can fluctuate. μ represents the chemical potential which is constant. Comparing with NVT ensemble, the partition function associated with this ensemble is given by the following expression:

$$\Xi_{\mu VT} = \sum_i \sum_{N_i} \exp(-\beta(E_i - \mu N_i)) = \sum_{N_i} Z_{NVT} \exp(\beta \mu N_i) \tag{2.27}$$

where E_i and N_i represent a microstate with energy E_i and N_i particles. In the grand canonical ensemble, the most important relationship is expressed with PV:

$$PV = k_b T \ln \Xi_{\mu VT} \tag{2.28}$$

[i] $k_b = 1.38066 \times 10^{-23} Joule/Kelvin$

With the fundamental equations of thermodynamics, we can obtain other thermodynamic properties:

$$E = k_b T^2 (\frac{\partial \ln \Xi_{\mu VT}}{\partial T})_{V,\mu} \tag{2.29}$$

$$S = k_b \ln \Xi_{\mu VT} + k_b T (\frac{\partial \ln \Xi_{\mu VT}}{\partial T})_{V,\mu} \tag{2.30}$$

$$N = k_b T (\frac{\partial \ln \Xi_{\mu VT}}{\partial \mu})_{V,T} \tag{2.31}$$

$$P = k_b T (\frac{\partial \ln \mu_{\mu VT}}{\partial V})_{\mu,T} \tag{2.32}$$

2.3.3 Micro Canonical Ensemble: NVE

This ensemble describes a completely isolated system with constant energy, where there is no particles or energy exchange with the surroundings. It is the fundamental system for MD simulations. In this system, all the microstates have the same probabilities of observing and p(i) can be simply expressed as :

$$p(i) = \frac{1}{\Omega} \tag{2.33}$$

We can still use the expression of entropy S in NVT ensemble. In this way, S in NVE ensemble is expressed:

$$S = k_b \ln \Omega \tag{2.34}$$

This is the famous Boltzmann's entropy formula, which is often used to describe the definition of entropy. Other thermodynamic properties can be deduced with the equation:

$$dS = \frac{1}{T} dE + \frac{P}{T} dV - \sum_j \frac{\mu_j}{T} dN_j \tag{2.35}$$

2.3.4 Isothermal-isobaric Ensemble: NPT

If the system is maintained at constant temperature T and pressure P due to energy and volume exchange through a thermostat and barostat, it stands in the isothermal-isobaric (NPT) ensemble. NPT ensemble is important because it is related to experiment conditions, during which one controls both pressure and temperature in a closed vessel.

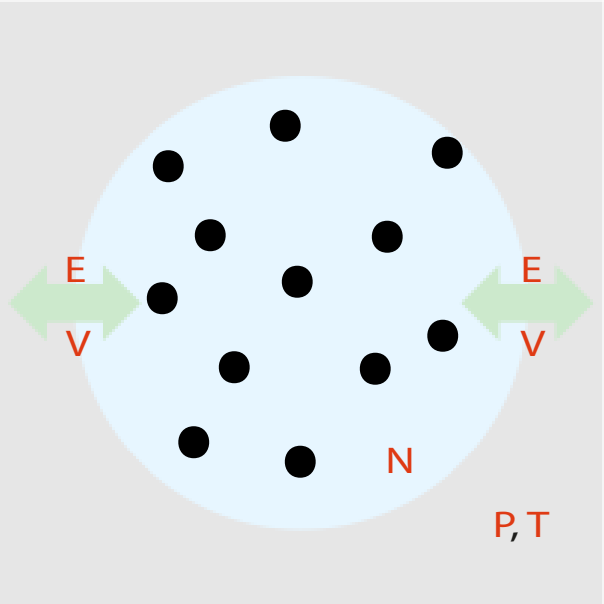

Figure 2.3: Isothermal-isobaric situation : the system, materialized by the blue sphere and black points, is in equilibrium with the bath in grey. The number of particle N is fixed, whilst temperature T and pressure P being imposed by exchanging energy E and volume V changing with a thermostat and barostat.

In this ensemble, the partition function is given by the expression as followed:

$$\Delta_{NPT} = \sum_i \sum_{V_i} \exp(-\beta(E_i + PV_i)) = \sum_{V_i} Z_{NVT} \exp(-\beta P V_i) \tag{2.36}$$

where E_i and V_i represent a microstate with energy E_i and pressure volume V_i. In isothermal-isobaric ensemble, the most important relationship is expressed with Gibbs free energy G:

$$G = k_b T \ln \Delta_{NPT} \tag{2.37}$$

As mentioned above, we can obtain other thermodynamic properties with fundamental equations and the properties are expressed as:

$$S = k_b \ln \Delta_{NPT} + k_b T (\frac{\partial \ln \Delta_{NPT}}{\partial T})_P \tag{2.38}$$

$$V = -k_b T (\frac{\partial \ln \Delta_{NPT}}{\partial P})_T \tag{2.39}$$

$$H = k_b T^2 (\frac{\partial \ln \Delta_{\mu VT}}{\partial T})_P \tag{2.40}$$

Ensemble	Partition functions	Associated equations
Microcanonical/NVE	$\sum_{i=1}^{\Omega} p(i) = 1$	$dE = TdS - PdV + \mu dn$
Canonical/NVT	$Z_{NVT} = \sum_{i=1}^{\Omega} \exp(-\beta E_i)$	$dA = -SdT - PdV + \mu dn$
Isothermal-isobaric/NPT	$\Delta_{NPT} = \sum_V Z_{NVT} \exp(-\beta PV)$	$dG = -SdT + VdP + \mu dn$
Grand Canonical/μVT	$\Xi_{\mu VT} = \sum_N Z_{NVT} \exp(\beta \mu N)$	$d(PV) = SdT + PdV + \mu dn$

Table 2.1: Characteristics of main statistical ensembles.

Table 2.1 summarizes the partition functions and the fundamental equations associated with each statistical ensembles.

2.4 Molecular Simulations

In this section, we provide details about two types of molecular simulation techniques: Monte Carlo (MC) and Molecular Dynamics (MD) simulations. These techniques are strongly connected with the development of the performances of computers. So, since the early 90's, an increasing of publications about molecular simulations has been observed[98]. Although the simulated systems are clearly at the nano scale (few nanometers (nm)), the simulation techniques described in the following obey to the law of classical mechanics. Quantum effects are indeed negligible at sufficiently high temperature and for large enough particles as studied in this work. In our work, we used molecular dynamics to study the gas transport behavior in simplified systems (chapter 4) and realistic graphene system (chapter 5). We also studied gas separation with nanoporous graphene membrane by molecular dynamics (chapter 6). All the simulations were accomplished with LAMMPS[99].

2.4.1 Monte Carlo Simulations

Historically, the Monte Carlo method is the first classical molecular simulation technique. In 1953, it was proposed by Nicholas Metropolis[100]. This method is purely statistical. It is based on Markov chain processes: instead of solving the equations of motions in an iterative fashion as in molecular dynamics, the method transforms the system from one configuration to another configuration according to a given transition probability, which is chosen to obtain the probability density of the desired statistical ensemble. The Monte Carlo technique is widely used to study the equilibrium properties of molecular systems such as phase equilibria[101, 102]. In our work,

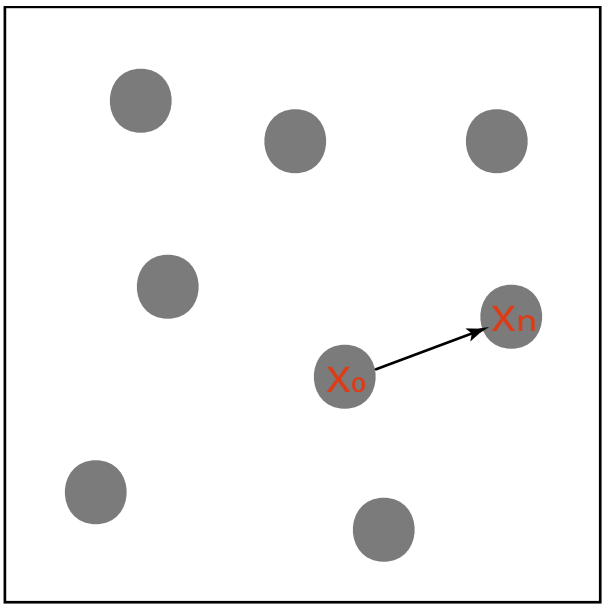

Figure 2.4: Illustration of Monte Carlo move : the new configuration is generated by a random displacement of one particle within the simulation box.

we mainly used the GCMC [ii] module implemented in LAMMPS[99].

Markov Chain

The probability that a system in configuration a is transformed into configuration b characterized a Markov chain. If this transition probability is noted π_{ab}, the condition for the Markov chain to converge to the probability density ρ is given by the following stationary condition, given in matrix notation :

$$\pi\rho = \rho \tag{2.41}$$

where the dimension of the square matrix π and of the vector ρ is the number of all possible configurations (a huge number but a finite one as a consequence of quantum mechanics principles).

In molecular simulation, we know the probability density of each configuration (details in section 2.3), and we must determine the elements of the transition matrix so that the equation 2.41 is respected. For this purpose, it is sufficient to use the following equation, called microscopic reversibility condition, for each configuration pair a and b :

$$\rho_a \pi_{ab} = \rho_b \pi_{ba} \tag{2.42}$$

[ii] Grand Canonical Monte Carlo

In this equation, the left side is the flow of configurations a transformed into configurations b, while the right side is the reverse flow from b to a. In practice, it is therefore sufficient to define π_{ab} and π_{ba} so that the two flows are equal.

Metropolis Algorithm

The Metropolis algorithm is a means of generating a Markov chain where each iteration comprises two steps[102] : in the first step, a new configuration is generated by a random change (for example a random rotation or translation) ; in a second step, the new configuration is accepted or rejected according to a criterion intended to generate the desired distribution. The probability that the new configuration is accepted is given by :

$$P_{acc}(old \rightarrow new) = min(1, \frac{\rho_{new}}{\rho_{old}}) \tag{2.43}$$

where ρ stands for the probability density of the configuration in the statistical ensemble under consideration, and the acceptance probability P_{acc} is related to the transition probability of the Markov chain through:

$$\pi_{ab} = \frac{1}{\Omega} P_{acc}(a \rightarrow b) \tag{2.44}$$

where Ω stands for the number of accessible configurations.

It may be easily verified that the application of the Metropolis criterion (equation 2.43) to the reverse flow (from the "new" to the "old" configuration) respects the microscopic reversibility condition stated by equation 2.42, also referred as "detailed balance" condition.

Note that the Metropolis algorithm does not need to know the number of accessible configurations Ω to calculate the probability of acceptance. Similarly, the Broglie wavelength Λ resulting from the integration of the kinetic part of the energy generally cancels itself out because only the ratio of the probability densities appears in the equation 2.45. Consequently, the expression of the probability density is often quite simple. For example, in the case of the NVT set, it is expressed as follows

$$P_{acc}(old \rightarrow new) = min(1, \exp(-\beta(E_{new} - E_{old})) \tag{2.45}$$

This criterion is exploited in the following way:

- If $E_{new} < E_{old}$, i.e. $\exp(-\beta(E_{new} - E_{old}) > 1$, the new configuration is accepted, i.e. it is added to the ensemble;

- If $E_{new} > E_{old}$, a random number q is selected between 0 and 1, and the new configuration is accepted if $\exp(-\beta(E_{new} - E_{old}) > q$. Otherwise, the old configuration is added to the ensemble.

Monte Carlo methods make extensive use of random number generators to generate the new configurations and apply the acceptance criterion.

Once a sufficient number of configurations has been generated by the above procedure, they form a representative subset of the statistical ensemble, i.e. every accepted configuration appears proportionally to its Boltzmann factor. Then, standard averaging formula can be used to derive macroscopic properties such as volume, potential energy, pressure, etc.

GCMC

The GCMC is a very versatile and powerful Monte Carlo technique that explicitly accounts for density fluctuations at fixed volume and temperature[103, 104]. It is widely used in adsorption studies in microporous material[105, 106]. It combines random insertions-deletions of particles with the classic Monte Carlo random displacements. Insertions / deletions consist in exchanging particles with a fictitious reservoir of fluid at the same chemical potential than the simulation box. Therefore, this movement allows a fluctuation of the number of particles in the system, and is characteristic of the MC simulation in the Grand Canonical ensemble, referred to hereafter as GCMC simulations.

2.4.2 Molecular Dynamics

Contrary to MC simulations which reproduce a statistical evolution of the system, classical Molecular Dynamics (MD) are somehow more intuitive, as they reproduce a time evolution of the system, by integrating the Newton equations of motion over time. Thus, MD give access to the trajectories and velocities of each individual particles. It is then possible to not only determine static properties at equilibrium, but also to study transport properties of system at equilibrium and out of equilibrium. It is worth noticing that, due to the ergodicity principle, MC and MD simulations should give the same results for any given observable X.

This technique is very close to a numerical experiment, as it consists in simulating the evolution of a system of particles over time to deduce the macroscopic properties by making space-time averages representative of the system if the phase space is well explored. The molecular dynamics simulation algorithm solves Newton's second law of motion for each atom aiming to determine the trajectories of the system in phase space by producing a temporal evolution of the position

$\overrightarrow{r}$ and the momentum $\overrightarrow{q}$ for each particle.

$$\begin{aligned} \overrightarrow{q_i} &= m_i \frac{d\overrightarrow{r_i}}{dt} \\ \frac{d\overrightarrow{q_i}}{dt} &= -\overrightarrow{\nabla} U_i = \overrightarrow{F_i} \end{aligned} \tag{2.46}$$

where $\overrightarrow{q_i}$ and $\overrightarrow{r_i}$ are the momentum and position of particle i, respectively, m_i is the mass of i and $\overrightarrow{F_i}$ represents the sum of forces acting on particle i.

Steps in Performing an MD Simulation

- Choose the interaction model, called force field, which is introduced in section 2.5
- Define the boundary conditions and set the initial conditions (positions, velocities, etc). The velocities are calculated initially from the Maxwell Boltzmann distribution[107] which makes it possible to tend more quickly towards equilibrium.
- Choose the ensemble, as introduced in section 2.3, such as NVE, NVT, NPT, etc.
- Set the target temperature, density/pressure, etc.
- Choose the integrator, thermostat, barostat, etc.
- Perform the simulation until the equilibration or steady state is reached (property dependent).
- Perform production simulation to collect time averages.
- Analyse the results by post-treatment algorithm. In our work, we used post-treatment algorithms to compute transport coefficients and separation factors.

Verlet Integration

Verlet integration is a numerical method used to integrate Newton equations of motion. It is frequently used to calculate trajectories of particles in molecular dynamics simulations and computer graphics. The algorithm was first used in 1791 by Delambre and has been rediscovered many times since then, most recently by Loup Verlet in the 1960s[108] for use in molecular dynamics. The Verlet integrator provides good numerical stability, as well as other properties that are important in physical systems such as time reversibility and preservation of the symplectic form on phase space, at no significant additional computational cost over the simple Euler method[109, 110, 111].

The Velocity-Verlet algorithm is based on Taylor expansions of positions of particles. The velocities are deduced from the calculated velocities at each half time step.

For a particle i, where the position $r_i(t)$, the velocity $v_i(t)$ and the acceleration $a_i(t)$ are known at time t, the position of particle i at $t + \Delta t$ is given by:

$$\overrightarrow{r_i}(t + \Delta t) = \overrightarrow{r_i}(t) + \Delta t \overrightarrow{v_i}(t) + 0.5\Delta t^2 \overrightarrow{a_i}(t) + \overrightarrow{O}(\Delta t^3) \tag{2.47}$$

Then we can compute the velocity at $t + \Delta t/2$:

$$\overrightarrow{v_i}(t + \Delta t/2) = \overrightarrow{v_i}(t) + 0.5\Delta t \overrightarrow{a_i}(t) \tag{2.48}$$

and the acceleration at $t + \Delta t$ is calculated by:

$$\overrightarrow{a_i}(t + \Delta t) = \frac{-1}{m_i} \overrightarrow{\nabla} U_i(t + \Delta t) \tag{2.49}$$

The velocity at $t + \Delta t$ is deduced and expressed by:

$$\overrightarrow{v_i}(t + \Delta t) = \overrightarrow{v_i}(t + \Delta t/2) + 0.5\Delta t \overrightarrow{a_i}(t + \Delta t) + \overrightarrow{O}(\Delta t^3) \tag{2.50}$$

We can deduce the kinetic energy at the instant $t+\Delta t$, while the potential energy, at the same instant, is calculated in the loop of forces. The truncation error of the velocity and positions is on the order of $O(\Delta t^3)$.

Nosé-Hoover Thermostat

The Nosé-Hoover thermostat[112] is a method for controlling the temperature in a molecular dynamics simulation. The Nosé-Hoover thermostat "strives" to reproduce the canonical phase-space distribution. It was originally developed by Nosé and was improved further by Hoover. Although the heat bath of Nosé-Hoover thermostat consists of only one imaginary particle, simulation systems achieve realistic constant-temperature condition (canonical ensemble). Therefore, the Nosé-Hoover thermostat has been commonly used as one of the most accurate and efficient methods for constant-temperature molecular dynamics simulations.

The central idea is to simulate in such a way that we obtain a canonical ensemble, where we fix the particle number N, the volume V and the temperature T. This means that these three quantities are fixed and do not fluctuate. The temperature of the system is connected to the average kinetic energy via the equation:

$$K = \frac{3}{2} k_b T \tag{2.51}$$

Although the temperature and the average kinetic energy are fixed, the instantaneous kinetic energy fluctuates (and with it the velocities of the particles).

Nosé-Hoover thermostat controls the temperature by modifying the equations of motion to include a non-Newtonian term in order to maintain the total kinetic energy constant. The modified equation of motion is given by:

$$\frac{dv_i(t)}{dt} = \frac{F_i(t)}{m} - \varsigma v_i(t) \tag{2.52}$$

where ς is the thermodynamic friction coefficient, given by:

$$\frac{d\varsigma(t)}{dt} = \frac{1}{Q}\left[\sum m v_i(t)^2 - (X+1)k_bT\right] \tag{2.53}$$

where Q is a parameter that has the dimensions of $energy \times (time)^2$ and determines the time scale of the temperature fluctuation and X is the number of degrees of freedom.

Periodic Boundary Conditions

In order to simulate the macroscopic behavior of the system under investigation, it is important that the system boundaries are handled correctly. There are several methods to dealing with this problem, but the most common are harmonic boundary conditions and periodic boundary conditions. As it is more common to perform molecular dynamics simulations with the latter type of conditions, it is discussed in more detail.

When we use periodic boundary conditions, we divide the simulation domain into boxes, all of which are exact replicas of the central box to form an infinite lattice. In our simulations, we only look at the molecules of the central box, or original box. If, during the simulation, a particle moves in the central box, its periodic image in each of the neighboring boxes moves in exactly the same way. Thus, if a particle leaves the central box, one of its images will enter through the opposite side, as shown in figure 2.5. Therefore, there is in fact no wall at the boundaries of the central box. The number of particles in the central box is therefore preserved. The box simply forms a convenient axis system for measuring the coordinates of the N particles[114]. Fortunately, it is not necessary to store the coordinates of all particle images, which would be an infinite set, because when a particle leaves the central box by crossing a boundary, attention is focused on the image that has just entered the central box.

In other words, periodic boundary conditions mean that the system is its own neighbor in all dimensions. This can be seen either as a universe made up of an infinite number of similar systems, or as a universe that is the system itself. The simplest way to implement periodic boundary conditions is to use the cubic cell, but different shapes are possible (such as the hexagonal prism cell or the rhombic dodecahedral cell).

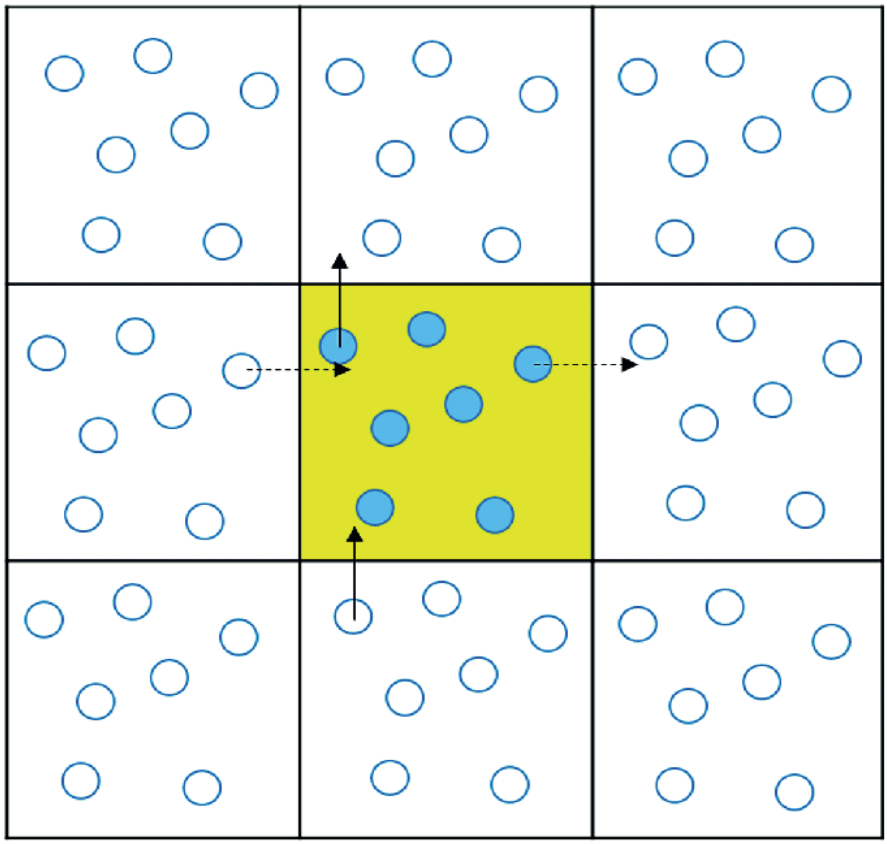

Figure 2.5: Two-dimensional representation of periodic boundary condition. The central cell (filled with yellow) represents the simulation box. Filled circles represent particles in the simulation box and open circles represent their periodic image in other cells. Bold and dashed lines shows movement of two particles near the boundary; as a particle leaves the simulation box, its image enters the box from the opposite end[113].

Not only is the movement of the particles limited by these periodic boundary conditions, but the interactions between the particles are also treated in the same way. It is therefore important to ensure that the size of the box is chosen in such a way that the particle cannot ”feel” its own image in the neighboring box and thus influence its own behavior.

Moreover, when calculating the interaction between a certain particle and another one, it is necessary to make sure to take the correct image of the other particle, so that the smallest distance between the particle and one of its images is calculated. This prerequisite is known as the minimum image convention. In the minimum image convention, each particle ”sees” at most one image of every other particle in the system (which is repeated ad infinitum through the periodic boundary conditions), and the interaction is computed with the nearest particle or image.

The use of the periodic boundary conditions and the minimum image convention ensures that the macroscopic behavior of the system is maintained, if we have chosen the box size correctly. A major disadvantage, however, is that fluctuations having a wavelength greater than the box length cannot be realized, because they do not fit into the periodic lattice, which can be a problem when approaching the critical point of a given fluid. However, the periodic boundary conditions model most systems well.

2.5 Force Field

As we have mentioned above, effective interactions between molecules need to be taken into account by using an empirical interaction model, called a force field. Depending on the properties and precision required, the molecular descriptions used in molecular simulations can go from the description of electrons up to simple hard sphere description. Normally, classical force fields consist in considering the molecular structure at upper level than a quantum description, with an explicit description of atoms or molecules. In ideal conditions, the force field should be simple enough to be evaluated quickly, but also precise enough to produce the properties of the system under study. The simplified treatment of the potential energy is achieved by empirical force field, whose mathematical formulation is imposed and parametrized on experimental data, such as X-ray and NMR[iii][115, 116]. In general, an empirical force field is described as the sum of two main contributions: non-bonded interactions and bonded interactions.

2.5.1 Non-Bonded Interactions

Non-bonded interactions represent the interactions of particles separated by more than two bonds. Generally, it is described as:

$$U_{inter} = U_{dispersion} + U_{repulsion} + U_{coulomb} \tag{2.54}$$

where U_{disp} represents the interactions of long range attraction due to polar momentum, $U_{repulsion}$ represents short range repulsion due to steric exclusion and $U_{coulomb}$ corresponds to Coulomb electrostatic interactions between charges of particles.

In our work, we use classical Lennard-Jones[117] 12-6 force field with electrostatic potential term, which is modeled using pair interactions between two force centers i and j of the same type

[iii] Nuclear Magnetic Resonance

of particles:

$$U_{LJ}(r_{ij}) = 4\epsilon \left[\left(\frac{\sigma}{r_{ij}} \right)^{12} - \left(\frac{\sigma}{r_{ij}} \right)^{6} \right] + \frac{q_i q j}{4\pi\epsilon_0 r_{ij}} \tag{2.55}$$

where σ corresponds to the distance at which the interaction potential between the two force centers is zero, and ϵ is the maximum amplitude of the potential well located at $r_{ij} = 2^{1/6}\sigma$. $q_{i,j}$ are the charges of particles i, j and ϵ_0 is the dielectric constant. In this expression, the term r^{-6} represents the attractive interactions between two particles which is justified by atom interaction theory. The term r^{-12} represents the repulsion due to the exclusion of PAULI[118].

2.5.2 Combining rules

The σ and ϵ in Lennard-Jones 12-6 force fields are given for force center of the same type. Interactions between unlike force centers are estimated using combining rules. For different types of particles, the Lennard-Jones parameters between unlike particles of type i and j are calculated with the Lorentz-Berthelot[119] rules:

$$\epsilon_{ij} = \sqrt{\epsilon_i \epsilon_j} \quad \sigma_{ij} = \frac{\sigma_i + \sigma_j}{2} \tag{2.56}$$

2.5.3 Truncation of Interactions

In our work, we perform simulations of a system with short range interactions. In this context, short range means that the total potential energy of a given particle is dominated by interactions with neighboring particles that are closer than the cutoff distance r_c. In this case, we have the expression as:

$$\begin{aligned} U^{truncation}(r) &= U_{LJ}(r) \qquad r \leq r_c \\ &= 0 \qquad\quad\ \ r > r_c \ , \end{aligned} \tag{2.57}$$

The error that results when we ignore interactions with particles at larger distances can be made arbitrarily small by choosing r_c sufficiently large. In our work, we use periodic boundary conditions. Thus, the case for which r_c is less than $L/2$ (half the diameter of the periodic box) is of special interest because in that case we only need to consider the interactions of a given particle only with the nearest periodic image of other particles. If the intermolecular interaction is not rigorously equal to zero for $r \geq r_c$, truncation of the intermolecular interactions at r_c will result in a systematic error. To correct this error, we can add a tail contribution. For the Lennard-Jones

12-6 potential, the tail contribution can be expressed as:

$$U^{tail} = \frac{8}{3}\pi\rho\epsilon\sigma^3[\frac{1}{3}(\frac{\sigma}{r_c})^9 - (\frac{\sigma}{r_c})^3] \tag{2.58}$$

where ρ is the reduced density of system.

2.5.4 Bonded Interactions

In our work, we study the transport behavior of gas molecules through nanoporous graphene membrane. In order to accurately described the internal behavior of molecules, bonded potential are required. They are decomposed in three contributions:

- Bonded potential: used to model a covalent bond in a molecular structure depending on the bond stretching.
- Angle potential: used to model a defined angle between two bonds sharing a common atom depending on angle bending.
- Two types of torsion potentials are commonly distinguished: dihedral angle potentials and improper torsions. Both potentials rely on a quartet of atoms, bonded in one way or the other. A dihedral angle potentials depends on four consecutive bonded atoms, whereas the improper torsion depends on three atoms centered around a fourth atom. The dihedral angle potential is mostly used to constrain the rotation around a bond. The improper torsion is used to maintain chirality on a tetrahedral extended heavy atom or to maintain planarity of certain atoms. The main difference between both torsion potentials is the definition of the torsional angle and the functional form of the potential function.

2.6 Advanced Techniques Used in Molecular Dynamics

2.6.1 Widom Method

The knowledge of chemical potential is sometimes necessary for the simulation of different phenomena such as phase equilibria and transport processes such as diffusion. These phenomena are important in the conception and design of many industrial processes, particularly in the field of transport and adsorption of fluids in nanoporous materials which is the subject of this work.

In order to maintain constant pressures in the upstream and downstream reservoirs when using the DCV-GCMD[iv] method, the chemical potential of the fluid in different reservoirs is

[iv] Dual Control Volume Grand Canonical Monte Carlo, described in section 2.7

controlled. To do this, we impose a constant chemical potential in the reservoirs, which are located at finite distance from nanoporous membranes, via insertions and deletions in the grand canonical ensemble. In this work, the pressure control of the fluid in reservoirs was done by imposing calculated chemical potentials in the NVT ensemble.To do this, we used the Widom method[120, 121, 122] which consists in inserting a fictitious particle rejected at each insertion test to derive the chemical potential by calculating the differential of the free energy of Helmholtz given by equation 2.22.

For the insertion of a Widom particle, in the NVT ensemble, the chemical potential can be deduced as follows:

$$\mu_i = \frac{\partial A}{\partial N_i} = -k_B T \ln(\frac{Z_{N+1}}{Z_N}) \tag{2.59}$$

This equation can be translated into:

$$\begin{aligned} \mu_i &= -k_B T \ln(\frac{V}{\Lambda^3(N+1)}) - k_B T \ln\left[\exp(-\Delta U_i / k_B T)\right] \\ &= \mu_{id} + \mu_{ex} \end{aligned} \tag{2.60}$$

where the term μ_{id} represents the ideal chemical potential, while μ_{ex} represents the excess chemical potential linked to the insertion of the widom particle. The term ΔU_i represents the change in total potential energy of the system of N particles if one particle is inserted. During the simulation, no particle is actually added and the value of ΔU_i is calculated by randomly inserting a fictitious particle of the species whose chemical potential we want to calculate. The average value is computed by averaging over several insertion attempts.

In our simulations, we used this techniques at different temperature and pressure in NVT ensemble by adding a home-made code to LAMMPS.

2.6.2 ABF Method

In molecular simulations, it is frequently desired to calculate potential energy changes along a one dimension trajectory or on a two dimension surface. The trajectory and surfaces are chosen because they characterized the process of interest. In our work, we study the transport behavior through nanoporous material. In such system, it is common that Boltzmann sampling does not allow for proper exploration of phase space, thus yielding statistical averages that exhibit strong dependence on initial conditions. This appearance of non ergodicity is often caused by high energy barriers, which are quite normal in nanoporous material, separating different volumes of phase space.

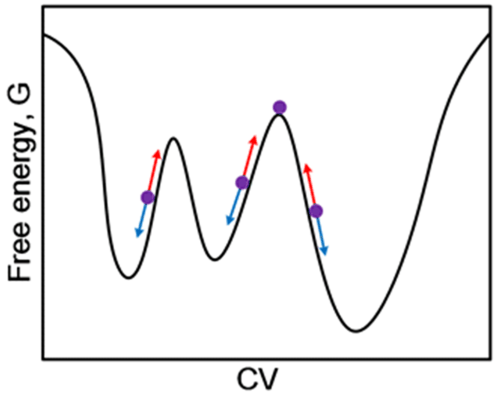

Figure 2.6: Schematic representation of the ABF method. The purple dots represent different states along the CV(Collective Variables). The blue and red arrows represent instantaneous mean forces and external biasing forces, respectively[123].

The ABF[v] method aims to improve the efficiency of molecular dynamics simulations to compute the profile of potential energy with the presence of high energy barriers. As shown in Figure 2.6, it applies a biasing force on the target particle to make it translocate from the low to high potential state by overcoming the energy barrier. In this work, we employed the ABF method[124, 125], implemented in LAMMPS/colvars package[126].

2.7 Post-treatment Algorithm to Compute Transport Coefficient

In our work, to characterize the permeability of the membrane to different gas species, we define a transport coefficient. In this section, we introduce the definition of this transport coefficient and the post-treatment algorithms used to compute it from MD simulations.

2.7.1 Transport Coefficient

In our work, to better understand the behavior of transport of gas through nanoporous graphene membrane, a diffusion transport coefficient in the linear regime is defined via Fick's law:

$$j = \Lambda \Delta \rho \tag{2.61}$$

[v] Adaptive Biasing Force

where the diffusion transport coefficient Λ relates the molecular flux density J to the number density difference across the membrane $\Delta\rho$. The SI unit of Λ is ms^{-1}.

In many works[44, 127, 87, 128], permeance of single-layer membranes Π is used to estimate the transport behavior. Π is defined in units of $mol\ Pa^{-1}\ s^{-1}$ as:

$$J = \frac{N_A}{S_w}\Pi\Delta P \tag{2.62}$$

where S_w is the surface area of the single-layer nanoporous membrane. N_A is Avogadro's number and ΔP is the pressure jump across the membrane. Equating the molecular flux densities in equation 2.61 and equation 2.62 yields the contribution of molecular diffusion to the permeance:

$$\Pi = \frac{S_w\Delta\rho}{N_A\Delta P}\Lambda \tag{2.63}$$

When we need to compare our results with other results in the literature, we can simply relate transport coefficient to permeance with equation 2.63 by means of the equation of state of the gas.

2.7.2 Comparison between NEMD and EMD simulations

In our work, we use both Non Equilibrium Molecular Dynamics (NEMD) and Equilibrium Molecular Dynamics (EMD) simulations. The difference between these two methods are introduced in this section.

For the NEMD simulations, system is maintained out of equilibrium upon imposition of a constant density difference between gas reservoirs (Figure 2.7 a). For this kind of simulations, it is similar to a realistic experiment, where the flow mechanism is emergent. Computation of Λ is directly achieved from flux/force equation and it considers all the contributions to the mechanism.

For EMD simulations, the system is maintained at thermodynamic equilibrium, where densities between gas reservoirs are constant(Figure 2.7 b). For this kind of simulations, no net flux but only thermal fluctuations at equilibrium can be observed. This means molecular diffusion is the only mechanism for transport of gas through nanoporous membrane during EMD simulations. Computation of Λ is inferred from the fluctuation relaxation time. More details about these two kinds of simulations and related post-treatment algorithms are introduced in next section.

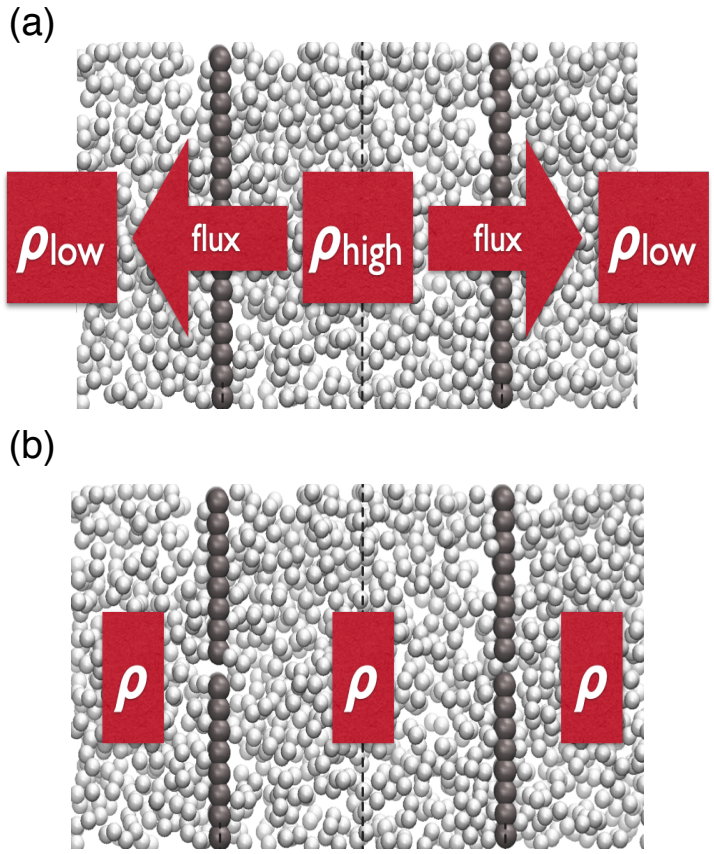

Figure 2.7: Illustration of NEMD (a) and EMD (b) simulations.

2.7.3 Post-treatment Algorithm to Compute Λ

Post-treatment Algorithm of NEMD

In NEMD simulations, we use the DCV-GCMD[129] method. This method employs two local control volumes for chemical potential control via particle insertion/deletion as in grand canonical Monte Carlo (GCMC) simulations. The control volumes are inserted in a standard NVT molecular dynamics simulation yielding a simulation with stochastic chemical potential control that may be thought of as a hybrid GCMC/MD approach. Restricting the insertions and deletions to two separate control volumes, one can apply different chemical potential in distinct locations, and thus create chemical potential gradients.

In our simulations, we define the control volumes in two reservoirs, which are located at a distance which is larger than cut off distance. The central reservoir and lateral reservoir are considered as the upstream and downstream reservoirs, respectively. With the DCV-GCMD method implemented in LAMMPS, a proper adjustment of the number of insertion/deletion trial

moves per time steps is required . A too small or too large value would distort the computation of flux. In our simulation, this ratio is of the order of 10. For a system out of equilibrium, the transport coefficient is computed directly from equation 2.61. We compute the molar flux instead by counting the velocity of molecules in a region comprised between two cross sections of the simulation box. The flux is defined as:

$$j = \frac{\sum v}{2SlN_A} \tag{2.64}$$

where S and l are the surface of simulation box and a small distance between two cross sections, respectively. In our system $l = 0.5nm$, while and the factor $\frac{1}{2}$ means that we used one region on each side of the membrane to compute the flux.

Post-treatment Algorithm of EMD

The previous computation of diffusion coefficients from Equilibrium Molecular Dynamics (EMD) simulations usually relies on two classical approaches, either based on the Einstein relation or the Green-Kubo formalism[105]. Both methods require that fluid particles diffuse during a sufficiently long time in a well-defined volume of space, be it in the bulk of a fluid, at the interface between two fluids[130, 131], near solid surfaces[132, 133] or inside porous materials[134, 135, 136]. When dealing with the permeation of fluids through vanishingly thin planar interfaces however, the volume of space in which fluid particles diffuse is ill-defined and, aside from the specific case of incompressible fluids[137], a diffusion coefficient cannot be determined unambiguously from EMD simulations. To solve these problems, a method proposed by Vermorel et al.[138] is applied in this work. This method requires minimal outputs from the simulation and is mostly based on a post-treatment algorithm.

The computation is based on a post-treatment algorithm that reconstructs homogenized fluid concentration transients between the reservoirs at equilibrium, $C(t)$, and computes their characteristic relaxation time, τ (see Figure 2.8 (a) and (b)). By homogenized, we mean that the algorithm acts as if the mixing of the gas molecules in each reservoir were instantaneous. Indeed, the algorithm does not track the ID of individual molecules, but only detects crossing events to generate virtual concentration profiles. As a result, any molecule that crosses the membrane contributes to the transport coefficient, regardless of the time elapsed between successive crossing and re-crossing of the interface by that same molecule. For this very reason, This technique can isolate the contribution of barrier crossing process. We will use the notation Λ_{cross} to refer to the transport coefficient computed with this technique. As shown in Figure 2.8 (c), Λ_{cross} is deduced

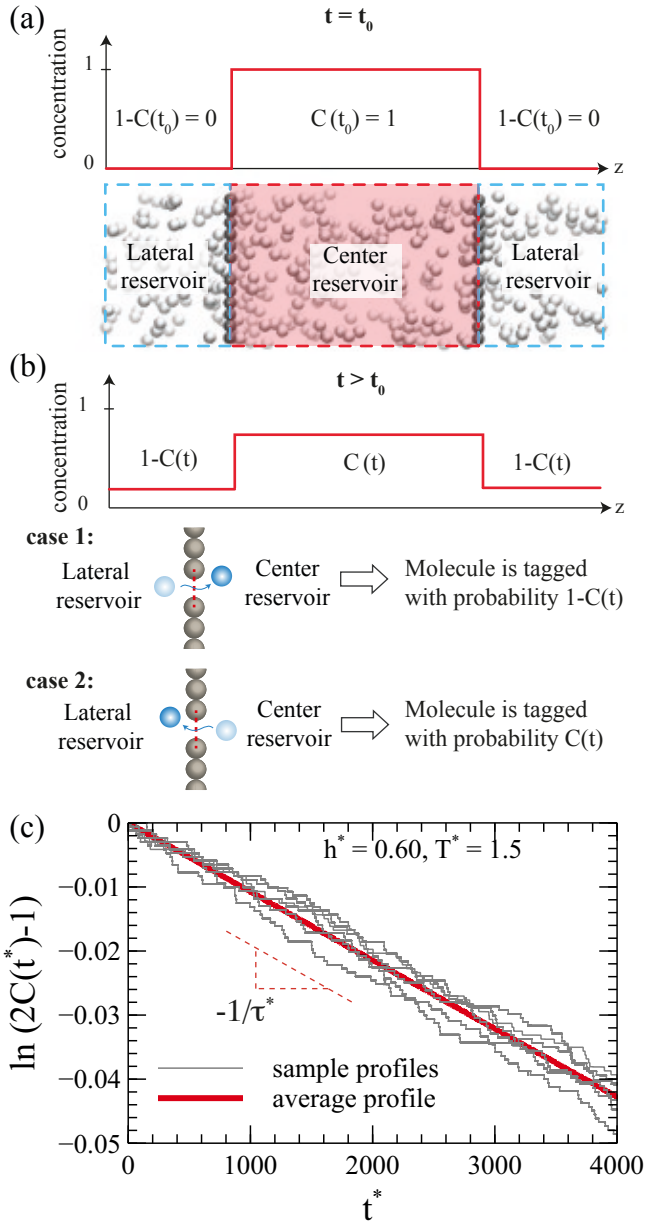

Figure 2.8: (*a*) At a given time origin t_0 the post-treatment algorithm sets the concentration to 1 in the center reservoir and 0 in the lateral reservoir, as if the center reservoir were filled with a uniform concentration of tagged molecules. (*b*) At subsequent times $t > t_0$, the concentration is $C(t)$ in the center reservoir and $1 - C(t)$ in the lateral reservoir. The algorithm tags each molecule that crosses the membrane with a probability $1 - C(t)$ if it goes from the lateral to the center reservoir (case 1), or with a probability $C(t)$ if it crosses the membrane in the opposite direction (case 2). $C(t)$ is then updated before processing to the next time step. (*c*) Typical concentration relaxation profiles computed by the post-treatment algorithm. Grey solid lines stand for individual sample profiles reconstructed from single time origins. The red solid line stands for the concentration profile averaged over multiple time origins.

from the transient concentration profile expressed as

$$C(t) = \frac{1}{2}\left(1 + e^{-t/\tau}\right), \quad \text{with} \quad \Lambda_{cross} = \frac{L}{2\tau}\,. \tag{2.65}$$

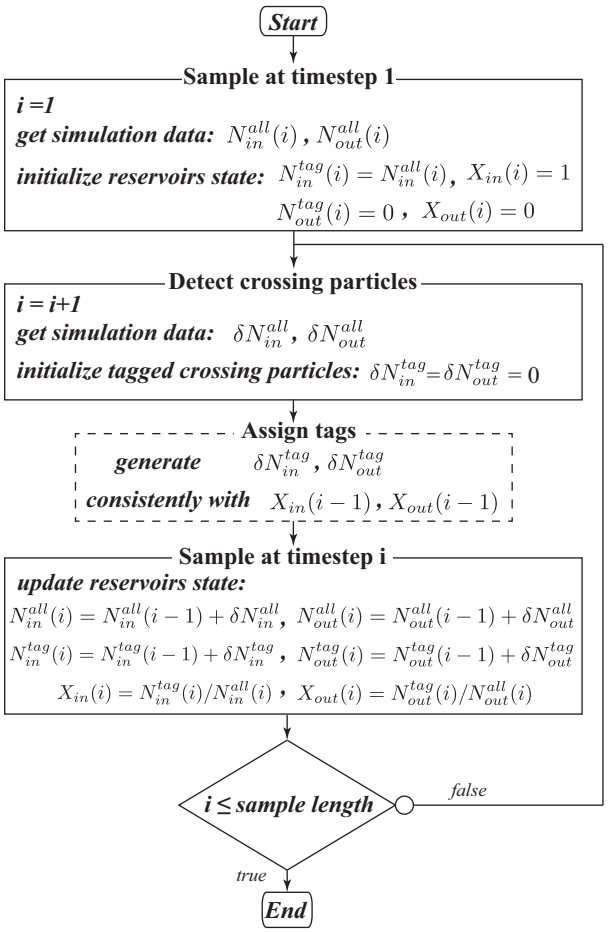

Figure 2.9: Post-treatment algorithm scheme for the generation of one sample corresponding to a single time origin. The treatment in the dashed block is detailed in Figure 2.10[138].

The main algorithm of the post-treatment is shown in Figure 2.9. This algorithm intends to generate transient molar fractions $X_{in}(t)$ and $X_{out}(t)$ of virtually tagged particles, in the central and lateral reservoirs respectively, just as if the concentrations of tagged particles were spatially uniform in each reservoir at any time step. Our technique is reminiscent of the "color" diffusion scheme first devised by Holian[139], yet different, as it exploits the transient response of the system. In our notations, subscripts *in* or *out* denote the central or lateral reservoir respectively, superscript *tag* denotes tagged particles and superscript *all* denotes all fluid particles, wether tagged or not.

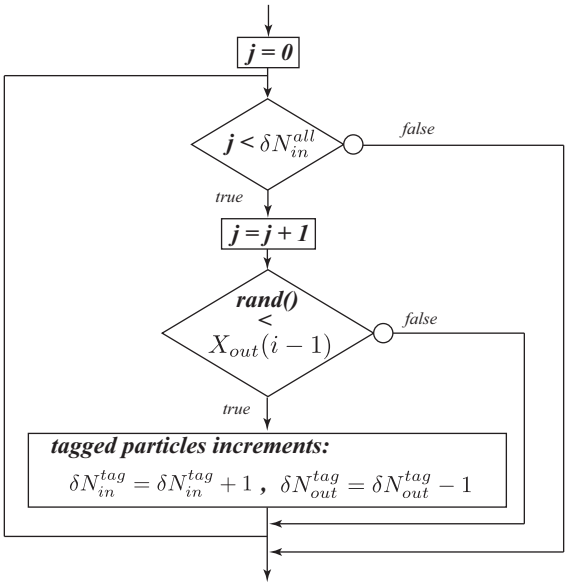

Figure 2.10: Assignment of tags to particles entering the central reservoir. We use a reciprocal algorithm to assign tags to particles leaving the central reservoir[138].

2.7.4 Relative Errors of Λ_{cross} Computed from EMD Simulations

A remarkable point is that relative errors of Λ_{cross} computed from EMD simulations by our post-treatment algorithms are below 1% when the runtime of simulations is superior to $5 \times \tau$. Nevertheless, our post-treatment algorithm considered the the central and lateral reservoirs are always in equilibrium. In fact it is not exact during our simulations with realistic graphene-gas system. We found that the difference of molecular number in different reservoirs can reach 40%. In this situation, there exists a transient driving force biasing the results of EMD simulations and our post-treatment algorithm will underestimate the relative error. To obtain the representative relative error of Λ_{cross}. We perfomed simulations with sufficient time steps and we observed several cycles of difference of molecular number between the two reservoirs. We used our post-treatment algorithm to compute Λ_{cross} for each cycle, then we computed the standard deviation of all the Λ_{cross}. In our work, the maximum percentage of relative error is about 35% (i.e. $CO_2 - Pore13a$). Details are given in Table 2.2 to Table 2.5.

	$CO_2 - Pore13a$	$CO_2 - Pore16a$	$CO_2 - Pore24a$
Standard deviation	0.002788	0.03409	2.3901
Average	0.007848	0.1679	8.4573
Percentage	35.52%	20.31%	28.26%

Table 2.2: Errors of Λ for CO_2 at 300K with different pore sizes.

	$CH_4 - Pore13a$	$CH_4 - Pore16a$	$CH_4 - Pore24a$
Standard deviation	n/a	0.02528	1.658
Average	n/a	0.1294	7.0255
Percentage	n/a	19.53%	23.6%

Table 2.3: Errors of Λ for CH_4 at 300K with different pore sizes.

	$O_2 - Pore13a$	$O_2 - Pore16a$	$O_2 - Pore24a$
Standard deviation	0.03881	0.09514	0.9794
Average	0.194	0.7578	8.4573
Percentage	20.08%	12.55%	25.8%

Table 2.4: Errors of Λ for O_2 at 300K with different pore sizes.

	$N_2 - Pore13a$	$N_2 - Pore16a$	$N_2 - Pore24a$
Standard deviation	0.022	0.1231	0.6684
Average	0.07681	0.5706	3.1954
Percentage	28.64%	21.58%	20.92%

Table 2.5: Errors of Λ for N_2 at 300K with different pore sizes.

Chapter 3

Theoretical Modeling of Transport Coefficient through 2D Single-layer Membranes

Contents

In chapter 1, a wide range of pore sizes were introduced. With these variety of pore sizes, gas permeation through 2D single-layer membrane are likely to be span different regimes, including molecular sieving, crossover and effusion. As mentioned in chapter 2, we defined a transport coefficient to qualify the permeability of membranes. In theory, it is important to propose a complete and proper model, which should provide a mathematical relation between the transport coefficient and relevant parameters describing various gas-pore combinations. With this kind of theoretical model, one can expect to predict the transport and separation properties of the membrane and then guide the design of pore structure, optimized for target applications.

Most studies found in the literature focus on the molecular sieving regime because it is more likely to achieve high selectivity[127, 44, 87]. Their analytical frameworks are based on transition state theory (TST)[140, 141] and they propose theoretical models based on semi-empirical Arrhenius-type equations. Yuan et al[142] proposed a serial model, which provide insights into

the gas permeation in different regimes. Nevertheless, their theoretical model is based on several assumptions introducing numerous empirical parameters. This kind of approach thus requires adjusting multiple parameters which depend on the permeation regime. In this chapter, we introduce another theoretical model which pertains to all kinds of permeation regimes. At this point, it is fully predictive for the molecular sieving and the effusion regime, but requires some development to tackle the crossover regime.

3.1 Theoretical Model for the Transport Coefficient

The permeation of gas molecules through 2D membranes can be decoupled into two steps: (1) barrier crossing through the pore and (2) desorption to the bulk region. Similar cross-desorption process have been proposed by Tian et al[143] and Yuan et al[44]. For the cross-desorption process, we propose the following expression for the transport coefficient:

$$\Lambda = P_{des}\Lambda_{cross} \tag{3.1}$$

where Λ_{cross} stands as the transport coefficient accounting for the barrier crossing process. P_{des} is the probability of that a molecule desorbs from the pore mouth region after the barrier crossing process. In the molecular sieving regime, $P_{des} \approx 1$ because the energy barrier is high and the barrier crossing process is rate-limiting due to its slow kinetics. On the other hand, P_{des} approaches a value of 1 in the effusive regime because the desorption process only concerns a minority of permeating molecules. In the crossover regime, $P_{des} < 1$ and it cannot be neglected to predict the transport coefficient accurately. Currently, there is no accurate model for P_{des}. In the next chapter, we will investigate the influence of desorption and compute P_{des} from first passage times statistics. A theoretical model for Λ_{cross} was proposed by Oulebsir et al[144]. In this work, we applied it to a simplified system (chapter 4) and realistic graphene-gas system (chapter 5). The following section details how we apply it to these two molecular systems.

3.2 Theoretical Model for Λ_{cross}: Computation for Simplified System

Figure 3.1 shows an illustration of the simplified system, which is the same system as the one introduced in chapter 4. In this system, two immobile solid walls with a slit opening of controlled width h stand as the planar interfaces under investigation. Fluid and solid molecules are described

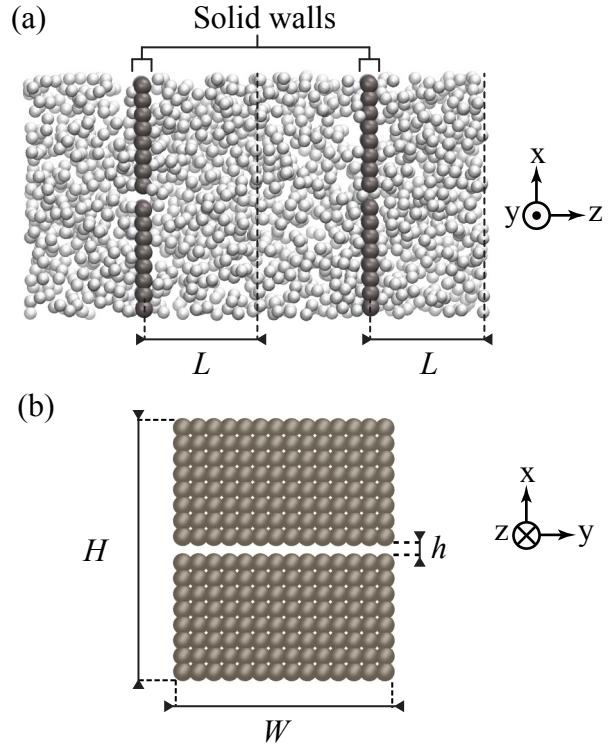

Figure 3.1: Basic features of the system under study. (a) Snapshot of the simulation box in the xz plane. Periodic boundary conditions are applied in all directions. (b) Snapshot of one solid wall in the xy plane.

as simple Lennard-Jones (LJ) spheres with a truncation of the interactions at $r_{ij} = r_c = 2.5\sigma$,

$$\begin{aligned} U_{LJ}(r_{ij}) &= 4\epsilon \left[\left(\frac{\sigma}{r_{ij}} \right)^{12} - \left(\frac{\sigma}{r_{ij}} \right)^{6} \right] \qquad r_{ij} \leq r_c \\ &= 0 \qquad\qquad\qquad\qquad\qquad\qquad r_{ij} > r_c \ , \end{aligned} \tag{3.2}$$

where the same potential parameters ϵ and σ were used to describe both fluid/fluid and fluid/solid interactions. In the following of this chapter, our simulations data are expressed in standard LJ reduced units [105] and dimensionless variables are written with an asterisk in superscript (see the appendix for the definition of the reduced units). More details about this molecular system will be introduced in chapter 4.

According to the model of Oulebsir et al. the coefficient Λ_{cross} is written in the following form

$$\Lambda_{cross} = \frac{\bar{v}}{4} \, \phi \, \Gamma. \tag{3.3}$$

where $\bar{v} = \sqrt{8kT/\pi m}$ is the thermal velocity, ϕ is the surface porosity of the 2D membrane

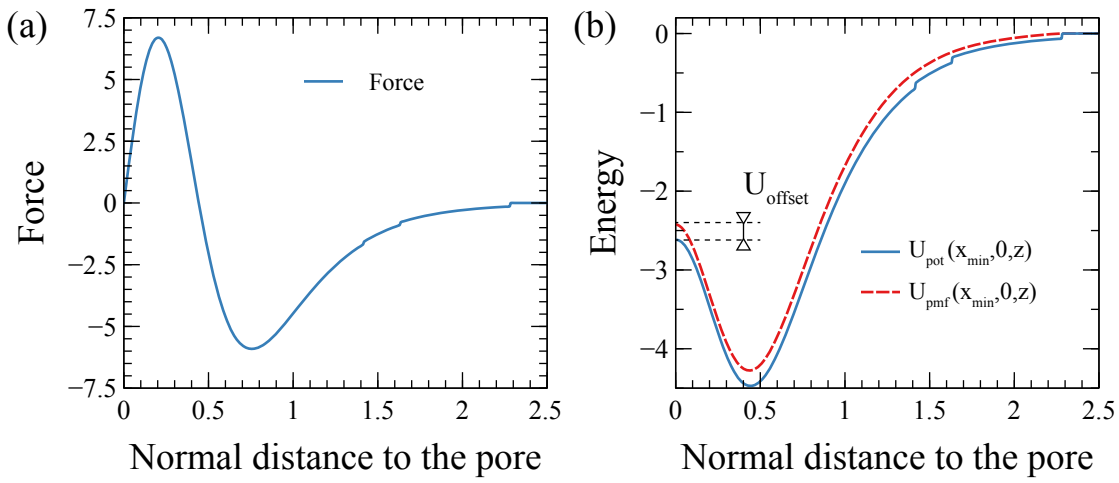

Figure 3.2: Force and energy profiles for a single gas molecule interacting with membrane atoms. In this example, the pore width is $h^* = 0.60$. (a) Projection of the force acting on a single gas molecule along a trajectory perpendicular to the membrane and passing through the point of lowest potential energy in the plane of the pore. (b) Potential energy (blue solid line) and PMF (red dashed line) of a single gas molecule along the same trajectory. U_{offset} is the energy difference between the potential energy and the PMF at the point of lowest potential energy in the plane of the pore.

accessible to permeating gas molecules and Γ is a thermodynamic correction factor that accounts for the increase of gas density near the pore entrance due to adsorption effects. The parameters ϕ and Γ depend directly on the potential of mean force (PMF) between a permeating molecule and the constituent atoms of the membrane[144]. In the case of gas permeation, we assume that the PMF is comparable to that of a single gas molecule interacting with the membrane. Therefore, the PMF can be calculated directly from the potential energy of interaction. In our case, the potential energy is reduced to a sum of Lennard-Jones pair interactions between the gas molecule and each membrane atom within the cut-off radius ($r_c^* = 2.5$ in our work). Figure 3.2(a) shows the total force acting on a gas molecule along a trajectory orthogonal to the membrane and passing through the most probable crossing point in the pore plane, i.e. the one with the lowest potential energy. Discontinuities in the force profile can be seen as one moves away from the plane of the membrane, resulting from missing interactions beyond the cut-off radius. The integration of this force with respect to the normal coordinate to the membrane, from $z^* \to \infty$ to $z^* = 0$, gives the PMF along the trajectory orthogonal to the pore and passing through the most probable crossing point. Precisely because of the discontinuities related to the cut-off, the PMF

differs from the potential energy. This difference is materialized by a difference in energy U_{offset} observed in the pore plane at $z^* = 0$. It should be noted that for our system the point of passage of lowest energy corresponds to the center of the pore at $(x^* = 0, y^* = 0)$ for the smallest pore sizes, which is the case in Figure 3.2. However, when the pore size is large enough, the minimum energy observed in the plane of the pore splits into two minima located on the edges of the slit at $(x^* = \pm x^*_{min}, y^* = 0)$.

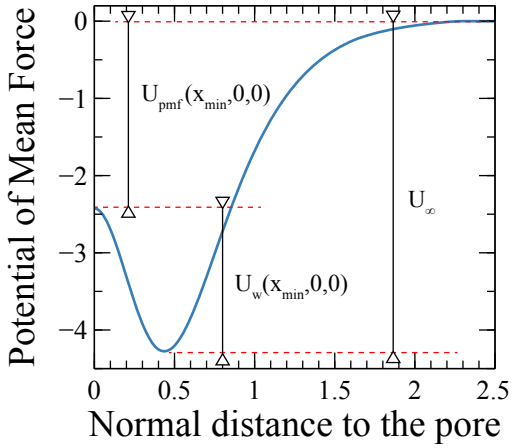

Figure 3.3: PMF of a single gas molecule along a trajectory perpendicular to the membrane and passing through the point of lowest potential energy in the plane of the pore. In this example, the pore width is $h^* = 0.60$.

From this one-dimensional PMF, we can define several energy differences shown in Figure 3.3, useful for the implementation of the theoretical model as we will show later. The first energy difference is referred to as U_∞ and corresponds to the difference in free energy that a gas molecule feels when it comes from the bulk of the reservoir to adsorb at the minimum of PMF in the vicinity of the pore entrance. The second energy difference is referred to as $U_w(x^*, y^*)$, which is the energy barrier required for a gas molecule to desorb from the PMF minimum and cross the pore at the point of coordinate $(x^*, y^*, 0)$. These quantities can then be used to define the ϕ and Γ parameters as

$$\phi = \frac{1}{HW} \int\int dxdy \exp\left(-\frac{U_w(x^*, y^*)}{kT}\right) \quad ; \quad \Gamma = \exp\left(\frac{U_\infty}{kT}\right) . \tag{3.4}$$

Although independently calculated ϕ and Γ allow a better physical interpretation of the physical mechanisms governing the passage of molecules through the membrane, the transport coefficient

can be calculated directly as

$$\Lambda_{cross} = \frac{1}{4HW}\sqrt{\frac{8kT}{\pi m}}\int\int dxdy \exp\left(\frac{U_{pmf}(x^*, y^*)}{kT}\right) \tag{3.5}$$

where $U_{pmf} = U_\infty - U_w$ stands for the direct evaluation of the PMF in the plane of the membrane, as shown in Figure 3.3. It should be noted that this two-dimensional PMF is none other than the potential energy of the single gas molecule in the plane of the membrane, corrected for the energy shift resulting from the 1D PMF calculation discussed above:

$$U_{pmf}(x, y) = U_{pot}(x, y, 0) + U_{offset} \tag{3.6}$$

Figures 3.4 and 3.5 show respectively the two-dimensional maps of Boltzmann's factors of the potential energy $U_{pot}(x, y)$ and the free energy barrier $U_w(x, y)$ in the plane of the membrane for a range of pore sizes. We see clearly how the single minimum of potential energy located in the center of the pore separates into two minima as the pore size increases. Moreover, when the pore size is large enough we observe that because of the cut-off radius there may be a region in the middle of the pore where the potential energy is zero, as shown in 3.4. This means that when the pore is large enough, some gas molecules can pass directly through the membrane without interacting with its atoms. We assume that the definition of the energy shift U_{offset} discussed above is not relevant for molecules permeating the membrane through this region. Therefore we will use the following definition of the energy U_{pmf} required for the calculation of Λ_{cross}:

$$U_{pmf}(x, y) = \begin{cases} U_{pot}(x, y, 0) + U_{offset}\ , & \text{if } U_{pot}(x, y, 0) \neq 0 \\ 0\ , & \text{otherwise} \end{cases} \tag{3.7}$$

Figure 3.5 shows the implication of such a definition, with the appearance of a band corresponding to the region in which we assume the flow is free of interatomic interactions. If the definition of this threshold may seem arbitrary, it seems necessary. Indeed, most of the molecules crossing the pore far from its edges transit directly from the inlet to the outlet reservoir without prior adsorption. Because we use a cut-off radius in our force field, this threshold is easy to define. The use of a force field with long-range interactions would probably require a finer criterion to delineate the area of the pore in which the interaction effects between the gas and the solid are expected to become negligible. By using the Lennard-Jones interaction potential and by knowing the positions of the constituent atoms of the membrane, we can then calculate the PMF given by equation 3.7. It is then sufficient to proceed to the numerical integration of the equation 3.5 by discretizing the surface of the pore in the (x, y) plane to calculate the transport coefficient Λ_{cross}.

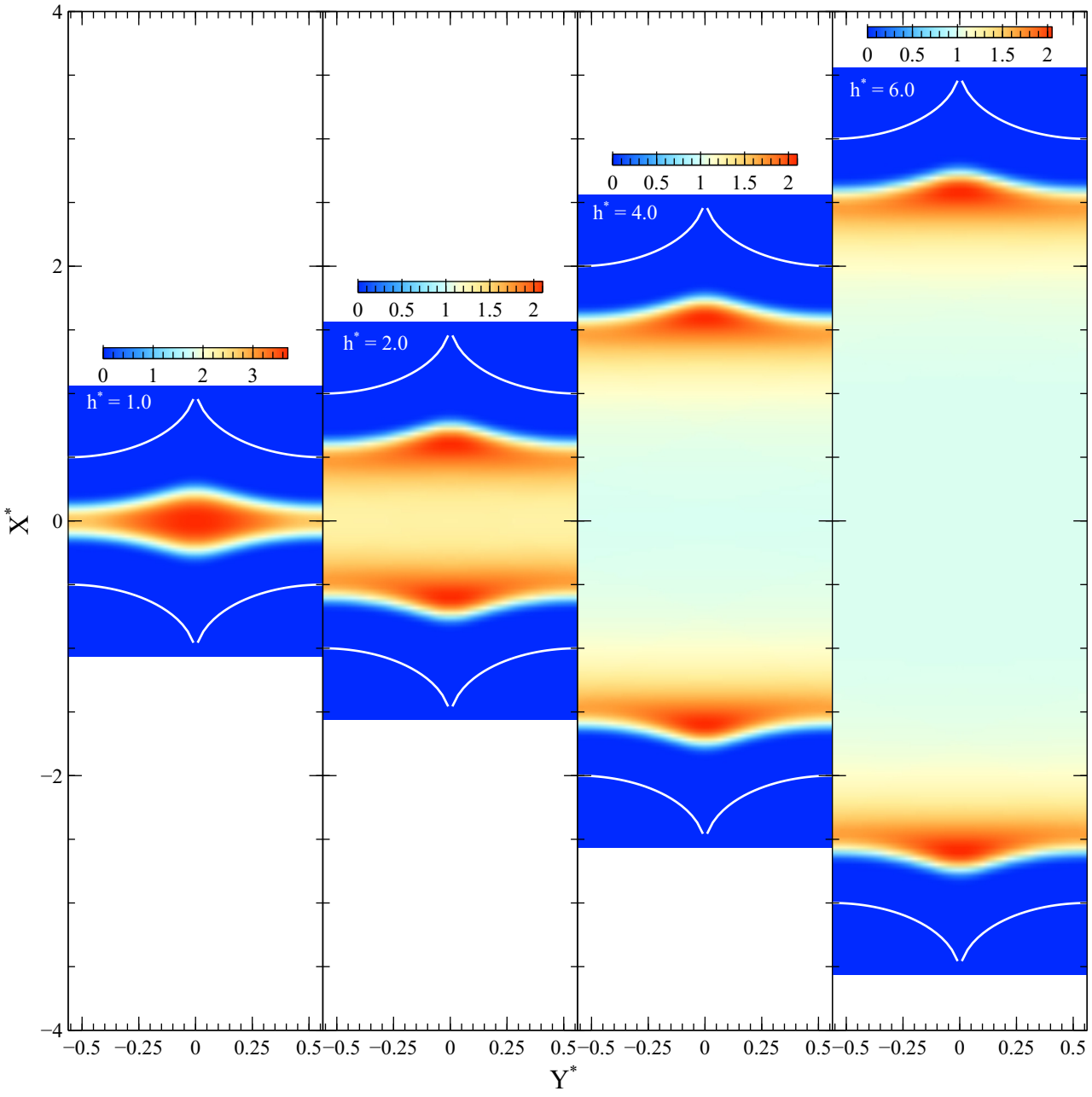

Figure 3.4: 2D map of boltzmann factors of the potential energy, $exp\left(-U^*_{pot}(x^*, y^*)/T^*\right)$, in the plane of the membrane for a range of pore sizes. White solide lines represent the edges of the membrane atoms taken at a reduced distance $2^{1/6}$ from their centers. In this example the temperature is $T^* = 3.0$.

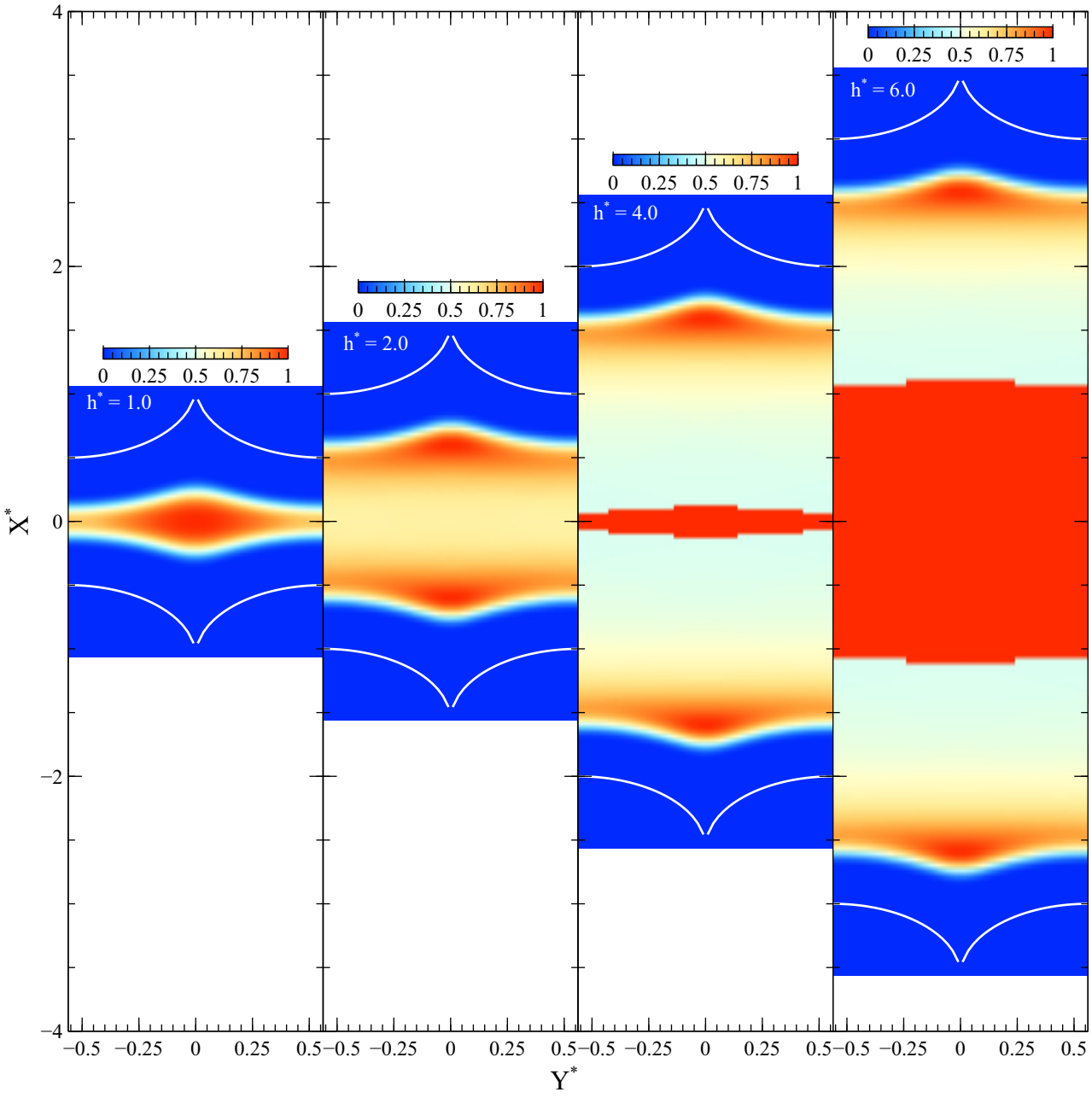

Figure 3.5: 2D map of boltzmann factors of the barrier energy, $exp\,(-U_w^*(x^*, y^*, 0)/T^*)$, in the plane of the membrane for a range of pore sizes. White solide lines represent the edges of the membrane atoms taken at a reduced distance $2^{1/6}$ from their centers. In this example the temperature is $T^* = 3.0$.

3.3 Theoretical Model for Λ_{cross}: Computation for Realistic System

For realistic graphene-gas system, we use the same theoretical model as described above. We can note that the computation of Λ_{cross} is based on the 1D and 2D PMF profiles. For the simplified system, the computation of PMF profile is straightforward as the gas molecules are spherical and the PMF only depends on the position of the gas molecule. For graphene-gas systems, if we perform simulations with united-atom gas models, we can also compute the PMF profiles directly and the methods used to compute Λ_{cross} is exactly the same as introduced above. However, for a more realistic system, we also investigated all-atom gas models. Because of the entropic contribution of rotational degrees of freedom, PMF profiles depend on the temperature and cannot be computed directly from the interaction potential. Hereafter, we will discuss the methods used to compute the PMF for all-atom gas models, as shown in Figure 3.6.

3.3.1 Methods Used to Compute $U_{pmf}(0,0,Z)$

To compute the profile of $U_{pmf}(0,0,Z)$, we applied an indirect method related to the local density profiles. Equation 3.8 is the relation between local density and PMF.

$$\frac{\rho(z)}{\rho_{bulk}} = exp(\frac{U_\infty - U_{pmf}(0,0,Z)}{KT}) \tag{3.8}$$

With eq 3.8, we could compute PMF profiles from local density profiles. The local density histograms were computed from unbiased NVT MD simulations by counting gas molecules in cylinder bins centered around a straight line that crosses the pore center and is normal to the graphene basal plane. We obtained convergence of density values for bin heights and radius smaller than 0.2Å. The bulk phase was defined as the region extending beyond 1 nm from the surface of the graphene sheet, so we compute the bulk density ρ_{bulk}as the average of density in the bulk region. The definition of the bulk phase can be verified by local density histograms, where the ratio of gas density profiles approach 1 when $z > 1nm$. We can also find the position z_{min} where the density reaches a maximum because the position of the density peak coincides with the minimum of PMF. The main objective for computing the $U_{pmf}(0,0,Z)$ is to find out U_∞ and U_w. To compute U_∞, we applied the density peak, where

$$\frac{\rho_{peak}}{\rho_{bulk}} = exp(\frac{U_\infty - U_{pmf}(0,0,z_{min})}{KT}) \tag{3.9}$$

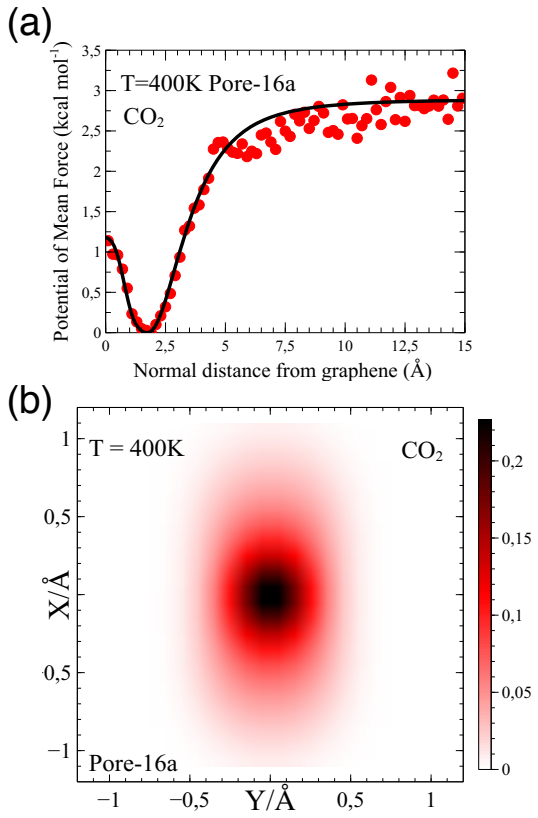

Figure 3.6: (a) PMF profile of $CO_2 - 16a$ in 400 K, The PMF is computed along the straight line $(0, 0, z)$ perpendicular to the graphene sheet and passing through the pore center. (b) Surface map of Boltzmann factors in the plane of the graphene sheet $z = 0$ of $CO_2 - 16a$ in 400 K.

We considered $U_{pmf}(0, 0, z_{min})$ as the reference, which means $U_{pmf}(0, 0, z_{min}) = 0$. U_∞ can be computed from eq 3.10.

$$U_\infty = KT \ln(\frac{\rho_{peak}}{\rho_{bulk}}) \tag{3.10}$$

To compute U_w, we applied eq 3.8 at $z = 0$, where

$$\frac{\rho_{z=0}}{\rho_{bulk}} = exp(\frac{U_\infty - U_w}{KT}) \tag{3.11}$$

With U_∞ obtained, U_w can be computed from eq 3.12.

$$U_w = U_\infty - KT \ln \frac{\rho_{z=0}}{\rho_{bulk}} \tag{3.12}$$

To obtain accurate enough U_∞ and U_w, the density peak and density in the center of pore were computed from the average number of gas molecules in the $z = z_{min}$ region and $z = 0$ region with

same sizes of cylinder bins. The time interval $\Delta t$for each counting was 1 ps and more than 10^6 countings were perfomed during a typical simulation. The errors of ρ_{peak} and $\rho_{z=0}$ are estimated by the block average method[105]. When the block length has an order of $1000\Delta t$, the error is uncorrelated. Therefore, the error bars of U_∞ and U_w are deduced from eq 3.10 and eq 3.12.

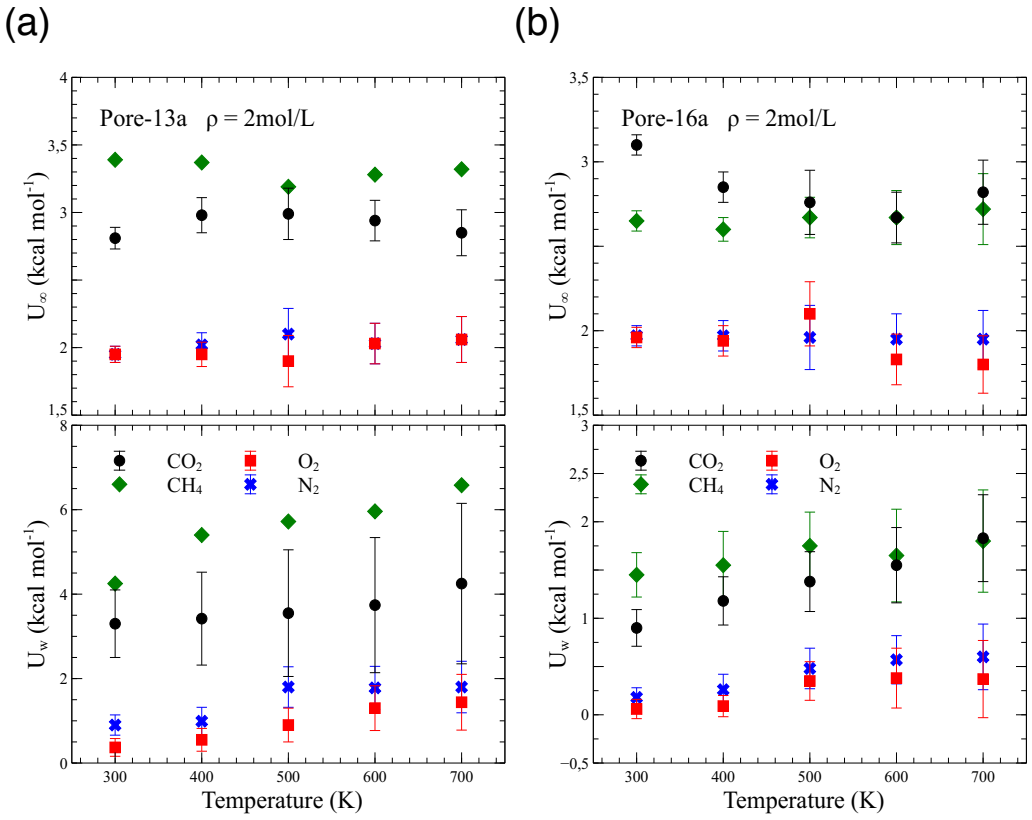

Figure 3.7: Evolution of the energy barrier U_∞ (top) and U_w (bottom) with temperature, the values are computed with original density 2mol/L. Symbols stand for different gas species, with pore size Pore-13a (a) and Pore-16a (b), respectively.

Figure 3.7 shows the results of U_∞ and U_w computed with this indirect method. We can observe that U_∞ and U_w depend on temperature because of the entropic contribution. The discrepancy between CO_2 (or CH_4) and O_2 (or N_2) is significant, suggesting that CO_2 and CH_4 are more prone to adsorption than O_2 and N_2. Meanwhile, similar behavior can be observed for U_w, suggesting that the energy barrier of O_2 (or N_2) is less than CO_2 (or CH_4). It means that molecules cross the pores more easily. With temperature increasing, U_w increases significantly while U_∞ exhibits similar values with different temperatures. With pore size shrinking from 16a to 13a, the impact on U_∞ is not significant as similar values can be observed with both pore sizes.

Nevertheless, we can observe that U_w increases rapidly when the pore size decreases.

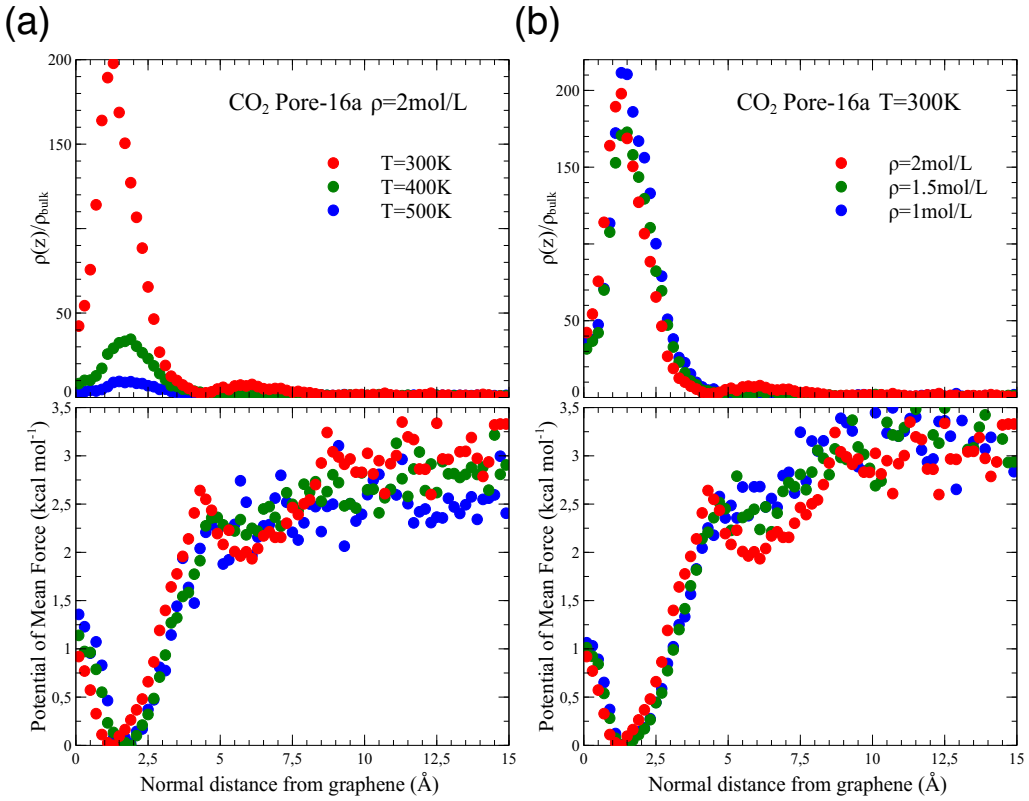

Figure 3.8: (a) Density (top) and PMF (bottom) profiles obtained with original density $\rho = 2mol/L$, symbols stand for the simulation data obtained for temperature ranging from 300 K to 500 K. (b) Density (top) and PMF (bottom) profiles obtained at $T = 300K$, symbols stand for the simulation data obtained for original densities ranging from 1mol/L to 2mol/L.

Figure 3.8 reports the details about the indirect method to compute the PMF by the profile of density ratio. Figure 3.8 (a) focuses on the effect of temperature. We note that the effect of adsorption decreases with increasing temperature. The profiles of PMF vary with temperature. It confirms that the PMF of non-spherical molecules depends on temperature, due to the entropic contribution of rotations.

We also investigated the impact of average densities for estimations of U_∞ and U_w. At $T = 300K$, we performed simulations with different densities of CO_2. We computed U_∞ and U_w and we found that there is no obvious difference considering the error bar(see Figure 3.9). It suggests that the gas/graphene interaction is the dominant interaction along the trajectory (0,0,Z) and that we are dealing with the dilute gas limit. In this work, we therefore use the average density

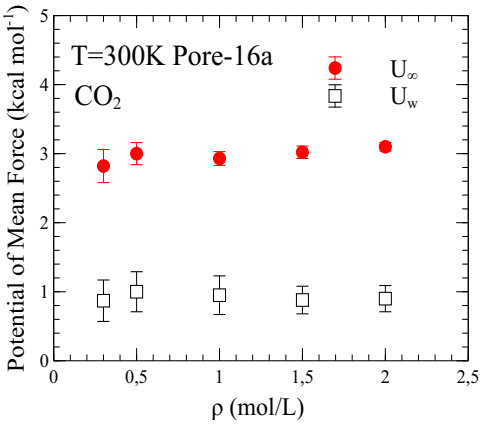

Figure 3.9: Evolution of the energy barrier U_∞ and U_w of $CO_2 - 16a$ with densities at T=300K.

$\rho = 2mol/L$ to compute U_∞ and U_w to decrease the statistic uncertainty.

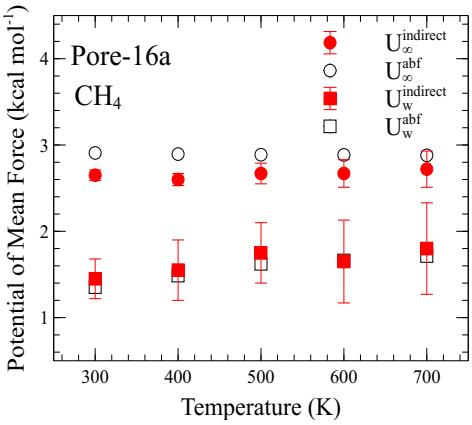

Figure 3.10: Comparison of computed U_∞ (top) and U_w (bottom) between ABF method indirect method for CH_4 with Pore-16a.

In addition, we can compute $U_{pmf}(0, 0, Z)$ directly by means of ABF simulations. The ABF technique consists in applying an external force field to targeted molecules in the simulation box. This external force field is adapted in the course of the simulation to compensate the actual force exerted by the rest of the system, which usually prevents molecules from accessing high free energy areas. Eventually, the external force field converges when the targeted molecules can explore all possible values of the reaction coordinate. We then performed a numerical integration of the biasing force field with respect to the reaction coordinate to compute the PMF, and then obtained U_∞ and U_w. Figure 3.10 compares the values of U_∞ and U_w computed by these

two methods. We note that U_∞ computed by ABF method is always a little higher than U_∞ computed by the indirect method while U_w has the opposite trend. It suggests that we always overestimate the value of Λ_{cross} by ABF method by a factor less than 2. Nevertheless, under extreme molecular sieving conditions, such as CH_4 with Pore-13a, we can use the ABF method to estimate Λ_{cross} and we will get the model predictions with correct order of magnitude. Slight discrepancies observed are most certainly due to the biased introduced during ABF simulations during which we constrain the dynamics of one molecule along an imposed trajectory. When the pore is definitely small for gas molecules, ABF simulations are recommended because we can not get accurate U_w due to no sufficient gas molecules crossing the pore.

3.3.2 Methods Used to Compute $U_{pmf}(X, Y, 0)$

With the 1D PMF profile, we can compute the isothermal thermodynamic factor, $\Gamma = (\partial\rho_{z_{min}}/\partial\rho)_T$. To compute the accessible surface porosity, the 2D PMF profile is required. Contrary to the computation of $U_{pmf}(0, 0, Z)$, we cannot continue to use density profiles to deduce PMF profiles because the surface of graphene is a region with high potential energy. We employed ABF method to solve this problem.

By means of ABF simulations, we computed the mean force on the surface of graphene(see Figure 3.11). To get the 2D PMF profiles, we need to integrate the mean force, which is a function of x and y. In this case, we use a transformation based on Poisson equation (see eq 3.13) and a post-treatment algorithm using the finite difference method to compute $U_{pmf}(X, Y, 0)$.

$$\frac{\partial^2 U_{pmf}}{\partial x^2} + \frac{\partial^2 U_{pmf}}{\partial y^2} = -div(\vec{F}(x, y)) \tag{3.13}$$

In the dilute gas limit, the fluid/fluid interaction can be neglected. In other words, to save the computational cost, a single gas molecule was simulated to calculate the force field on the surface of the graphene sheet. With these methods to compute the 1D and 2D profiles of PMF, we can infer the thermodynamic factor Γ and accessible surface porosity ϕ. Figure 3.12 reports the theoretical values of Γ and ϕ in Arrhenius plots. We note that these two parameters have opposite trend with temperature. It suggests that the transport behavior results from the competition between accessible porosity and adsorption. This competition could influence the trend of Λ_{cross} with temperature. Details will be discussed in chapter 5.

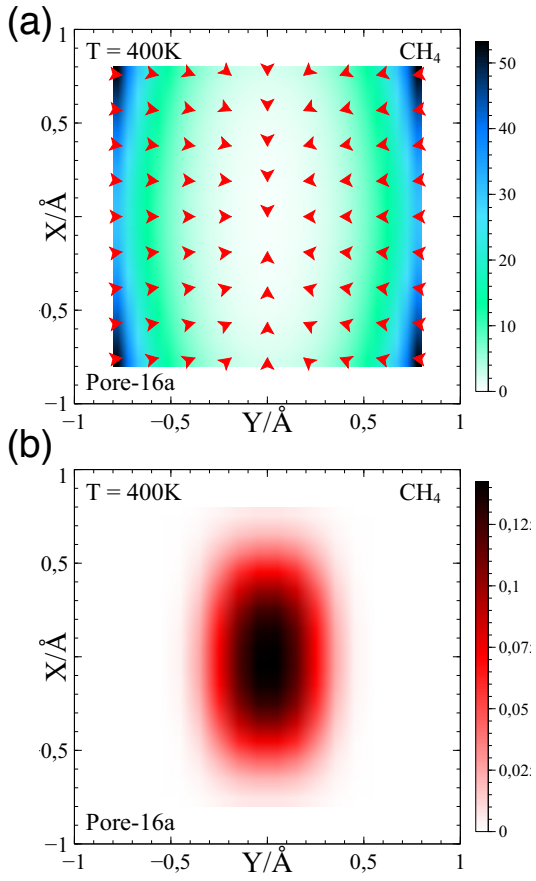

Figure 3.11: (a) Force field of CH_4 computed by ABF method in the plane of graphene sheet $z = 0$ with Pore-16a in 400 K, where the red arrows represent the force field and the colormap is the potential on the surface. (b) Surface map of Boltzmann factors in the plane of the graphene sheet $z = 0$ of $CH_4 - Pore16a$ in 400 K

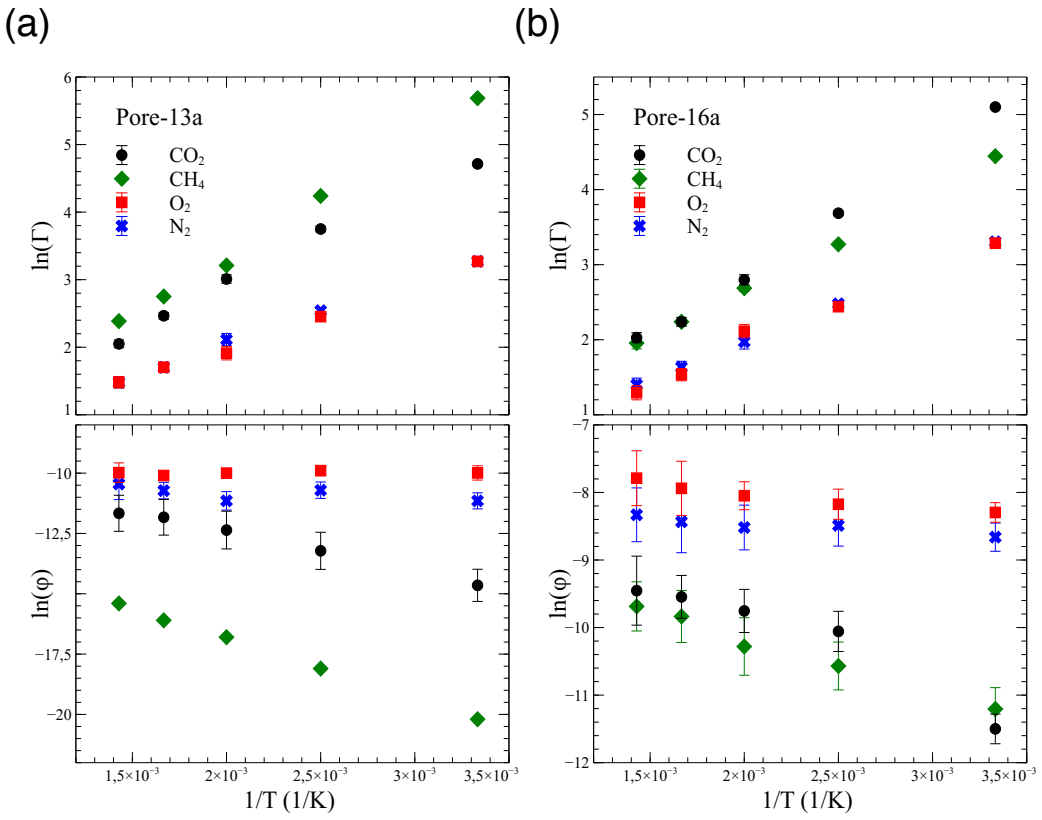

Figure 3.12: Evolution of thermodynamic factors Γ (top) and ϕ (bottom) with temperature in Arrhenius plots. Symbols stand for different gas species, with pore size Pore-13a *a* and Pore-16a *b*, respectively.

Chapter 4

Gas Permeation through Single-layer Simplified Graphene-like Membranes

Contents

Several research groups have used molecular simulations to investigate the sieving properties of nanoporous graphene membranes in the context of gas separation[87, 146, 147, 148, 149]. Various studies have used equilibrium molecular dynamics (EMD) to compute molecular fluxes under equilibrium conditions[87, 149, 146, 147]. For instance, Sun et al. simply averaged the absolute values of the molecular fluxes across the membrane obtained at a given equilibrium pressure P. They considered it to be comparable to the value that would be obtained by applying a pressure difference $2P$ in an experiment conducted under non-equilibrium and steady-state conditions [87]. Vallejos et al.[146] and Yuan et al.[147] followed the same approach. On the other hand, Yuan et al used a non equilibrium molecular dynamics (NEMD) technique referred to as escape time simulations, which consists in simulating two parallel graphene membranes separating a bulk gas reservoir from vacuum[148]. They inferred the permeance of the membrane from the average

time required by a gas molecule to escape from the reservoir. Interestingly, even if the techniques proposed in these various studies are different, they have in common that they disregard the possibility that molecules that have just passed through the membrane may quickly re-cross it. This is due to the fact that the methods used consider that each molecule that crosses the plane of the membrane contributes to the flow, no matter what happens to them after their first passage through the pore. However, these re-crossing events are prone to affect the transport and separation properties of the membrane when it operates out of equilibrium, under differential pressure.

In this chapter, we present results obtained with a simplified molecular model of 2D graphene-like membranes. We compute transport coefficients and we document gas permeation mechanisms by combining the EMD technique and the NEMD technique called DCV-GCMD, introduced in chapter 2. The combination of these two techniques is well suited to the study of 2D membranes. The EMD technique is able to isolate the contribution of the barrier crossing process and DCV-GCMD technique is able to take into account all the mechanisms governing permeation through graphene-like 2D membranes. Comparison of the results obtained by the different methods makes it possible to determine under which conditions (pore size, temperature) the calculated equilibrium permeances differ from those calculated out of equilibrium. We show that the transport coefficient computed by NEMD is lower than that computed by EMD, due to the occurrence of re-crossing events during which gas molecules having just crossed the membrane re-cross it in the opposite direction. The quantitative study of the statistics of re-crossing and desorption times in a region adjacent to the pore, referred to as the pore-mouth region, allows to correct the transport coefficients calculated by the EMD method in good agreement with the results obtained by the NEMD method.

4.1 Fluid and Solid Molecular Models

The system used in this study is shown in Figure 4.1. It consists of three reservoirs of moving spherical fluid molecules [white spheres in Figure 4.1(a)] separated by two porous surfaces made of immobile spherical solid molecules [grey spheres in Figure 4.1(a)]. In our simulations, we applied periodic boundary conditions in all directions so that the two lateral reservoirs are actually connected through their periodic images along the z axis. The central and lateral reservoirs, on the other hand, can only exchange fluid molecules through the two solid porous walls separated by a distance $2L$. The solid walls structure is shown in Figure 4.1(b). It is comparable to the system found in the work of Ford and Glandt[150]. The porous surface is made of two single-layered sheets of spherical molecules with a horizontal slit gap centered around $x = 0$. In each

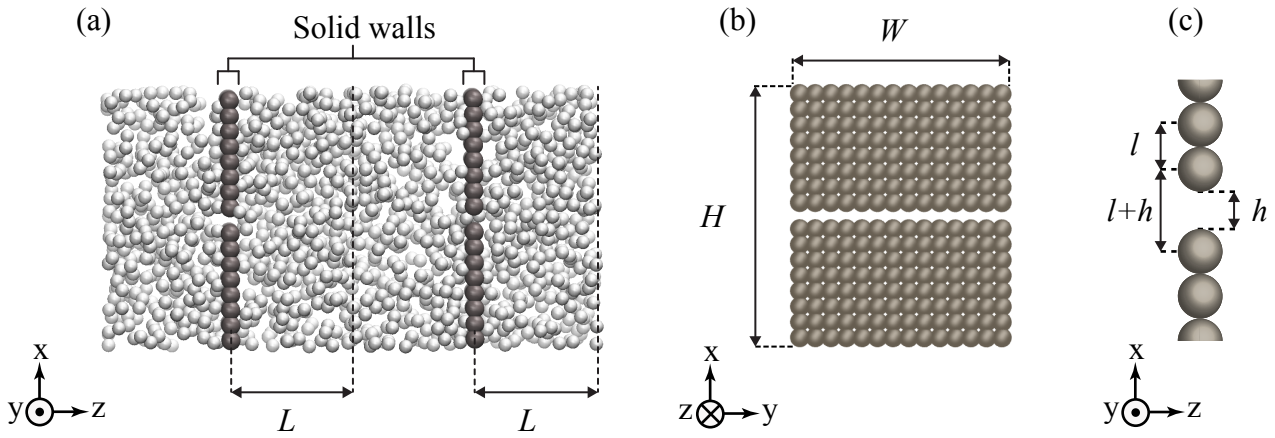

Figure 4.1: Basic features of the system under study. (a) Snapshot of the simulation box in the xz-plane. Periodic boundary conditions are applied in all directions. (b) Snapshot of one solid wall in the xy-plane. (c) Zoomed in view of the slit gap in the xz-plane.

solid walls the molecules are arranged in a square pattern with lattice spacing l. The width h of the slit gap is defined as the vertical distance between the edges of the opposing solid atoms [see Figure 4.1(c)]. The height and width of the solid walls, noted H and W respectively, coincide with the dimensions of the simulation box in the xy-plane.

Fluid and solid molecules are described as simple Lennard-Jones (LJ) spheres with a truncation of the interactions at $r_{ij} = r_c = 2.5\sigma$,

$$\begin{aligned} U_{LJ}(r_{ij}) &= 4\epsilon \left[\left(\frac{\sigma}{r_{ij}} \right)^{12} - \left(\frac{\sigma}{r_{ij}} \right)^{6} \right] \qquad r_{ij} \leq r_c \\ &= 0 \qquad\qquad\qquad\qquad\qquad\quad r_{ij} > r_c \ , \end{aligned} \tag{4.1}$$

where the same potential parameters ϵ and σ were used to describe both fluid/fluid and fluid/solid interactions. In the following of this chapter, our simulations data are expressed in standard LJ reduced units [105] and dimensionless variables are written with an asterisk in superscript (see the appendix for the definition of the reduced units). The lattice spacing was set to $l^* = 2^{1/6}$ and we investigated pore widths ranging from $h^* = 0.55$ to $h^* = 10$. We defined the pore width $h^* = h/\sigma$ in such a way that the two solid sheets form a perfect cristalline surface with lattice spacing l for $h^* = 0$ [see Figure 4.1(c)]. The temperatures imposed in our simulations ranged from $T^* = 1.5$ to $T^* = 4.5$, which are above the critical temperature of the LJ fluid ($T_c^* = 1.1875$ for $r_c^* = 2.5$ [151]). We therefore dealt with supercritical fluids and we observed no phase transition in our systems. Fluid densities ranged from $\rho^* = 0.010$ to $\rho^* = 0.030$, which correspond to dilute

gas conditions. Typically, the porous solid wall was made of two single-layer sheets, each of them consisting of n_x and n_y layers of particles in x- and y-directions respectively. The number of layers in the $y-$direction was set to $n_y = 120$ resulting in a width of the membrane greater than $W^* = 134$. The large dimension of the system in the y-direction helped in maintaining a sufficient number of fluid molecules in the simulation box, even at such low gas densities. Moreover, n_x was adjusted in accordance with the pore size h^*, ranging from $n_x = 6$ for the smallest pore to $n_x = 35$ for the largest pore, so that all systems exhibit a surface porosity $h/H \lesssim 0.12$. This was done to maintain a sufficient resistance to the flow during NEMD simulations, even for the largest pore sizes. The half-distance between the solid walls was set to $L^* = 12$ and held constant for the range of pore widths h^* under investigation.

4.2 Simulation Details

In this chapter, we are primarily interested in the computation of the gas transport coefficient through the single layer membrane. As introduced in chapter 2, in the linear regime, the diffusional transport coefficient, Λ, relates the molecular flux density, j, to the number density difference across the thin membrane, $\Delta\rho$, via the Fick's law:

$$j = \Lambda \Delta\rho \, . \tag{4.2}$$

Given the apparent invariance of our system along the y-axis Λ is independent of the width W of the 2D membrane. However, Λ is inversely proportional to its height H (see Figure 4.1(b)). Consequently most of our data will be reported in terms of ΛH or jH, which are independent of both the height H and width W of the membrane.

As introduced in chapter 2, we employed a method developed recently in our group to compute diffusional transport coefficients from EMD simulations[152]. Λ_{cross} is deduced from the transient concentration profile expressed as

$$C(t) = \frac{1}{2}\left(1 + e^{-t/\tau}\right), \quad \text{with} \quad \Lambda_{cross} = \frac{L}{2\tau} \, . \tag{4.3}$$

For a sufficiently large distance L, permeation events through the two porous walls are uncorrelated and τ is thus simply proportional to L. As a result, Λ_{cross} does not depend on the distance between the interfaces and only accounts for the diffusion of the fluid particles across the solid walls. In our EMD simulations, we used the standard velocity-Verlet integrator using a time step of 0.001 while the solid atoms were held in fixed positions. We first equilibrated the gas phase at the target temperature in the NVT ensemble for 5×10^5 time steps using a Nose-Hoover thermostat with a damping constant of 100 time steps applied to gas molecules only. We then processed

the simulations in the NVE ensemble for 5×10^6 time steps to compute the data required by the post-treatment algorithm discussed above.

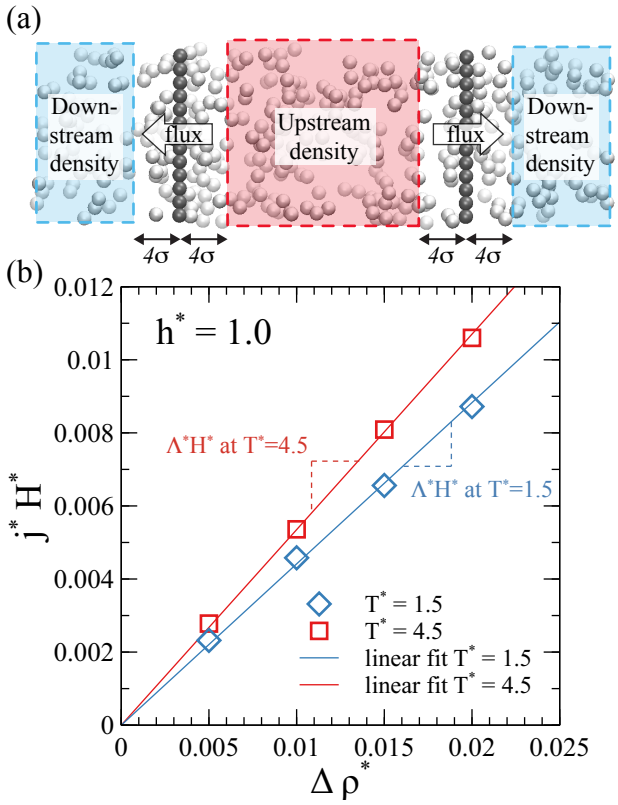

Figure 4.2: (a) Snapshot of the simulation box in the xz-plane showing the principle of the DCV-GCMD technique. (b) Typical evolution of the flux per unit width j^*H^* with the density difference across the membrane $\Delta\rho$. In this example the pore size is $h^* = 1.0$ and we show the results for two temperatures : $T^* = 1.5$ (blue lines and symbols) and $T^* = 4.5$ (red lines and symbols). Solid lines stand for linear fits of the data points and the value of the transport coefficient relates to the slope of the fitting curves.

NEMD simulations stand as the most direct way to compute the transport coefficient described above. As introduced in chapter 2, we used the Dual Control Volume Grand Canonical Molecular Dynamics (DCV-GCMD) scheme to impose a density difference across the membranes[153, 154]. Figure 4.2(a) shows how the simulation box was split in several regions. In addition to the integration of Newton's equations of motion, we performed insertion and deletion of gas molecules in so-called control volumes located in the reservoirs, referred to as *upstream reservoirs* and *downstream reservoirs* regions. We controlled the density in these regions by means of a Grand

Canonical Monte Carlo algorithm to impose a value of the chemical potential in accordance with the target density and temperature. Each time a gas molecule was inserted in the simulation box, the algorithm initialized randomly its velocity based on the Maxwell-Boltzmann distribution at the target temperature. We set the bounds of these control volumes at a distance 4σ away from both side of each membrane to ensure that the Monte Carlo moves did not perturb the dynamics near the porous walls. In our NEMD simulations, we computed the trajectory of the gas molecules with the standard velocity-Verlet integrator using a time step of 0.001 while the solid atoms were held in fixed positions. We first equilibrated the gas phase at the target temperature in the NVT ensemble for 5×10^5 time steps using a Nose-Hoover thermostat with a damping constant of 100 time steps applied to gas molecules only. We then processed the DCV-GCMD runs for 5.5×10^6 time steps. For the computation of the steady-state molecular flux, we discarded the first 0.5×10^6 time steps corresponding to the transient regime. We performed 400 Monte Carlo insertion/deletion trial moves in each reservoir every 20 MD steps to maintain a constant density jump across the membrane. Furthermore, we used the method proposed by Evans and Morriss[155] to control the temperature of the gas phase during out of equilibrium simulation runs. This method consists in subtracting out the local center-of-mass velocity field before computing the temperature of the gas, resulting in a so-called profile-unbiased thermostat. We performed spatial averaging of the velocity field by setting up 2D pencils partitioning the simulation box in 12 bins along the $x-$ axis and 11 bins along the z axis. This resulted in a minimum average number of 10 gas molecules per pencil in our simulations and was sufficient to obtain uniform gas temperatures. Figure 4.2(b) evidences the linear relation between the steady-state fluxes and the imposed density difference, eq. 4.2 was therefore used to obtain the transport coefficient Λ directly from the computed fluxes.

4.3 Results obtained with Simplified Graphene-like System

Before into a detailed comparison of the results obtained with NEMD and EMD techniques, we first investigate the influence of gas density on the transport coefficient. Figure 4.3 shows the evolution of the transport coefficient with the value of the upstream density in the NEMD simulations. We computed this data at fixed downstream density $\rho^* = 0.010$ and we normalized the computed transport coefficients with respect to the mean value $< \Lambda >$ averaged over the range of upstream densities. The results obtained for the investigated range of temperatures and pore sizes do not evidence any influence of the density on the transport coefficient in this range of

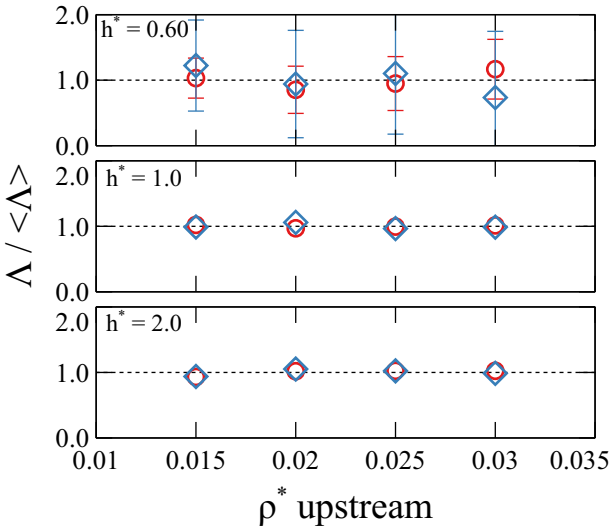

Figure 4.3: Variation of the normalized transport coefficient $\Lambda / < \Lambda >$ with the density of the upstream reservoir at fixed density difference $\Delta\rho^*$. Blue and red symbols stand for data computed at $T^* = 1.5$ and $T^* = 4.5$ respectively. Each subfigure stands for a different pore size : $h^* = 0.60$ (top), $h^* = 1.0$ (middle) and $h^* = 2.0$ (bottom).

gas densities. This suggests that the thermodynamic conditions in our simulations are consistent with the dilute gas limit. In the remaining of this paper we will therefore report only the most accurate data, which correspond to the upstream and downstream densities respectively set to $\rho^* = 0.030$ and $\rho^* = 0.010$ in the NEMD simulations, and a constant density set to $\rho^* = 0.030$ in the EMD simulations.

4.3.1 Comparison with the Theoretical Model for Λ_{cross}

$$U_{pmf}(x,y) = \begin{cases} U_{pot}(x,y,0) + U_{offset} \ , & \text{if } U_{pot}(x,y,0) \neq 0 \\ 0 \ , & \text{otherwise} \end{cases} \tag{4.4}$$

$$\Lambda_{cross} = \frac{1}{4HW}\sqrt{\frac{8kT}{\pi m}} \int\int dxdy \exp\left(\frac{U_{pmf}(x^*,y^*)}{kT}\right) \tag{4.5}$$

As introduced in chapter 3, by using the Lennard-Jones interaction potential and by knowing the positions of the constituent atoms of the membrane, we can then calculate the PMF given by equation 4.4. It is then sufficient to proceed to the numerical integration of equation 4.5 by discretizing the surface of the pore in the (x, y) plane to calculate the transport coefficient Λ_{cross}. Figure 4.4 shows the evolution of Λ_{cross} as a function of temperature for a range of pore sizes, from

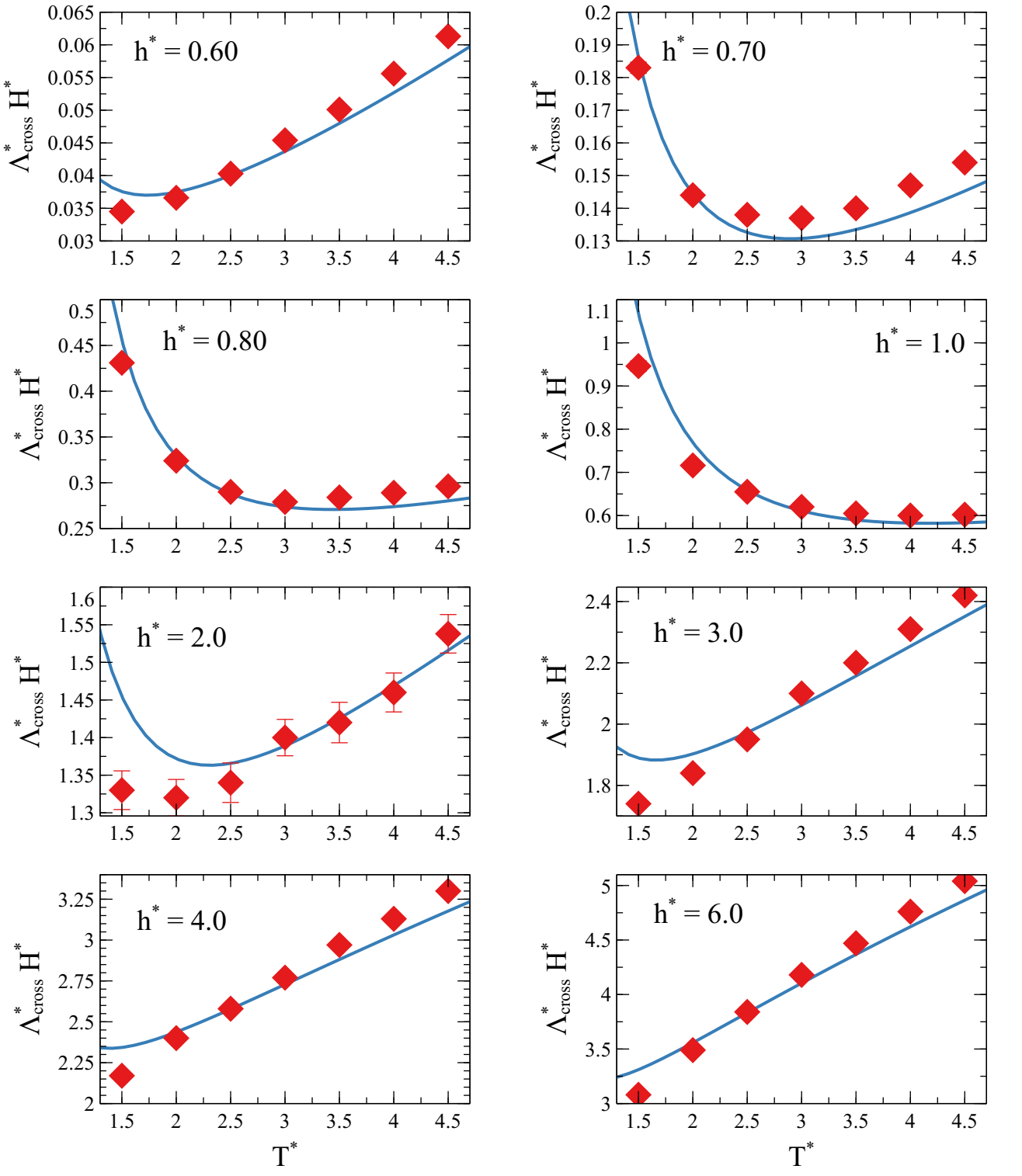

Figure 4.4: Evolution of the transport coefficient Λ_{cross} with temperature for a range of pore sizes. Symbols represent EMD simulations data, while solid lines show model predictions.

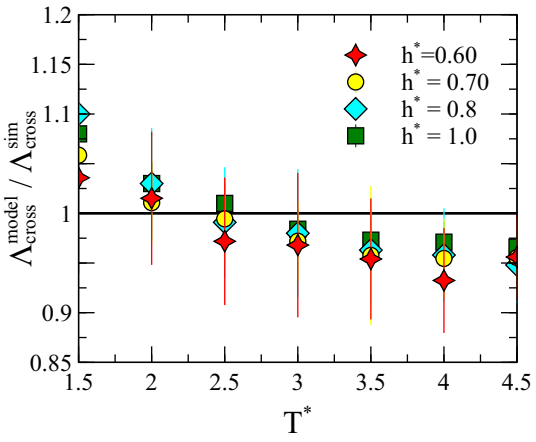

Figure 4.5: Ratio between model prediction and simulation data for Λ_{cross} as a function of temperature and for a range of pore sizes.

the molecular sieving regime ($h = 0.6$) almost to the effusive regime ($h = 6$). Overall, we observe a good agreement between the results of the EMD simulations and the predictions of our theoretical model, without adjustable parameters. Nevertheless, we notice a tendency to overestimate the transport coefficient at low temperature and to overestimate it at high temperature for all pore sizes studied.

As shown in Figure 4.5 these differences are of the order of $\pm 10\%$ maximum. We explain them by our choice to use a rectilinear trajectory orthogonal to the plane of the membrane as the reference trajectory for the calculation of the PMF. Indeed, gas molecules probably deviate from this reference trajectory by taking curvilinear trajectories as they approach the pore, especially at low temperature. This would likely prevent some gas molecules to reach the pore plane resulting in a lower Λ_{cross} value. The fact that the observed deviations depend on the temperature seems to indicate that the trajectories taken by the gas molecules approaching the pore are temperature sensitive. At high temperatures, these interaction effects should be less pronounced. The slight underestimation of simulation data at high temperature could therefore indicate that the molecular dynamics time step should be reduced to observe better agreement. Despite these discrepancies, the theoretical model reproduces the trends of the simulations well and the quantitative agreement remains satisfactory. In particular, we do not need to use independent models to deal with the different permeation regimes and therefore equation 4.5 applies regardless of pore size as long as the flow regime is diffusive.

4.3.2 Comparison between NEMD and EMD data

In the following we report and compare the transport coefficients Λ and Λ_{cross} computed with the NEMD and EMD techniques respectively. Figure 4.6 shows the evolution of both transport coefficients with pore size h in logarithmic scale for temperatures ranging from $T^* = 1.5$ to 4.5. In these plots, solid lines stand for theoretical predictions based on the model proposed by Oulebsir et al [149], which introduced in previous section.

As already demonstrated in the previous section, this model is in excellent agreement with the values of Λ_{cross} obtained from EMD simulations. When the pore size becomes sufficiently large (i.e. for $h^* \gtrsim 2$) one can approximate the accessible porosity by the geometric porosity h/H and neglect the influence of adsorption ($\Gamma \to 1$), which yields the geometric limit represented with a dashed line in Figure 4.6. Having a look at the data obtained for Λ from NEMD simulations, we can immediately notice that the values computed for Λ and Λ_{cross} may differ significantly under certain conditions.

We evidence these discrepancies by plotting the ratio Λ/Λ_{cross} as a function of pore size in Figure 4.7 (a). Strikingly, we see that Λ is systematically lower than Λ_{cross}, indicating that the post-treatment used to compute Λ_{cross} overestimates the number of molecules that contribute to the flow. We observe that this effect is more pronounced for pore sizes around $h^* \simeq 1$ and tends to disappear for smaller and larger pore sizes. Moreover, the influence of temperature is paramount as illustrated by the ratio Λ/Λ_{cross} increasing from 0.46 ± 0.02 at $T^* = 1.5$ to 0.88 ± 0.03 at $T^* = 4.5$ for the pore size $h^* = 1.0$. We attribute these behavior to the adsorption of gas molecules close to the pore mouth where the PMF exhibits a local minimum, as shown in Figure 4.7 (b). The existence of such a free energy minimum has two main effects. Firstly, gas molecules that have just passed through the membrane in a given direction may get adsorbed in this local potential well and spend a certain amount of time there. As a result, if the time required to desorb from this local energy minimum and diffuse away from the pore is not negligible compared to the time it takes to cross the membrane, such gas molecules are likely to re-cross the membrane in the opposite direction. In addition, when the pore size is sufficiently large, this local free energy minimum lies in the plane of the 2D membrane. Consequently, gas molecules may get adsorbed in the pore and oscillate around this equilibrium position thus crossing and re-crossing the membrane multiple times over short periods of time. These two mechanisms are enhanced for pore sizes close to $h^* = 1.0$. Under such conditions, the minimum of PMF is located in the plane of the pore, leading to quick oscillations of the adsorbed molecules back and forth through the membrane. Moreover at such pore sizes, the PMF well is deep enough to slow down the diffusion of gas molecules to the bulk of the reservoir considerably. The post-treatment algorithm used

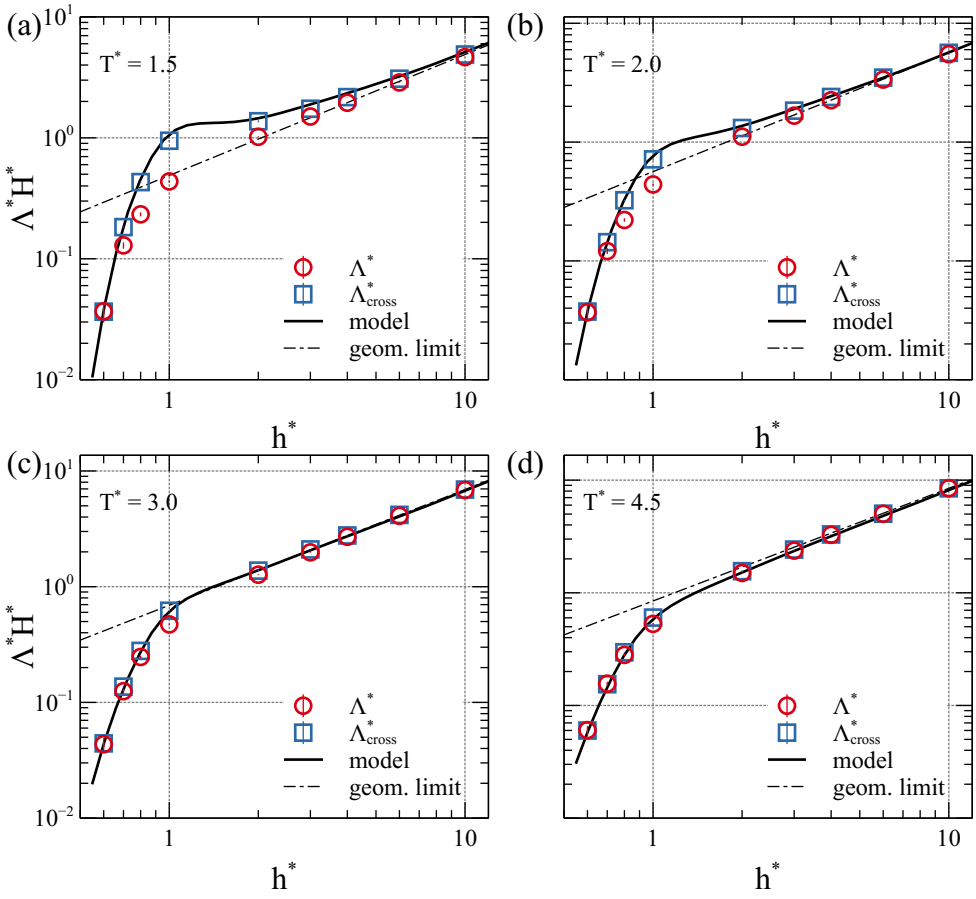

Figure 4.6: Evolution of the transport coefficient with pore size in logarithmic scale at different temperatures : (a) $T^* = 1.5$, (b) $T^* = 2.0$, (c) $T^* = 3.0$ and (d) $T^* = 4.5$. Red circles stand for $\Lambda^* H^*$ computed from NEMD simulations, blue squares stand for $\Lambda^*_{cross} H^*$ computed from EMD simulations. Solid lines show the predictions of the theoretical model from Oulebsir et al. [149] and the dashed lines stand for the geometrical approximation $\Lambda H = \bar{v}h/4$.

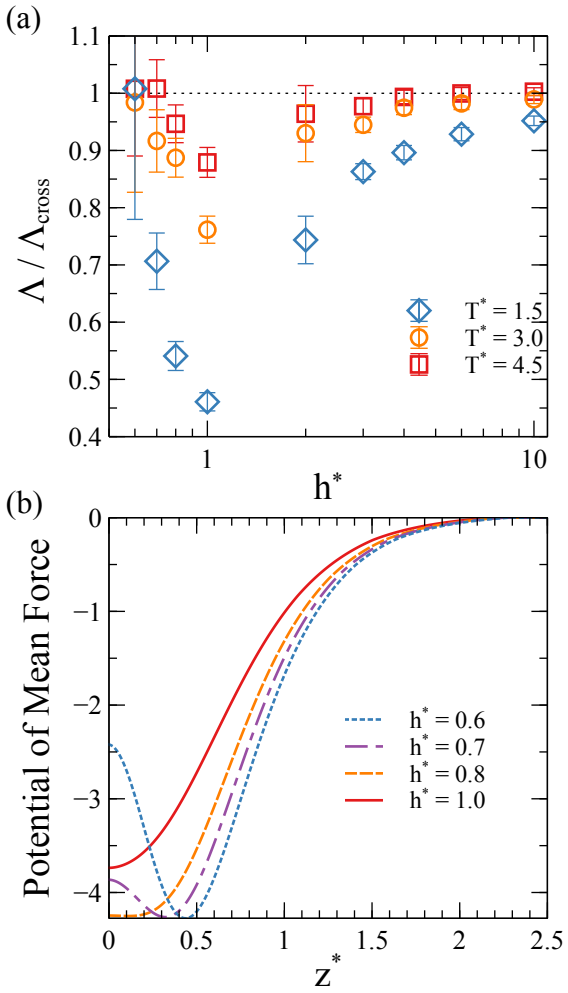

Figure 4.7: (a) Ratio of the transport coefficients Λ/Λ_{cross} as a function of pore size h^* in semi-log scale. Blue lozenges, orange circles and red squares stand for data computed at temperatures $T^* = 1.5$, $T^* = 3.0$ and $T^* = 4.5$ respectively. (b) Potential of mean force of a single gas molecule along the trajectory $(0, 0, z)$ corresponding to the most favorable path through the membrane. Blue dotted line, purple dashed-dotted line, orange dashed line and red solid line stand for the pore sizes $h^* = 0.6$, 0.7, 0.8 and 1.0 respectively.

to compute transport coefficient from EMD simulations is "blind" to such mechanisms and each crossing of the barrier is accounted for in the computation of Λ_{cross}, leading to $\Lambda/\Lambda_{cross} \leq 1$. For smaller pore sizes, the probability of re-crossing must tend to zero as the energy barrier between the minimum of PMF and the center of the pore increases rapidly. This explains why the ratio of transport coefficients gradually approaches unity when the pore size decreases. On the other hand, when the pore size is several times larger than the diameter of the gas molecules, the effects of adsorption described above only concern a minority of molecules crossing the membrane at the edges of the pore. Therefore the ratio of transport coefficients tends to unity as the pore size increases.

4.3.3 Probability of desorption

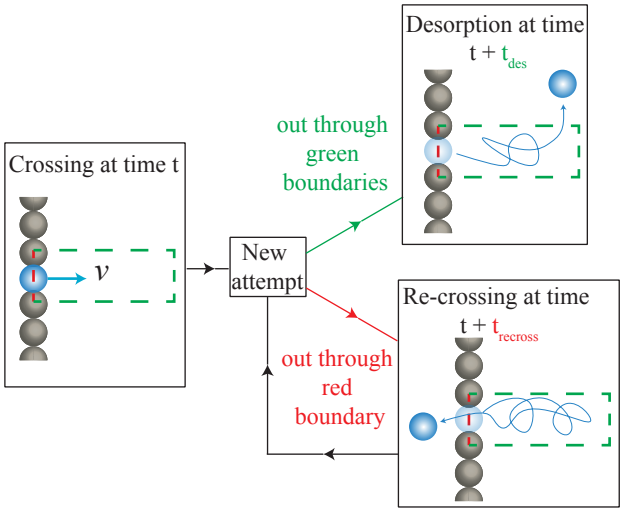

Figure 4.8: Principle of the post-treatment procedure applied to EMD simulations to compute the first passage times statistics.

To document the phenomena leading to $\Lambda/\Lambda_{cross} \leq 1$, we investigated first passage times distributions of gas molecules diffusing in a so-called *pore mouth region* adjacent to the 2D membrane. Figure 4.8 shows the principle of the post-treatment we applied to the molecular trajectories obtained from EMD simulations to compute first passage times statistics. The pore mouth region is a rectangular cuboid, one edge of which is the same length as the simulation box along the y-axis (see coordinate system in Figure 4.1) and is therefore periodic in this direction. In the xz-plane, one boundary of the region coincides with the position of the pore and appears as a red dashed line in Figure 4.8, while the other boundaries are located at finite distances from the pore and

appear as green dashed lines (further details in the next paragraph). Our post-treatment detects any gas molecule that crosses the membrane and enters the region through the red boundary at times t with a velocity pointing inward. Each of these crossing events triggers a new *attempt* with two possible outcomes: if a gas molecule goes out the region through the green boundary, this will be considered as a *desorption* event occurring at time $t + t_{des}$; if the gas molecule goes out the region through the red boundary, this will be considered as a *re-crossing* event occurring at time $t + t_{recross}$. As simulation time progresses, we keep track of the number of desorption and re-crossing events as well as the statistics of times t_{des} and $t_{recross}$.

Obviously, the probability distributions of times t_{des} and $t_{recross}$ depend directly on the definition of the pore mouth region. The latter should delimit the zone of influence of the pore in terms of adsorption. Figure 4.9 (a) shows a 2D map of the Boltzmann factor $exp(-U(x,z)/kT)$ where $U(x,z)$ stand as the potential energy of one gas molecule averaged over a transverse distance $l^* = 2^{1/6}$, corresponding to the periodicity of the pore structure in the y-direction. In this example, the pore size is $h^* = 1.0$ and the temperature is $T^* = 1.5$. The middle of the pore is located at $(x^*, z^*) = (0, 0)$ and in this example it coincides with the minimum of the PMF in the pore mouth region. We see that the Boltzmann factor tends to unity away from the plane $z^* = 0$ as the interactions between membrane atoms and the gas molecule vanish. Dashed black lines indicate how we set the boundaries of the pore mouth region. Along the x-axis, the boundaries are located at $x^* = \pm(h^* + l^*)/2$ beyond which gas molecules fall in the zone of influence of neighboring adsorption sites on the surface of the membrane. As for the upper bound of the region along the z-axis, results reported in Figure 4.9 (b) show that the number of attempts resulting in re-crossing of the membrane hits a plateau when z^*_{max} becomes greater than 1.5. This value indeed corresponds to the position of the interface between the bulk of the reservoir and the adsorbed layer at the surface of the membrane. Consequently, we set $z^*_{max} = r^*_c = 2.5$ as the upper bound of the pore mouth region to make sure we obtain a converged number of re-crossing events.

From the numbers of re-crossing and desorption events, we computed the probability densities $p_{recross}(t)$ and $p_{des}(t)$ of respectively re-crossing the membrane and desorbing from the pore mouth between times t and $t + dt$. Figure 4.10 reports the results obtained for pore sizes ranging from $h^* = 0.6$ to $h^* = 1$, at a temperature $T^* = 1.5$. We observe that the probability density of desorption events , p_{des}, exhibits a single peak shifting towards smaller times as the pore size decreases. The evolution of the PMF landscape with pore size explains this shift. Indeed, as pore size gets smaller the distance and the energy barrier between the local PMF minimum in the pore mouth region and neighboring adsorption sites located at the surface of the membrane tend to decrease, resulting in desorption events occurring sooner. Moreover, we observe that a

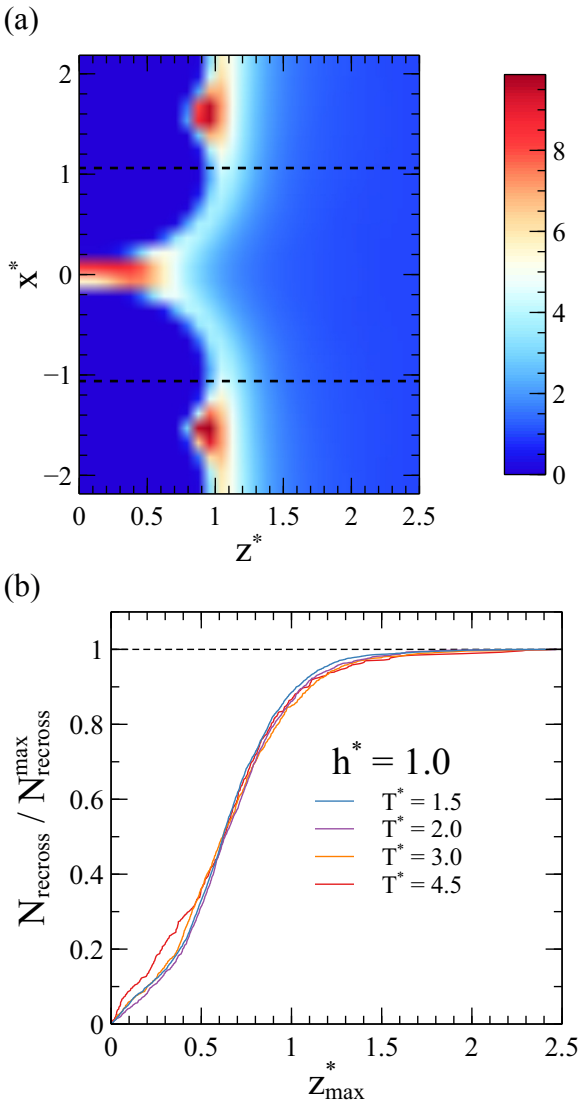

Figure 4.9: (*a*) 2D map of boltzmann factor $exp(-U^*(x,z)/T^*)$ around the pore mouth region. The pore size is $h^* = 1.0$ and the temperature is $T^* = 1.5$. Dashed black lines show the limits of the pore mouth region in the x direction, as set in our post-treatment algorithm. (*b*) Cumulative number of gas molecules re-crossing the membrane as a function of their maximum z displacement in the pore mouth region. The pore size is $h^* = 1.0$ and we show data temperatures ranging from $T^* = 1.5$ to 4.5.

decrease of the pore size also leads to higher desorption probabilities, in response to the increase of the energy barrier that a gas molecule has to overcome in order to re-cross the membrane. On the other hand, the shape of the probability density $p_{recross}$ reported in Figure 4.10 is more

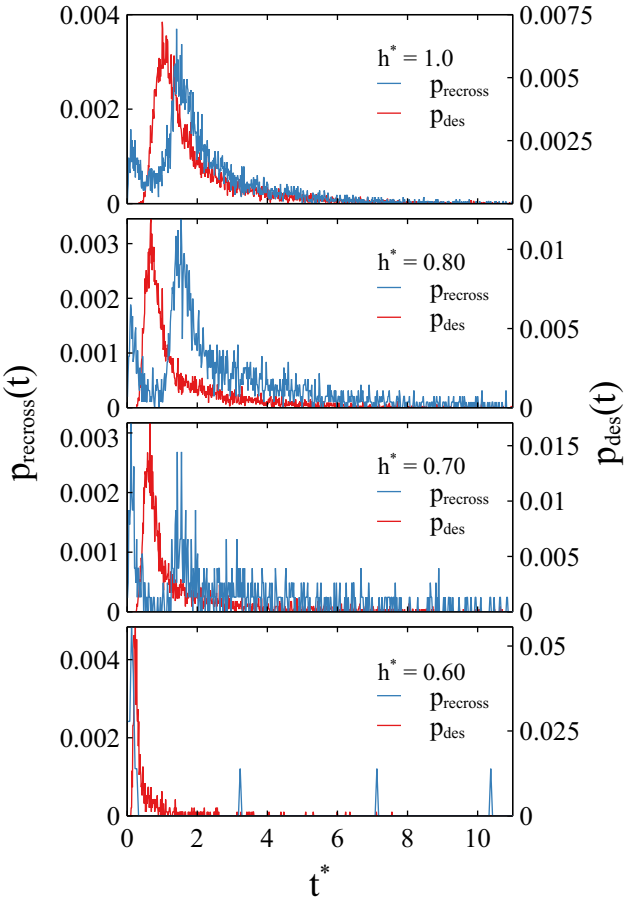

Figure 4.10: First passage time statistics for a range of pore sizes. We plot re-crossing time ($p_{recross}$, blue lines) and desorbing time (p_{des}, red lines) probability densities. All data was computed at $T^* = 1.5$, we present results obtained for pore sizes $h^* = 1.0$, 0.8, 0.7 and 0.6.

complex. A first main peak appears at small times that may be followed by a second main peak at larger times for larger pore sizes (i.e. $h^* \geq 0.7$). When the energy barrier required to cross the pore becomes sufficiently low, rapid oscillations of molecules adsorbed near the middle of the pore result in frequent crossings of the membrane. This explains the presence of the first peak for larger pore size. We observe, however, a similar peak for small pore sizes in spite of the higher energy barrier, which suggests that this first peak also underlies rare events such as gas molecules interacting through the barrier and thus influencing the shape of the PMF occasionally. In the case of the pore size $h^* = 0.6$, we stress that the number of re-crossing events comprised in the first peak of $p_{recross}$ amounts to 13 events detected over 5×10^6 time steps and such effects are therefore marginal. The second peak of $p_{recross}$ stands for gas molecules that diffuses inside the pore mouth region before re-crossing the membrane. We observe that the second peak of $p_{recross}$ is

concurrent with the main peak of p_{des} for pore sizes $h^* \geq 0.7$. In addition, we see that this second peak decreases in amplitude and spreads to larger times when the pore size decreases. There again, the increase of the energy barrier required to cross the pore explains why the probability of re-crossing the membrane decreases when the pore size is reduced. For the smallest pore size $h^* = 0.6$, the second peak vanishes and gives way to rare re-crossing events distributed over time randomly.

4.3.4 Correction of Λ_{cross} by the Probability of Desorption

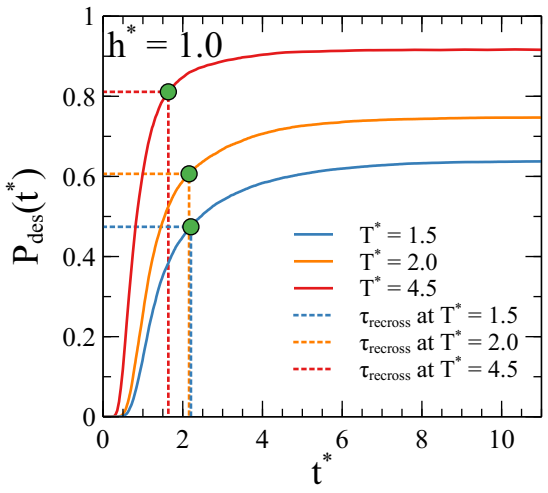

Figure 4.11: Cumulative distribution functions (CDF) P_{des} of desorbing time (solid lines) for three values of temperature : $T^* = 1.5$, 2.0 and 4.5. Green circles and dotted lines indicate the values of the CDF at $t = \tau_{recross}$ for each temperature.

Of the molecules that have passed through the membrane, only those that desorb from the pore-mouth region contribute to the flow. The transport coefficient Λ_{cross} computed from EMD simulations does not account for this additional desorption mechanism, which explains why Λ_{cross} is systematically greater than the true transport coefficient Λ computed from NEMD simulations. It thus makes sense to correct Λ_{cross} by the probability of desorbing from the pore mouth region. To do so, we compute the Cumulative Distribution Function (CDF) of the probability density $p_{des}(t)$ defined as

$$P_{des}(t) = \int_0^t p_{des}(u)du \ . \tag{4.6}$$

Figure 4.11 shows the typical shape of $P_{des}(t)$ obtained for $h^* = 1.0$, which is the pore size that reveals the lower Λ/Λ_{cross} values in our study. We see that $P_{des}(t)$ is a S-shaped curve that reaches

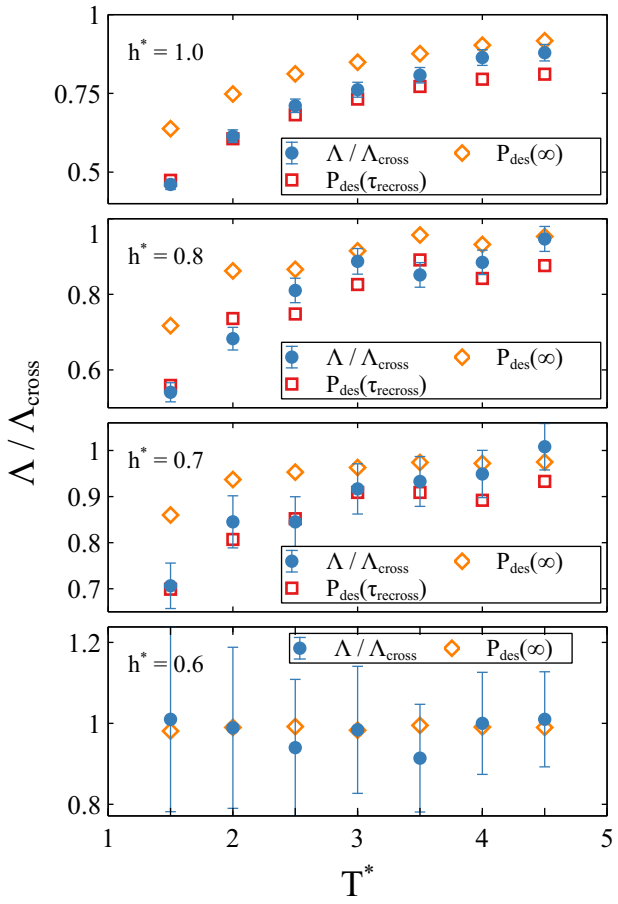

Figure 4.12: Evolution of the ratio of transport coefficients Λ/Λ_{cross} with temperature, for a range of pore sizes $h^* = 1.0$, 0.8, 0.7 and 0.6. Blue plain circles stand for simulation data, red hollow squares stand for the value of $P_{des}(\tau_{recross})$ and orange hollow losanges stand for the asymptotic value of P_{des} at large time.

a plateau at large times. We refer to the asymptotic value of P_{des} at large times as $P_{des}(\infty)$. This corresponds to the probability that a gas molecule that has just crossed the membrane leaves the pore mouth region without re-crossing the barrier, whatever time it takes. In other words, $P_{des}(\infty)$ is the ratio of the total number of desorption events to the total number of events. For instance, we observe on the figure that $P_{des}(\infty)$ increases from approximatively 0.64 to 0.92 between $T^* = 1.5$ and $T^* = 4.5$ for the pore size $h^* = 1.0$. In Figure 4.12 we compare the values of Λ/Λ_{cross} (plain blue circles) to that of $P_{des}(\infty)$ (orange hollow lozenges) obtained for a range of temperatures and pore sizes. While these two quantities exhibit similar increasing trends with temperature, $P_{des}(\infty)$ is globally higher than Λ/Λ_{cross}. More precisely, the discrepancies are the highest at lower temperatures and they progressively decrease as the temperature rises. For the

smallest pore size $h^* = 0.6$, however, we find a good agreement between these two quantities over the whole temperature range, with values close to one.

In previous paragraphs we noticed the concurrency of the main peak of $p_{des}(t)$ and the second peak of $p_{recross}(t)$ observed for pore sizes $h^* \geq 0.7$ (cf. Figure 4.10). This suggests a competition between the re-crossing and desorption mechanisms. We infer the average re-crossing time $\tau_{recross}$ from the probability density $p_{recross}(t)$ as

$$\tau_{recross} = \int_0^\infty p_{recross}(u) u du \ . \tag{4.7}$$

Then the CDF $P_{des}(t)$ evaluated at $t = \tau_{recross}$ yields the probability that a molecule will leave the pore mouth region between $t = 0$ and $t = \tau_{recross}$. In other words, $P_{des}(\tau_{recross})$ corresponds to the probability that a gas molecule desorbs from the pore mouth before the characteristic time required to re-cross the membrane. The green dots in Figure 4.11 exemplifies how we compute $P_{des}(\tau_{recross})$ from the CDF and more substantiated data are reported in Figure 4.12 as red hollow squares. We observe a fair agreement between Λ/Λ_{cross} and $P_{des}(\tau_{recross})$ for pore sizes $h^* \geq 0.7$, especially at lower temperatures. Note that values of $P_{des}(\tau_{recross})$ obtained for $h^* = 0.6$ are not reported in Figure 4.12. We indeed could not compute converged values of $\tau_{recross}$ for $h^* = 0.6$ as re-crossing events are rare. However, the good agreement between Λ/Λ_{cross} and $P_{des}(\infty)$ suggests that $\tau_{recross}$ should be considered as sufficient long for P_{des} to reach its plateau value when the crossing of the free energy barrier in the plane of the membrane dominates the permeation process.

Based on the discussions above, we validated the theoretical formula $\Lambda = P_{des}\Lambda_{cross}$ to describe the transport coefficient of gas through single layer graphene-like membrane. In next chapters, we will apply this theoretical model to realistic graphene-gas systems.

4.4 Conclusion

.

In this chapter, we have shown that the combined use of equilibrium and non-equilibrium molecular dynamics methods allowed us to identify the mechanisms governing gas diffusion through 2D graphene-like membranes. Permeation appears as a two-step process: in the first step, a gas molecule contained in the inlet reservoir crosses the 2D membrane's plane; in the second step, this molecule must escape from the pore's zone of influence, referred to as the pore-mouth region, to mix with the other gas molecules that populate the outlet reservoir. If the second step does not succeed, the gas molecule re-crosses the membrane and returns to the inlet reservoir, cancelling its contribution to the flow. Previous studies found in the literature only address the first step, as they use numerical methods that make such re-crossing events

impossible[148], or they consider that a molecule making a rapid round trip across the membrane nevertheless contributes to the molecular flow[87, 149, 146, 147]. The DVC-GCMD method used in our work allows us to isolate the contribution of the second step of the permeation process by comparing its results with those of EMD simulations. Indeed, we were able to demonstrate that the transport coefficient of the membrane under pressure gradient was systematically lower than the transport coefficient calculated at equilibrium conditions, as a result of the re-crossing events described above. This tendency is very marked when the pore size is comparable to that of the gas molecule, i.e. in the crossover between the molecular sieving regime (small pore size) and the effusion regime (large pore size). By analyzing the statistics of re-crossing and desorption times inside the pore-mouth region, we were able to quantify the probability that a gas molecule that has passed through the membrane succeeds in leaving this region on the side of the inlet reservoir. This probability is in agreement with the multiplicative prefactor required to match the value of the transport coefficient obtained from EMD simulations with the one obtained from NEMD simulations. This motivates the introduction of our theoretical model to account for the influence of barrier crossing and desorption on the permeation process. These results suggest that a finer analysis of the 3D potential of mean force around the pore is needed to predict this corrective prefactor and thus improve existing theoretical models. Unfortunately, we did not have enough time to develop a theoretical model for P_{des}, and this problem will be addressed in future work. Nevertheless, we will use the theoretical framework $\Lambda = P_{des}\Lambda_{cross}$ to interpret the results of the simulations performed on realistic graphene-gas systems. More specially, in the molecular sieving regime and effusion regime, as $P_{des} \approx 1$, the model for Λ_{cross} will be sufficient to predict permeation and selectivity.

Chapter 5

Gas Permeation through Single-layer Nanoporous Graphene

Contents

In the previous chapter, we proposed a theoretical model based on a simplified system. We performed equilibrium molecular dynamics (EMD) and non equilibrium molecular dynamics (NEMD) simulations with pure supercritical fluids permeating through single-layer nanoporous solids, where both fluids and solids consisted of spherical Lennard-Jones (LJ) molecules with a slit gap of controllable width on the membrane. From the simulations results, we verified that molecular diffusion was the only permeation mechanism, as reported in literature[83, 87, 156, 127, 44]. Meanwhile, our theoretical model is not in the form of semi-empirical Arrhenius-type equations[127, 44] and we observed that simulated transport coefficients were in good agreement with the predictions of our theoretical model. We demonstrated that our theoretical approach was suitable for

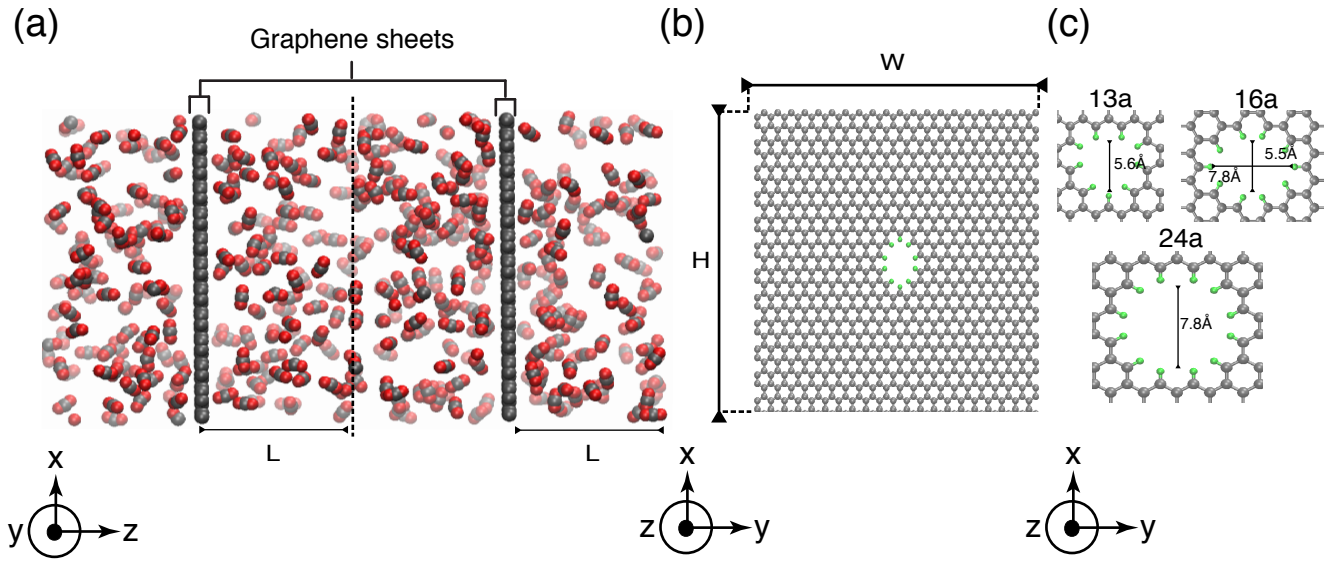

Figure 5.1: Basic features of the system under study. (a) Snapshot of the simulation box in the xz-plane. Periodic boundary conditions are applied in all directions. (b) Snapshot of one graphene sheet in the xy-plane. (c) Zoomed in view of the graphene pores in the xy-plane.

all scales of pore sizes, ranging from the molecular sieving regime to the effusion regime. As shown in this chapter, this theoretical model should also be applicable to single layer nanoporous graphene membranes.

In this chapter, we show how to extend and apply our theoretical model to realistic graphene-gas system. We applied the same EMD and NEMD techniques and performed our simulations with different gas species, including CH_4, CO_2, N_2 and O_2 through porous graphenes exhibiting different pore sizes and geometries. Hydrogen-terminated sub-nanometer pores are generated in the center of a graphene sheet. We report the values of transport coefficient with different gas-pore combinations to confirm the adaptation of this theory to temperatures and gas densities.

5.1 Gas and Nanoporous Graphene Molecular Models

The system used in this chapter is shown in Figure 5.1. Two immobile porous graphene sheets, which were frozen by zeroing the force acting on them in the simulations, were placed parallel to each other in z direction at a distance of $2L$, separating the simulation box into three reservoirs. Each graphene sheet contains a hydrogen-terminated pore in its center. A pore library was designed by Yuan et al[44]. In this study, we chose three typical pores: 13a, 16a and 24a, representing small, intermediate and large sizes. In our simulations, we applied periodic boundary

conditions in all directions so that the two lateral reservoirs are actually connected through their periodic images along the z-axis. It is worth noting that the box dimensions in the xy-plane, as well as the height H and width W of the graphene sheet, need to be modified to make a periodic boundary. To ensure that the central and lateral reservoirs can only exchange gas molecules through hydrogen-terminated pores, we must extend by a distance of C-C equilibrium bond length along y-axis and a distance of $\sqrt{3}/2$ times C-C bond length along x-axis. To generate the nanoporous graphene membranes, we used the software Visual Molecular Dynamics (VMD[157]). More details about the process of generating nanoporous graphene membranes can be found in appendix.

In this study, an all-atom force field was used to carry out the simulations. The total potential energy of this force field is described in a standard way[158, 159, 160, 161, 162], as a sum of bonded pairwise interactions and non-bonded pairwise interactions. The bonded interactions include harmonic bond stretching, harmonic angle bending and dihedral potentials in a cosine form. A pair of atoms is considered as non-bonded if they belong to different molecules or if they are on the same molecule but separated by more than two covalent bonds. The case when two atoms are in the same structure and separated by three covalent bonds, so called 1-4 interaction, is treated with scaled LJ and Coulombic potentials with scaling factor of 0.5. All 1-2 (directly bonded atoms) and 1-3 (two atoms separated by two bonds) non-bonded interactions are ignored, since they are included in the bonded part through bond stretching and angle bending.

In graphene-gas system, the most important part of the force field is the non-bonded interaction, which is given as a sum of steric and dispersive Van-der-Waals interaction modeled by Lennard-Jones 12-6 potential and electrostatic interactions.

$$U_{nb}(r_{ij}) = 4\epsilon \left[\left(\frac{\sigma}{r_{ij}} \right)^{12} - \left(\frac{\sigma}{r_{ij}} \right)^{6} \right] + \frac{q_i q_j}{4\pi\epsilon_0 r_{ij}} \tag{5.1}$$

where the summation is over all the active sites of the molecules for which the potential is being calculated. ϵ and σ are the energy and size parameters, while q is the charge on site an r the distance between the active sites. For cross term pairwise Lennard-Jones interactions, Lorentz-Berthelot combination rules are used:

$$\epsilon_{ij} = \sqrt{\epsilon_i \epsilon_j} \quad \sigma_{ij} = \frac{\sigma_i + \sigma_j}{2} \tag{5.2}$$

All the bonded and non-bonded interaction parameters of graphene were given by the all-atom-optimized potentials for liquid simulations (OPLS-AA model)[163]. The transferable potential for phase equilibria (TraPPE)[164] force field and the OPLS-AA force field were used for CO_2 and CH_4, respectively. For CO_2, original TraPPE force field has fixed bond lengths and angles

of molecules. We modified this force field to allow these degrees of freedom to vary so that the CO_2 model used was all-atom and fully flexible[165, 166]. For O_2 and N_2, they were modeled by using both a united atom (UA) Lennard-Jones potential as well as with a diatomic Lennard-Jones potential proposed by Krishnamurthy et al[167]. The cutoff distance of the Lennard-Jones interaction was set as 1.2 nm. Long range electrostatics were handled using the Particle-Particle-Particle Mesh (PPPM) method.

To deal with supercritical fluids without phase transition in our simulations, the imposed temperatures ranged from $T = 300K$ to $T = 700K$. A remarkable point is that $T = 300K$ is below the critical temperature of CO_2 (304 K). In this condition, different behavior was observed in our simulations and we will discuss this behavior in the next section. Note that in practical experiments used to test gas permeation through single layer or few-layer graphene, the pressure of gas is lower than 10 bar[73, 168, 72, 86, 169, 170, 128, 171]. We define a dilute system with gas densities ranging from $\rho = 0.3mol/L$ to $\rho = 2mol/L$ while the pressure ranged from 5 bar to 50 bar. The graphene sheet was set to a square with $H = W = 5nm$, while the half-distance between graphene sheets was set to $L = 5.5nm$. The size of graphene sheets and the distance L were held constant for the different pore sizes under investigations.

5.2 Simulations Details

All molecular dynamics simulations were carried out using LAMMPS[99] (http:// lammps.sandia.gov), which we extended for our own requirements. In this chapter, we used both EMD simulations and NEMD simulations as mentioned. For the EMD simulations, we distributed the same number of gas molecules in the central reservoir and lateral reservoir. To do so, we used Packmol[172] software to create initial gas systems with random positions where gas molecules did not overlap with graphene sheets. The file generated by Packmol was in format of .xyz and we used Moltempate[173] to convert .xyz files to LAMMPS input/data files. Starting with the initial system discussed above, the trajectory of the gas molecules were computed with the standard velocity-Verlet integrator using a time step of 1 fs. To equilibrate the gas phase at target temperature, we first simulated in the NVT ensemble for 5×10^5 time steps using a Nose-Hoover thermostat with a damping constant of 100 time steps applied to gas molecules only. Then we processed the simulations in NVT ensemble for at least 4×10^6 time steps to compute the transport coefficient. With the small pore sizes, we had to increase the duration of this NVT run depending on the value of transport coefficient. For instance, for the Pore-13a, we had to run NVT simulations for 8×10^7 time steps as a result of the small value of the transport coefficient.

For EMD simulations, with the same method as mentioned in chapter 4, transport coefficient

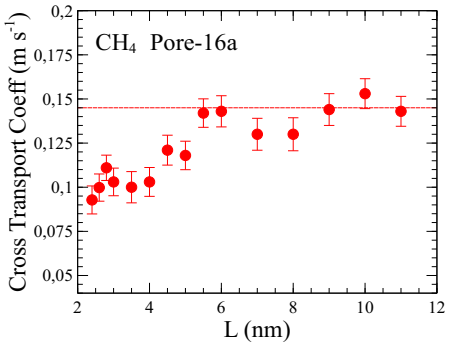

Figure 5.2: Evolution of Λ_{cross} with half distance L between two graphene sheets for CH_4 with Pore-16a at 300 K.

was computed as the ratio of the half-distance of graphene sheets, L, to the characteristic time, τ, of gas concentration fluctuations between the reservoirs at equilibrium. The post-treatment algorithm introduced in chapter 2 allowed us to isolate the contribution of crossing events. Thus, the transport coefficient computed from EMD simulations is noted as Λ_{cross}.

Figure 5.2 shows how the cross transport coefficient increases and reach a plateau as the half distance between two graphene sheets increases. We find that the cross transport coefficient reach a constant when $L_{min} = 5.5nm$. With this distance, the permeation events through the two graphene sheets are uncorrelated. As a result, Λ_{cross} does not depend on the distance between the graphene sheets and only accounts for the diffusion of the gas molecules across the membrane. In our work, we chose this distance for our system to save the computational cost.

In NEMD simulations, we used the technique of dual control volume grand canonical molecular dynamics (DCV-GCMD) as mentioned in chapter 2 and 4. With this technique, a flow is generated by connecting the nanoporous graphene under study to two reservoirs of gas at different densities. The central reservoir and lateral reservoir are considered as the upstream and downstream reservoirs, respectively. The densities in these reservoirs are controlled by means of grand canonical Monte Carlo (GCMC) implemented in LAMMPS and molecular motions are described using molecular dynamics simulations. The GCMC technique was applied in the region away from the graphene sheet. For a system out of equilibrium, we computed the molar flux instead by counting the velocity of molecules in a region comprised between two cross sections of the simulation box. The flux is defined as:

$$j = \frac{\sum v}{2SlN_A} \tag{5.3}$$

where S and l are the surface of simulation box and a small distance between two cross sections, respectively. In our system $l = 0.5nm$, and the factor $1/2$ means that we used one region on each side of the membrane to compute the flux. N_A is Avogadro's number. $\sum v$ is the sum of velocities of the gas molecules in regions described above. In NEMD simulations, we first equilibrated the gas phase at the target temperature in the NVT ensemble for 5×10^5 time steps using a Nose-Hoover thermostat with a damping constant of 100 time steps. We then processed to the DCV-GCMD runs for 5×10^5 time steps to assign different densities in two reservoirs. We maintained the different densities across the membrane in the production of data. We performed 20000 Monte Carlo insertion/deletion trial moves in each reservoir every 1000 MD steps and ran at least 4×10^6 time steps to compute the flux. Other general parameters of NEMD simulations are the same as EMD simulations.

In the graphene-gas system, several studies[144, 146, 82, 174, 175] have shown that gas molecules need to overcome free energy barriers to pass through the pore in the molecular sieving regime. To compute free energy profiles, or so-called potentials of mean force (PMF)[176, 177] in our work, biased MD techniques are required. In this work, we employed the adaptive biasing force (ABF) method[124, 125] as mentioned in chapter 2, implemented in LAMMPS/colvars package[126]. In ABF simulations, we defined the reaction coordinate as the distance between the center of a pore and a selected gas molecule. To compute the 1D profile of PMF, the motion of the gas molecule was restrained to a line perpendicular to the xy plane of graphene sheet, while it was restrained on the surface of xy plane of graphene sheet to compute the 2D profile of PMF. To perform biased MD simulations, we first equilibrated the system by means of regular MD in NVT ensemble for 7×10^5 time steps with a Nose-Hoover thermostat and a damping constant of 100 time steps. During the last 2×10^5 time steps of the NVT equilibration procedure, we dragged the selected gas molecule toward the center of the pore by applying a constant external force of amplitude 2000 in unit of $Kcal\ mol^{-1}$ Å^{-1}. Note that a constant external force with the same amplitude for the molecule of CH_4 can cause the problem of losing atom because the H atom is much lighter than the C atom. With the same amplitude of force, H atoms displace faster than C atom. To avoid this problem, we applied an external force of amplitude 200 for H atoms while the amplitude for C atoms was still 2000. We then processed to ABF simulation for 4×10^7 time steps with a Nose-Hoover thermostat set as previously described. The motion of the selected molecules was restrained to the reaction coordinate axis by means of a harmonic potential with an energy constant of 9000 in unit of $Kcal\ mol^{-1}$. The biasing external force field was accumulated in bins of width 0.1 Å distributed along the reaction coordinate.

5.3 Results obtained for United-Atom Gas Models

To analyzing gas diffusion process in graphene-gas systems, at first, we start with spherical gas molecules, $O_2 - UA$ and $N_2 - UA$. This system is similar to the simplified system of chapter 4. We apply directly the theoretical model for this system:

$$\Lambda = P_{des}\Lambda_{cross} \tag{5.4}$$

For graphene-gas systems, previous studies considered the pre-factor as a constant and assumed that the pre-factor approaches 1. It is correct when the pore size is small enough and the gas permeation is in the molecular regime. Nevertheless, in chapter 4, we have proved that the desorption effect can not be neglected in the crossover regime when the pore size is intermediate, especially at low temperature. So the probability of desorption could be obviously less than 1 even with sub-nanometer pore sizes.

In Figure 5.3, we show the simulated transport coefficients ,Λ_{cross} and Λ, for several gas-pore combinations. When it comes to the Pore-24a, we note that the discrepancies between Λ_{cross} and Λ are significant. The difference is more obvious at low temperature, similar to what we observed with simplified systems. It means that the desorption effect can not be neglected in such conditions and applying a constant pre-factor, $P_{des} = 1$, may lead to significant inaccuracies. When it comes to Pore-13a and Pore-16a, the barrier crossing process can be considered as rate-limiting process, as Λ/Λ_{cross} for $O_2 - UA$ and $N_2 - UA$ is approaching a value of 1. Because of $P_{des} \approx 1$, we observed that $\Lambda^a/\Lambda^b \approx \Lambda^a_{cross}/\Lambda^b_{cross}$ for Pore-13a and Pore-16a. It indicates that we can use our theoretical model for Λ_{cross} to predict the selectivity. For Pore-24a, even if Λ^a/Λ^b and $\Lambda^a_{cross}/\Lambda^b_{cross}$ have the same order of magnitude, Λ^a/Λ^b is not equal to $\Lambda^a_{cross}/\Lambda^b_{cross}$, especially at low temperature. Nevertheless, the selectivity of $O_2/N_2 - UA$ with Pore-24a is so weak that an accurate prediction of selectivity is not important under such conditions. Meanwhile, our simulated results for Λ^a/Λ^b decreases with pore size increasing. This exemplifies a trade-off between permeability and selectivity, which is widely observed in the permselective membrane literature[46, 178, 45].

As for the investigated pore sizes, it can be observed that the permeation of $O_2 - UA$ and $N_2 - UA$ with Pore-13a and Pore-16a is in the molecular sieving regime, while the permeation of $O_2 - UA$ and $N_2 - UA$ with Pore-24a is in the crossover regime. To verify that our theoretical approach based on molecular diffusion mechanism can be applied to all pore sizes, we designed a large pore with a diameter of 2nm to check if other mechanism boosting the frequency of permeation events, as shown in Figure 5.4.

With this pore size, we compare Λ_{cross} and Λ. Contrary to one could expect, as shown in Figure 5.5 (a), Λ did not surpass Λ_{cross}, suggesting that there is no other mechanisms, such as

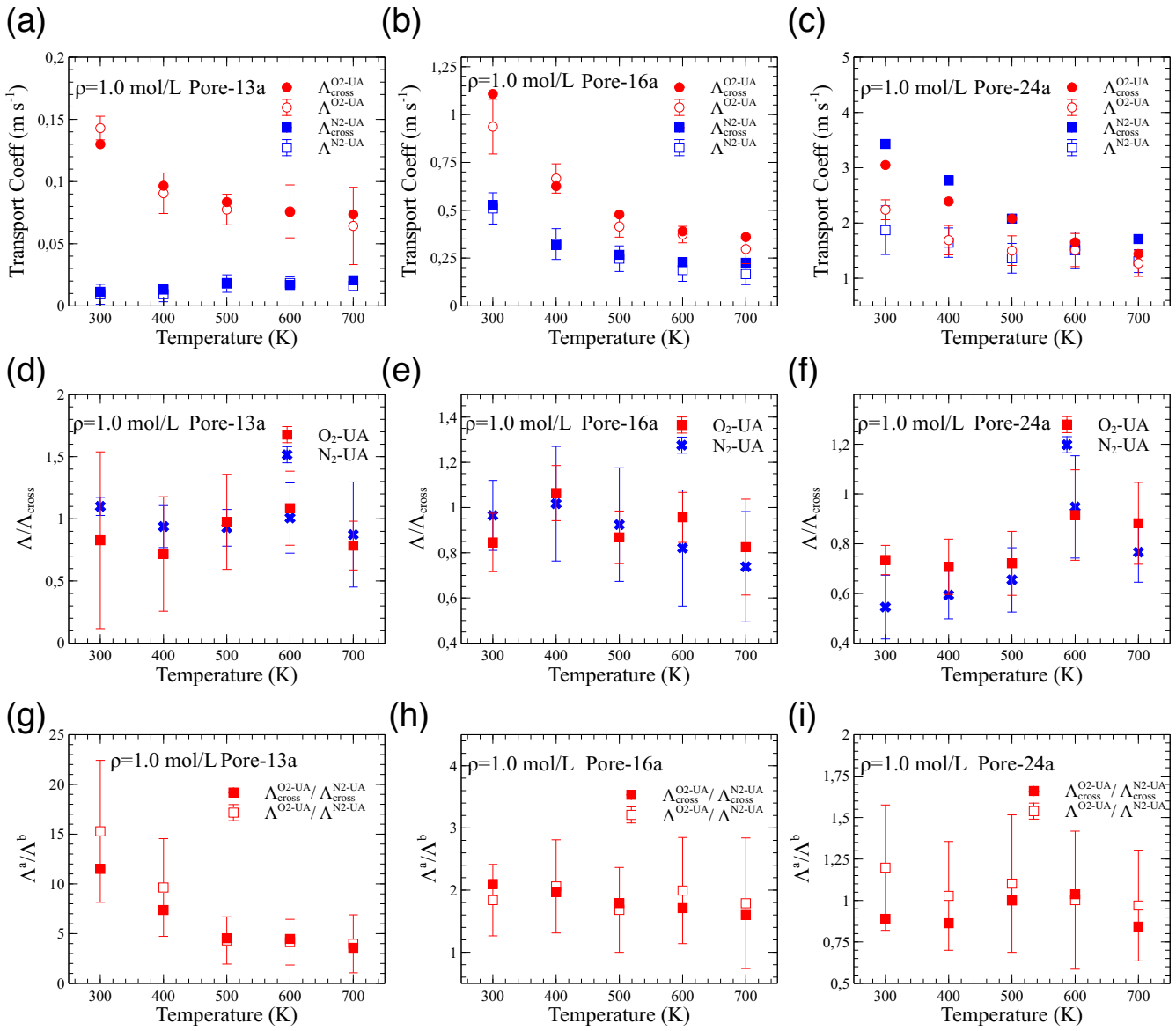

Figure 5.3: Simulated data of cross transport coefficient Λ_{cross} and transport coefficient Λ obtained from our post-treatment algorithms with the combination of $O_2/N_2 - UA - 13a$ (a), $O_2/N_2 - UA - 16a$ (b), $O_2/N_2 - UA - 24a$ (c), and the ratio of Λ/Λ_{cross} for $O_2/N_2 - UA - 13a$ (d), $O_2/N_2 - UA - 16a$ (e), $O_2/N_2 - UA - 24a$ (f), and the ratio of Λ^a/Λ^b, including Λ and Λ_{cross} for $O_2/N_2 - UA - 13a$ (g), $O_2/N_2 - UA - 16a$ (h), $O_2/N_2 - UA - 24a$ (i).

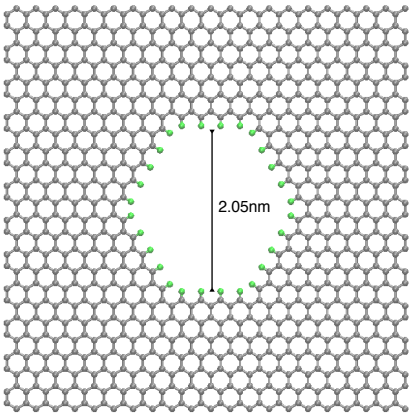

Figure 5.4: Snapshot of one graphene sheet with Pore-2nm.

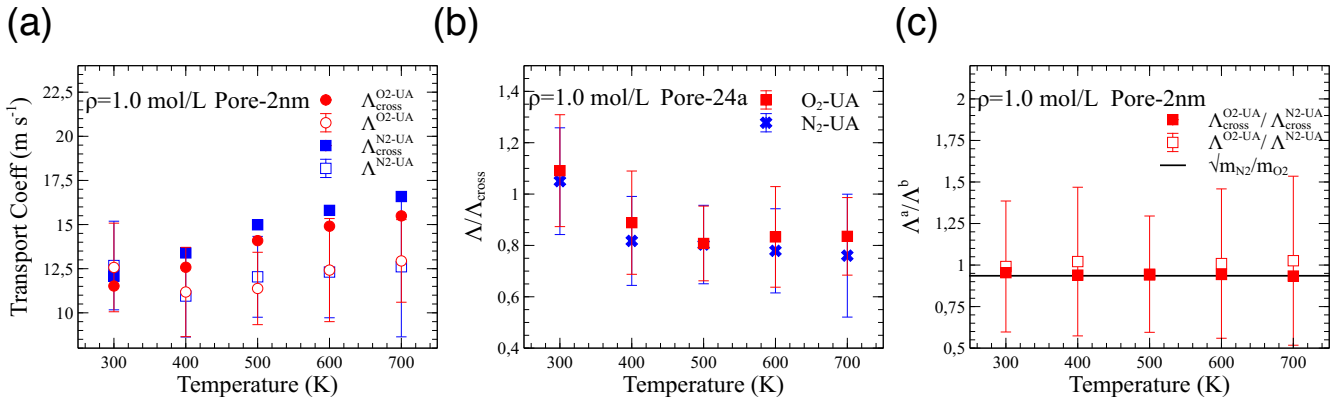

Figure 5.5: (a) Simulated data of cross transport coefficient Λ_{cross} and transport coefficient Λ obtained from our post-treatment algorithms for $O_2 - UA$ and $N_2 - UA$ with Pore-2nm. (b) The ratio of Λ/Λ_{cross} for $O_2 - UA$ and $N_2 - UA$ with Pore-2nm. (c) The ratio of $\Lambda^{O_2-UA}/\Lambda^{N_2-UA}$, including Λ and Λ_{cross} with Pore-2nm

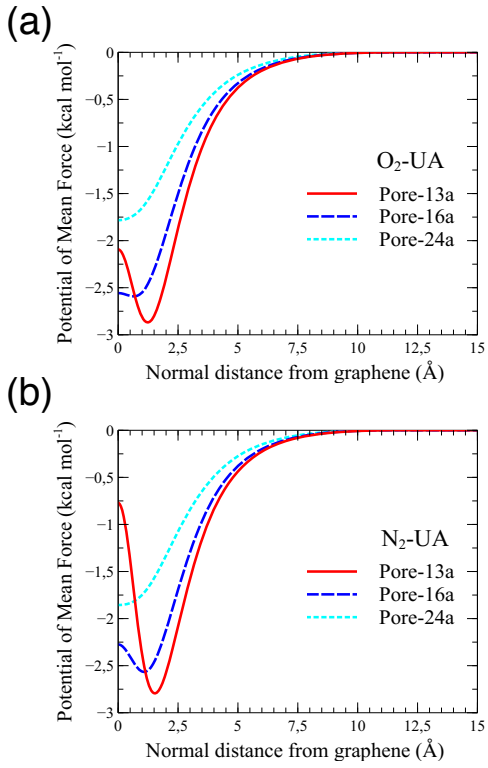

Figure 5.6: PMF profiles of $O_2 - UA$ (a) and $N_2 - UA$ (b) for a range of pore sizes.The PMF is computed along the straight line $(0, 0, z)$ perpendicular to the graphene sheet and is the most favorable path.

hydrodynamic flow, in the permeation process through nanoporous graphene membranes. We can confirm that molecular diffusion is the only mechanism. From Figure 5.5 (b), we observed that $\Lambda/\Lambda_{cross} < 1$. It means that the permeation of $O_2 - UA$ and $N_2 - UA$ with Pore-2nm is in the crossover regime and the effect of the desorption at the edge of the pore can not be neglected. Nevertheless, as shown in Figure 5.5 (c), Λ^a/Λ^b and $\Lambda^a_{cross}/\Lambda^b_{cross}$ approaches $\sqrt{m_b/m_a}$, which is the selectivity in the effusion regime. Under such conditions, we consider that the permeation of $O_2 - UA$ and $N_2 - UA$ gets close to the effusion regime.

5.3.1 Comparison with the Theoretical Model for Λ_{cross}

For spherical gas molecules, the PMF only depends on the position of the gas molecule. We can calculate PMF directly as we did with simplified systems, as shown in Figure 5.6. Thus, we use

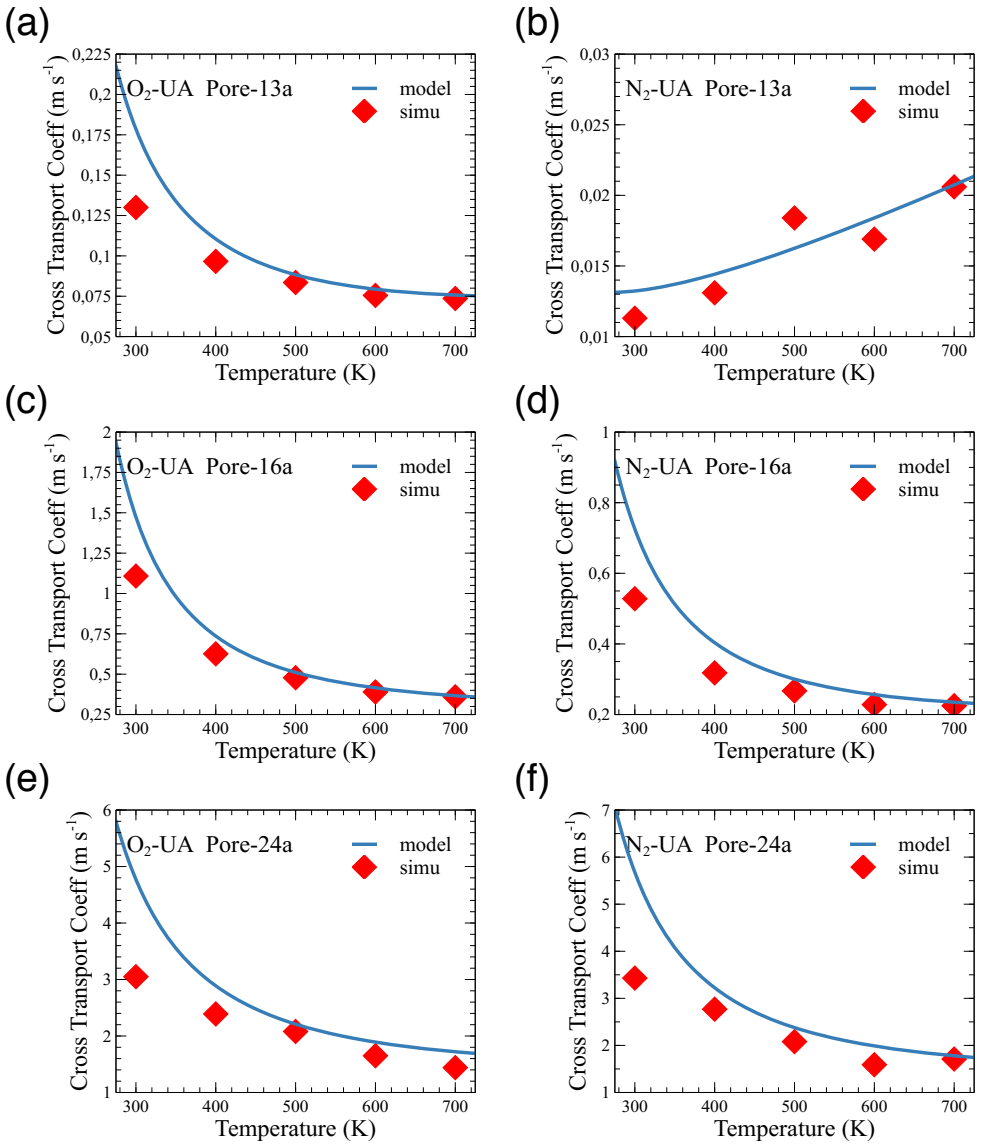

Figure 5.7: Comparison between model predictions (blue lines) and simulation results (red diamonds) for Λ_{cross} with the combination of $O_2 - UA - 13a$ (a), $N_2 - UA - 13a$ (b), $O_2 - UA - 16a$ (c), $N_2 - UA - 16a$ (d), $O_2 - UA - 24a$ (e) and $O_2 - UA - 24a$ (f).

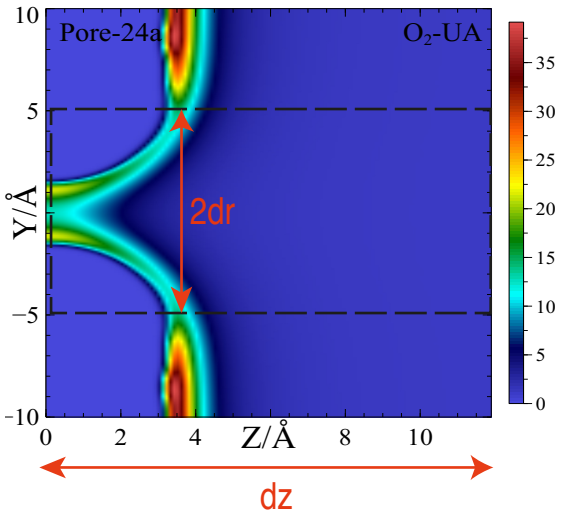

Figure 5.8: The plot of $-\exp(U/kT)$ in the plane YZ at $X = 0$ with T= 300K, where the black dashed rectangle represents the pore mouth region.

our theoretical model for Λ_{cross} directly, expressed as

$$\Lambda_{cross} = \frac{1}{4HW}\sqrt{\frac{8kT}{\pi m}}\int\int dxdy \exp\left(\frac{U_{pmf}(x,y)}{kT}\right) \tag{5.5}$$

In the following figures, the symbols without error bars means that error bars are smaller than the size of symbols. Similar to simplified systems introduced in chapter 4, we can observe an overall good agreement with MD simulation results, as shown in Figure 5.7. Nevertheless, we always notice a tendency to overestimate the transport coefficient. This behavior in realistic graphene-gas system is more evident than in simplified system. Indeed, the adsorption effect is more significant in realistic system and gas molecules are more likely to deviate from the reference trajectory while approaching the pore plane. Thus, it would lead to an overestimation of Λ_{cross}.

5.3.2 Probability of Desorption

To study the probability of desorption for spherical gas molecules, we applied the same method as explained in chapter 4. With this method, we first need to define the pore mouth region. We defined the desorption process as gas molecule moves out from the pore mouth region after crossing the graphene sheet. To determine this region, we focus on the Boltzmann factor $exp(-U(0,y,z)/KT)$, where $U(0,y,z)$ is the potential energy of one gas molecule. In Figure 5.8, we can observe the 2D map of Boltzmann factor, computed in the plane YZ at $X = 0$ for $O_2 - UA$ with Pore-24a at 300K. According to this plot and with the same criteria to define the

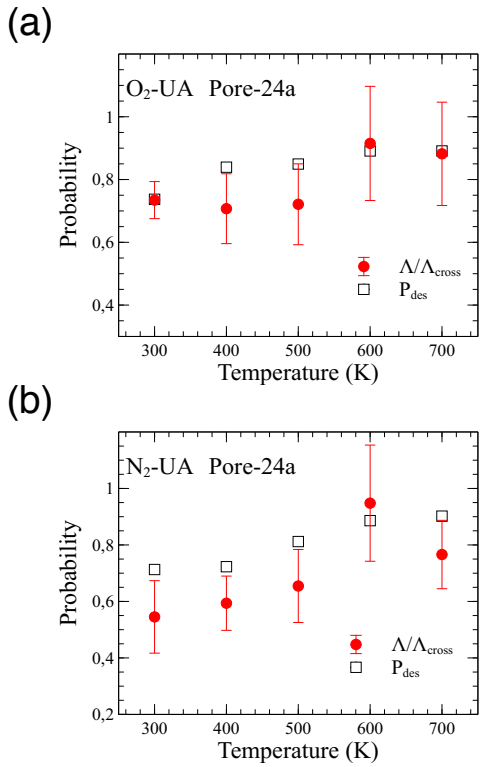

Figure 5.9: Comparison of probabilities between simulated results computed from post-treatment algorithm and the ratio between Λ and Λ_{cross} obtained by NEMD and EMD simulations for $O_2 - UA - 24a$ (a) and $N_2 - UA - 24a$ (b).

pore mouth region as introduced in chapter 4,, we defined the pore mouth region as a cylindrical region centered around the pore. Along Z, the zone of influence of the pore extends to the cutoff distance, resulting in $dz = r_{cut} = 12$Å. Along X/Y, we defined the radius as $dr = r_{pore} + l_{bond}$, where r_{pore} and l_{bond} represent the radius of pore and length of $C - H$ bond, respectively.

In our simulations, we kept track of the molecules remaining in the pore mouth region at each time step. We applied a post-treatment algorithm to compute the probability that molecules that have just crossed the pore desorb from this region, as mentioned in chapter 4. For cases $O_2 - UA - 24a$ and $N_2 - UA - 24a$, P_{des} is shown in Figure 5.9 and we can observe good agreement with the ratio between Λ and Λ_{cross} obtained by NEMD and EMD simulations, which is consistent with the results reported in chapter 4. Table 5.1 summarizes permeation regimes observed for $O_2/N_2 - UA$ as a function of pore size. With pore size increasing, the regime transformed from molecular sieving regime, crossover regime for sub-nanometer pore sizes, and to an almost effusion regime for nanometer pore sizes.

$Gas - Pore$	$13a$	$16a$	$24a$	$2nm$
$O_2 - UA$	sieving	sieving	crossover	crossover/effusion
$N_2 - UA$	sieving	sieving	crossover	crossover/effusion

Table 5.1: Summary of permeation regime for united-atom gas-pore combinations.

5.4 Results obtained for All-Atom Gas Models

In the previous section, we addressed the transport coefficient of spherical gas molecules, where we applied the same method as for the simplified system of chapter 4. Nevertheless, in realistic applications, we generally deal with non spherical gas molecules. In Figure 5.10, we show the simulated transport coefficients Λ_{cross} and Λ, for several kinds of polyatomic gas molecules-pore combinations. Even for the sub-nanometer pore sizes, we find that graphene with relative large pores may act as a size-selective membrane[179, 85, 180, 181]. For instance, CH_4 has a larger kinetic diameter than that of CO_2 but it has also the higher transport coefficient with Pore-24a. Nevertheless, Λ_{cross} of CH_4 is smaller than that of CO_2 under the same conditions. According to our theoretical approach, Λ_{cross} depends on two parameters: thermodynamic factor and accessible porosity. With Pore-24a whose pore size is large enough, the thermodynamic factor is the main contribution to Λ_{cross}. With nanoporous graphene, CO_2 exhibits a more significant adsorption effect than CH_4 resulting in a larger value of Λ_{cross}. When it comes to Λ, we should correct Λ_{cross} by the probability of desorption, as mentioned above. Under such conditions, the probability of desorption of CO_2 is much smaller than that of CH_4. It indicates that CO_2 is more likely to adsorb in the center of the pore than CH_4 making it more difficult to desorb from the pore mouth region.

With Figure 5.11, we can observe several behaviors similar to that of spherical gas molecules. For instance, when it comes to Pore-13a and Pore-16a, the barrier crossing process can also be considered as rate-limiting for CO_2 and CH_4. For $CH_4 - Pore13a$, we could not observe any permeation event during our simulations, indicating that the Pore-13a is almost impermeable to CH_4. With $\Lambda/\Lambda_{cross} \approx 1$, the permeation of CO_2 and CH_4 with Pore-13a and Pore-16a is in the molecular sieving regime. For O_2 and N_2, even with Pore-13a, $\Lambda/\Lambda_{cross} < 1$ as shown in Figure 5.11 (a). For these kinds of pore sizes, the probability of desorption is significantly less than 1 even with Pore-13a and the permeation of O_2 and N_2 is in the crossover regime. Table 5.2 is a summary of permeation regimes observed for all gas-pore combinations. We observed that molecular sieving and crossover regimes are principle regimes with gas molecules permeating through sub-nano pores.

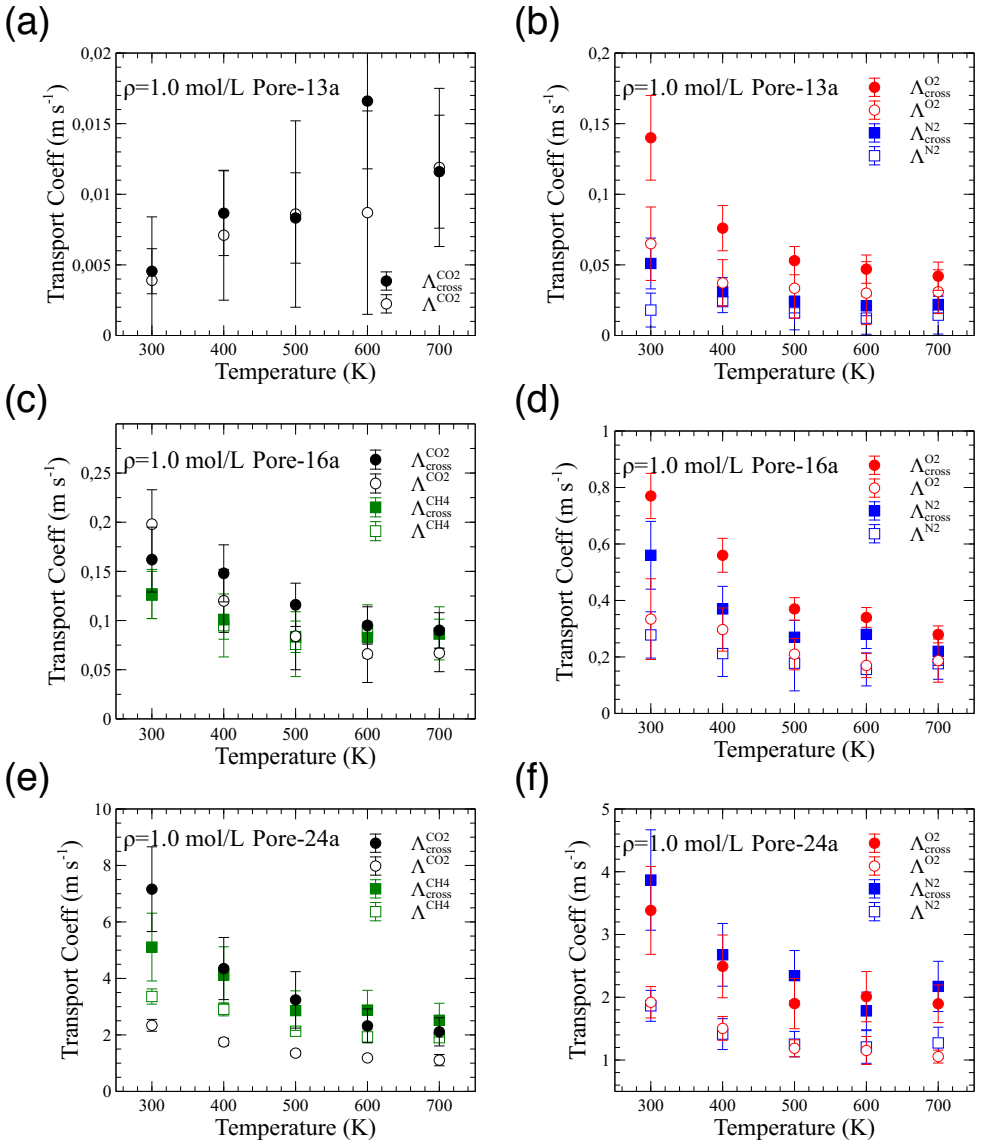

Figure 5.10: Simulated data of cross transport coefficient Λ_{cross} and transport coefficient Λ obtained from our post-treatment algorithms with the combination of $CO_2/CH_4 - 13a$ (a), $O_2/N_2 - 13a$ (b), $CO_2/CH_4 - 16a$ (c), $O_2/N_2 - 16a$ (d), $CO_2/CH_4 - 24a$ (e), $O_2/N_2 - 24a$ (f).

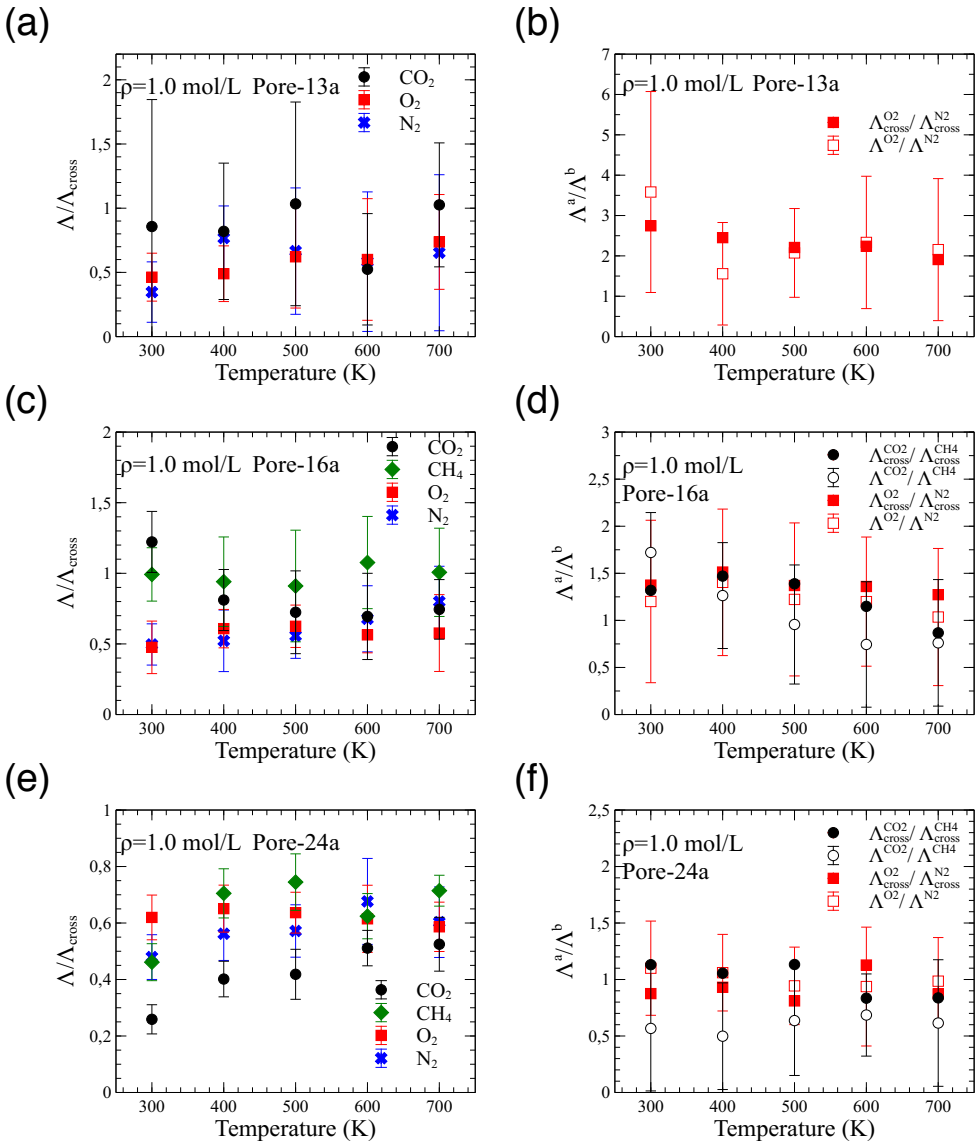

Figure 5.11: The ratio of Λ/Λ_{cross} for $CO_2/O_2/N_2 - 13a$ (a), $CO_2/CH_4/O_2/N_2 - 16a$ (c), $CO_2/CH_4/O_2/N_2 - 16a$ (e), and the ratio of Λ^a/Λ^b, including Λ and Λ_{cross} for $O_2/N_2 - 13a$ (b), $CO_2/CH_4, O_2/N_2 - 16a$ (d), $CO_2/CH_4, O_2/N_2 - 24a$ (f).

$Gas - Pore$	$13a$	$16a$	$24a$
CO_2	sieving	sieving	crossover
CH_4	sieving	sieving	crossover
O_2	crossover	crossover	crossover
N_2	crossover	crossover	crossover

Table 5.2: Summary of permeation regime for all-atom gas-pore combinations.

In the molecular sieving regime, such as CO_2 and CH_4 with Pore-16a, $\Lambda^{CO_2}/\Lambda^{CH_4} \approx \Lambda^{CO_2}_{cross}/\Lambda^{CH_4}_{cross}$ because of $\Lambda/\Lambda_{cross} \approx 1$. With the same pore size, O_2 and N_2 are in the crossover regime as mentioned above. Nevertheless, we observed that $\Lambda^{O_2}/\Lambda^{N_2}$ exhibits similar values to that of $\Lambda^{O_2}_{cross}/\Lambda^{N_2}_{cross}$. The same behavior could be observed with these three pore sizes. It suggests that O_2 and N_2 have similar values of probability of desorption with hydrogen-terminated pore and we can use our theoretical model for Λ_{cross} to predict the separation of this mixture. However, for the crossover regime of CO_2 and CH_4 with Pore-24a, we observed that $\Lambda^{CO_2}/\Lambda^{CH_4} < 1$ while $\Lambda^{CO_2}_{cross}/\Lambda^{CH_4}_{cross} > 1$ because CO_2 and CH_4 exhibit different probabilities of desorption. Under such condition, it indicates that our model can not predict the selectivity directly. Further discussions about gas separation will be introduced in the next chapter.

5.4.1 Comparison with the Theoretical Model for Λ_{cross}

With the methods we used to compute the PMF, we can calculate the theoretical Λ_{cross} as explained in chapter 3. Hereafter, we report and compare the results of our simulations to the theoretical model.

Figure 5.12 shows results obtained for different gas species, including CO_2, CH_4, O_2 and N_2. With pores sizes reducing from 16a to 13a, the error bars on the model prediction become more important. That is because U_w becomes less accurate with fewer molecules passing through the pores. In supercritical condition, the theoretical predictions have overall good agreements with the simulated results. The data obtained for different densities fall in the interval of theoretical predictions within error bars. We observe no significant difference between different densities and there is no obvious trend with density. It implies that our system is dilute enough and the fluid/fluid interaction are negligible. Thus, the solid/fluid interaction is the dominant and the ideal gas limit is suitable to describe supercritical conditions. However, close to the critical point(CO_2 at 300 K), the simulated results of $CO_2 - 16a$ are not in the interval of theoretical prediction and Figure 5.13 (b) shows an obvious trend with density. In this situation, the fluid/fluid

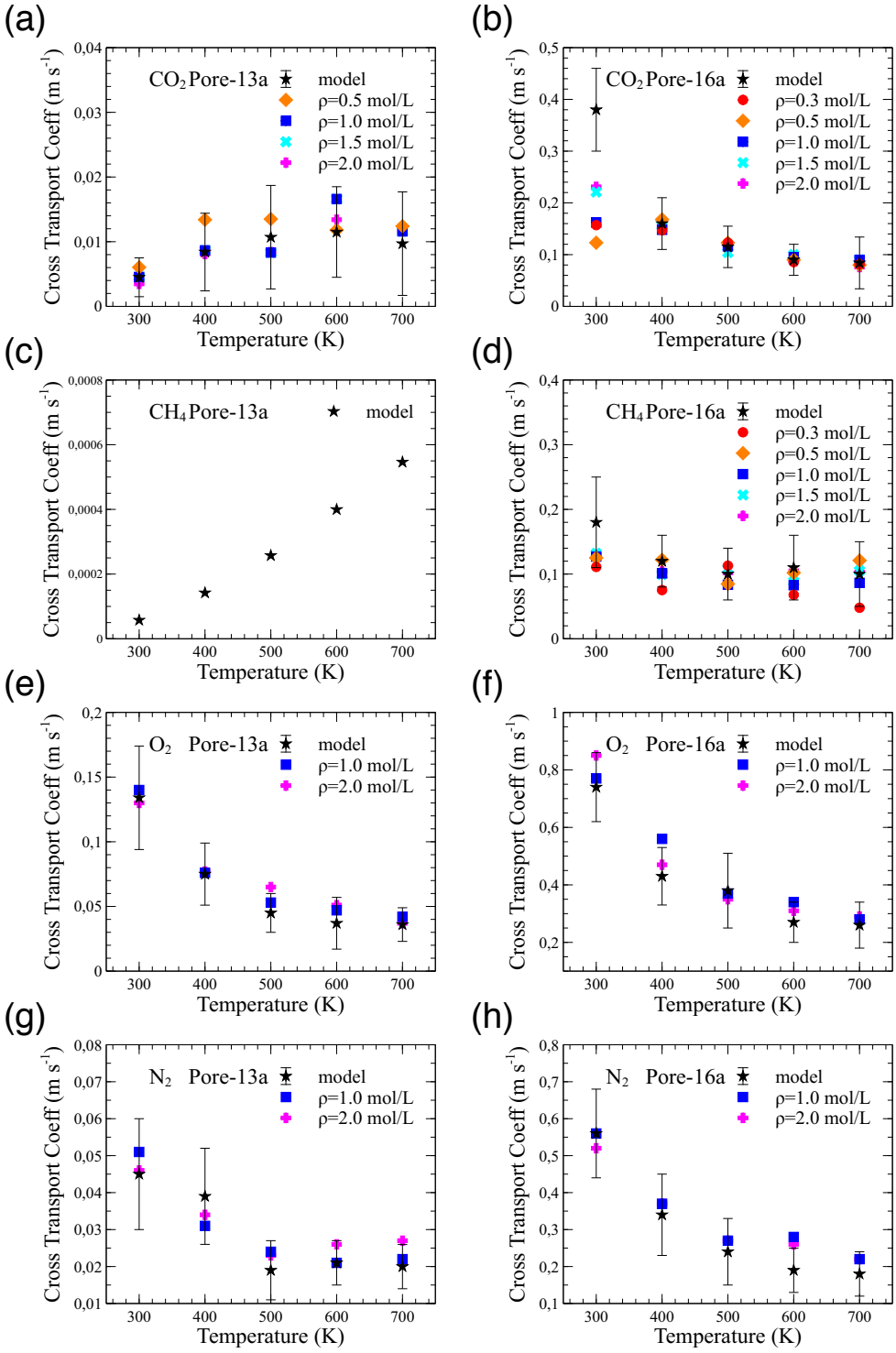

Figure 5.12: Model predictions (black stars) for Λ_{cross} with the combination of $CO_2 - 16a$ (a), $CO_2 - 13a$ (b), $CH_4 - 16a$ (c), $CH_4 - 13a$ (d), $O_2 - 16a$ (e), $O_2 - 13a$ (f), $N_2 - 16a$ (g) and $N_2 - 13a$ (h). Symbols stand for simulated data obtained for original densities ranging from 0.3 mol/L to 2 mol/L.

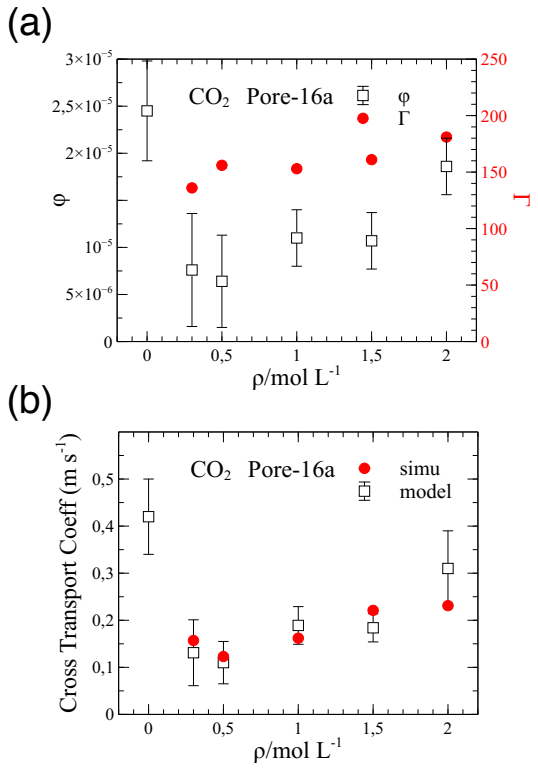

Figure 5.13: Evolution of parameters ϕ and Γ (a), and the comparison of model predictions and simulated results (b) with densities.

interaction cannot be negligible. Another remarkable behavior lies in the trend with temperature that changes with pore size (CO_2 and CH_4 from Pore-16a to Pore-13a). In next sections, we will discuss these specific behaviors, namely, the influence of density and the influence of pore size.

Influence of Density

As introduced in chapter 3, the cross transport coefficient is determined by two parameters, the accessible porosity ϕ and the thermodynamic factor Γ. As analyzed in previous work, the PMF profile along the trajectory (0,0,Z) is not strictly affected by gas density. Thermodynamic factors have similar values with different gas densities because of similar U_∞ as discussed in chapter 3. Figure 5.13 (a) focuses on how the density impacts the accessible porosity. At 300K, we can no longer use a single CO_2 molecule to compute the force field on the surface of graphene sheet because liquid-like density in the adsorption layer enhances fluid/fluid interactions, which provokes additional steric hindrance at the pore mouth. As a result, the value of ϕ obtained from the simulations performed at finite fluid loadings is significantly smaller than that obtained

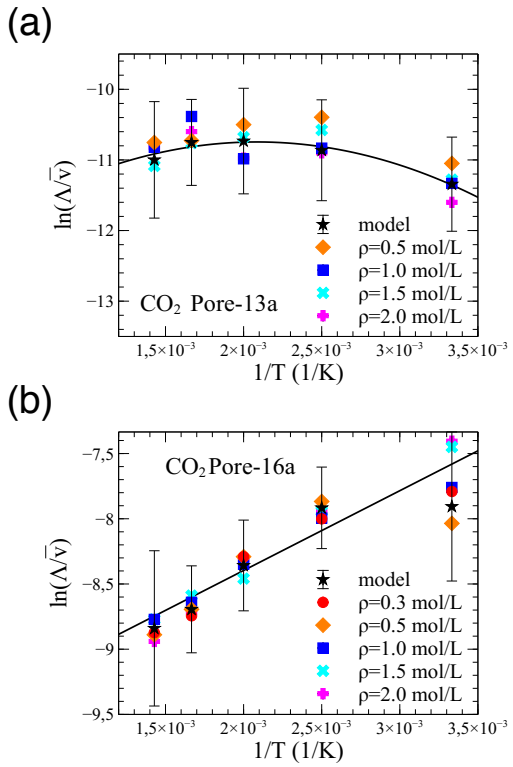

Figure 5.14: Arrhenius plots of the the quantity $\Lambda/\bar{v}$ for the combination $CO_2 - 13a$ (a) and $CO_2 - 16a$ (b), where the model results is modified with $\rho = 1mol/L$ at T=300K. Symbols stand for simulated data obtained for original densities ranging from 0.3 mol/L to 2 mol/L.

with a single CO_2 molecule. Note that the variations of simulated cross transport coefficients and accessible porosities are very similar, suggesting a proportional correlation between these two quantities. We can observe an overall good agreement between simulated results and the theoretical model, when accounting for the finite density PMF. Note that the influence of gas density is not observed with $CO_2 - Pore13a$. This may be because the additional fluid/fluid interaction is negligible compared to the strong repulsive solid/fluid interaction. Therefore, the contribution of the repulsive fluid/fluid interaction is not significant when the pore is small enough.

Influence of Pore Size

In Figure 5.14, we report the quantity $\Lambda/\bar{v}$ in Arrhenius plots for two pore sizes, 13a and 16a. For any kind of gas, increasing the temperature helps the gas molecules to access increasingly larger areas of the pore. On the contrary, it also causes desorption and thus it is more difficult to find molecules in the vicinity of the pore. To explain this behavior with our theoretical model, the

trend of the cross transport coefficient with temperature results from competition between the accessible porosity and the thermodynamic factor. In chapter 3, we reported the trends of these parameters with temperature. These two parameters are determined by U_w and U_∞, respectively. For pore-16a, the barrier crossing process is dominated by adsorption as U_∞ is much larger than U_w. As a consequence, the corresponding Arrhenius plots in Figure 5.14 (b) show a monotonically increasing trend. When it comes to smaller pores, U_∞ and U_w have similar order of magnitude. In this case, the Arrhenius plots as shown in Figure 5.14 (a) exhibit a non-monotonic trend. With temperature decreasing, we indeed observe significant curvature. At high temperature, an increasing trend shows the barrier crossing process is dominated by adsorption, while accessible porosity dominates at low temperature. Similar mechanism has been described by Oublesir et al[144].

5.4.2 Probability of Desorption

For non spherical gas molecules, we use exactly the same criteria to define the pore mouth region, where a cylinder region is defined with $dz = r_{cut}$ and $dr = r_{pore} + l_{bond}$. With the same post-treatment algorithm, we can compute the probability of desorption for different gas-pore combinations. For all-atom gas models, the average re-crossing time $\tau_{recross}$ should be considered as sufficiently long for $P_{des}(t)$ to reach its value even though the barrier crossing process does not dominate the permeation process. Once molecules stop oscillating around their equilibrium position, they will not recross the pore because of the entropic contribution of rotations. The results are shown in Figure 5.15. In the following, the parameter P_{des} will therefore stand for the long time asymptotic limit of P_{des}(t). We can observe good agreement with the ratio between Λ and Λ_{cross} obtained by NEMD and EMD simulations. With temperature increasing, the value of the desorption probability increases, which is consistent with the results reported in chapter 4. Nevertheless, for O_2 and N_2, there is no obvious increasing of probability when reducing the pore size from Pore-24a to Pore-13a. It indicates that these pore sizes are large enough so that the permeation of O_2 and N_2 is in the crossover regime.

5.5 Conclusion

In this chapter, we have performed EMD and NEMD simulations to investigate the permeation of different gas-pore combinations through single layer nanoporous graphene membranes under various thermodynamic conditions. We confirmed that molecular diffusion is the only mechanism in the permeation process of gas through nanoporous graphene. For united-atom gas models, we

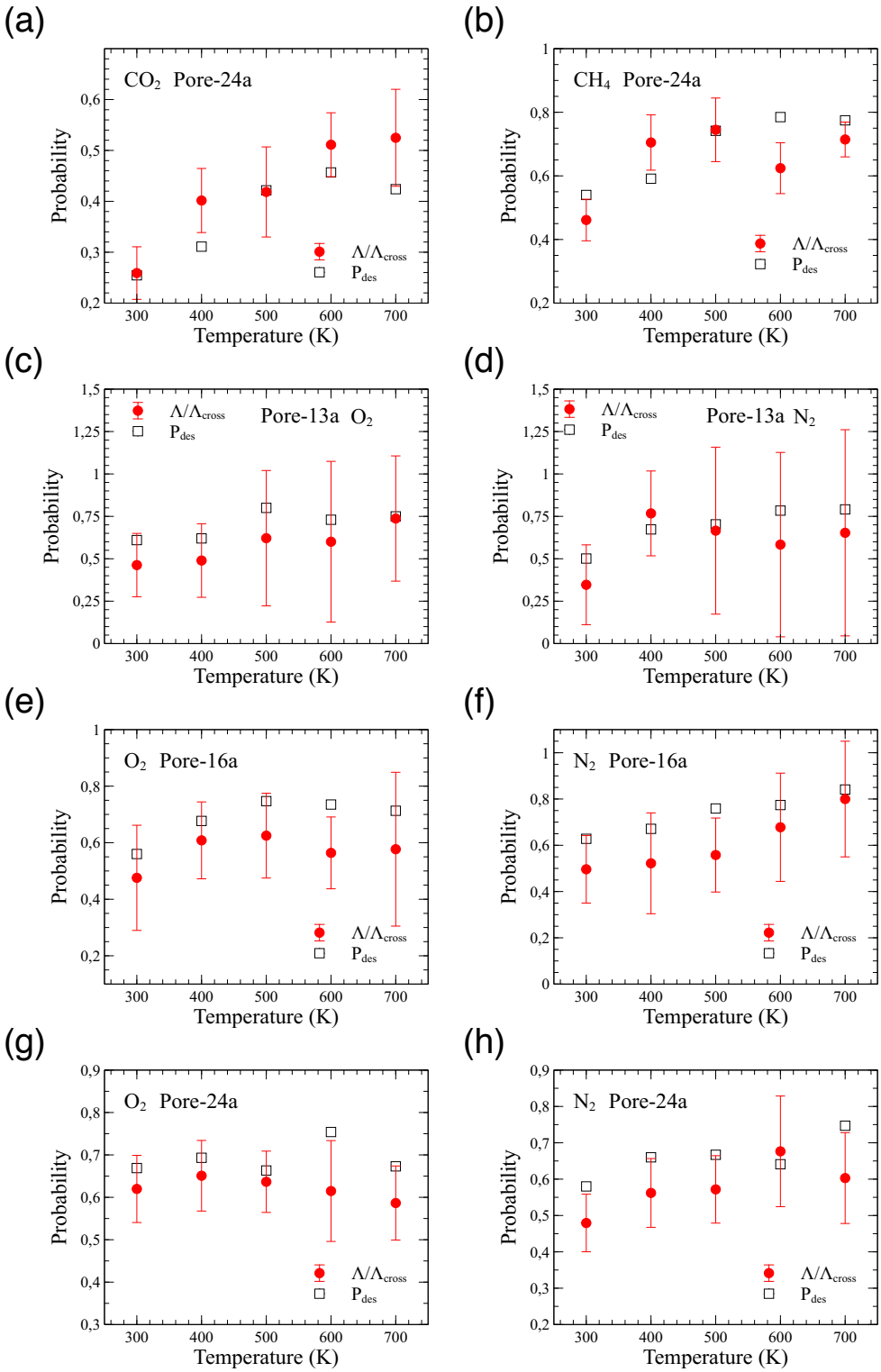

Figure 5.15: Comparison of probabilities between simulated results computed from post-treatment algorithm and the ratio between Λ and Λ_{cross} obtained by NEMD and EMD simulations for $CO_2 - 24a$ (a), $CH_4 - 24a$ (b), $O_2 - 13a$ (c), $N_2 - 13a$ (d), $O_2 - 16a$ (e), $N_2 - 16a$ (f), $O_2 - 24a$ (g), $N_2 - 24a$ (h).

applied our theoretical model directly and we observed similar behaviors to those obtained with the simplified system of chapter 4. For sub-nanometer pore sizes, including Pore-13a, 16a and 24a, the permeation of gas is either in the molecular sieving or in the crossover regime. When the pore is significantly larger, e.g. Pore-2nm in this study, the permeation regime gets close to the effusion regime.

For all-atom gas models, the permeation of different gas species is either in molecular sieving or in the crossover regime with sub-nanometer pore sizes, which is consistent with the results obtained for united-atom. Using the methods discussed in chapter 3, we succeeded in applying our theoretical model to a realistic graphene-gas system. In supercritical conditions, the theoretical predictions of Λ_{cross} are in overall good agreement with simulation results. Close to the critical temperature, our theoretical model is correct provided we account for the consideration of fluid/fluid interactions. It indicates that our theoretical model may be applied to the permeation of liquid. In the molecular sieving regime, where $\Lambda/\Lambda_{cross} \approx 1$, our results suggest that the semi-empirical Arrhenius equation is not sufficient to capture the subtle influence of temperature on the transport coefficient. This is the competition between the adsorption effect and the accessible porosity. Importantly, we confirm that our theoretical model is suitable for all scales of pore sizes, including all kinds of gas permeation regimes through nanoporous graphene membranes.

Chapter 6

Gas Separation through Single-layer Nanoporous Graphene

Contents

In previous chapters, we investigated pure gas permeation through single layer nanoporous graphene membranes. Studying both simplified and realistic systems, we confirmed that molecular diffusion is the only permeation mechanism in the dilute gas conditions we explored. We also proposed a semi-predictive theoretical model to explain the mechanisms and predict the transport coefficients. We observed good agreement with simulation results.

In this chapter, based on the knowledge acquired on the permeation of pure compounds, we focus on gas mixture permeation and gas pairs selectivity through nanoporous graphene membranes. After defining the concept of selectivity, we present the results of molecular simulations performed with gas mixtures. We will show in which cases the results we obtained for pure compounds, and consequently our theoretical model, allow us to predict the selectivity of mixtures. We will also discuss the cases in which the data for pure compounds do not extrapolate to the

case of mixtures. Under these conditions, we show that by feeding the theoretical model with molecular simulation data that take into account the non-ideality of certain mixtures, we can correctly predict the separation factors.

6.1 Definition of Separation Factor

In this chapter, we used the DCV-GCMD technique and performed NEMD simulations. The simulation details are the same as introduced in chapter 5. We performed NEMD simulations with different gas pairs to observe the selectivity of the membrane. In these simulations, we maintained the density jump of 1mol/L between upstream reservoir and downstream reservoir. We measured selectivity by means of the simulated separation factor f_s of gas mixtures, defined as the ratio of the flux of component a to the flux of component b weighted by the inverse of the molar fractions(equation 6.1).

$$fs^{mix} = \frac{j_a\, x_b}{j_b\, x_a} \tag{6.1}$$

With the definition of transport coefficient, j_a and j_b can be expressed as:

$$\begin{aligned} j_a &= \Lambda^a_{mix} x_a \Delta\rho \\ j_b &= \Lambda^b_{mix} x_b \Delta\rho \end{aligned} \tag{6.2}$$

where Λ^a_{mix} and Λ^b_{mix} are the transport coefficient in mixtures of component a and b respectively. Herein, fs^{mix} can also be expressed as:

$$fs^{mix} = \frac{\Lambda^{mix}_a}{\Lambda^{mix}_b} \tag{6.3}$$

In the previous chapter, we investigated the transport coefficient of several pure compounds with different pore sizes. Confrontation between the predictions of our theoretical model and simulations data yields satisfactory results for different pore sizes and thermodynamic conditions. So in this chapter, we would like to investigate if we can apply the results of pure compounds to predict separation factors. To compare the results between gas mixtures and pure gas, we define a separation factor from the transport coefficient of pure gas:

$$fs^{pure} = \frac{\Lambda_a}{\Lambda_b} \tag{6.4}$$

where Λ_a and Λ_b are the transport coefficient of pure compound a and b, respectively. According to our theoretical model, $\Lambda = P_{des}\Lambda_{cross}$, thus, fs^{pure} can be expressed as:

$$fs^{pure} = \frac{P^a_{des}}{P^b_{des}} fs^{cross} \tag{6.5}$$

where fs^{cross} is defined as

$$fs^{cross} = \frac{\Lambda^a_{cross}}{\Lambda^b_{cross}} \tag{6.6}$$

In the following sections, we compare the results of fs^{mix} and fs^{pure}. These results can be divided in two cases:

- If $fs^{mix} \approx fs^{pure}$, the mixture exhibits an ideal behavior, suggesting that the separation factor does not depend on the gas compositions. The case of ideal mixtures can further be split in two sub-cases

  - If $fs^{mix} \approx fs^{cross}$, we can use the model of Λ_{cross} to predict the selectivity of the membrane. Obviously, this situation occurs when both gas species permeate in the molecular sieving regime, as $P^a_{des} \approx P^b_{des} \approx 1$. However, in the crossover regime, P^a_{des} or P^b_{des} may not be equal to 1. Nevertheless, if P^a_{des} and P^b_{des} exhibit similar values, leading to $P^a_{des}/P^b_{des} \approx 1$, we can use the theoretical model for Λ_{cross} to predict separation factors as discussed above.

  - If $fs^{mix} \neq fs^{cross}$, the theoretical model for Λ_{cross} cannot be used directly. This situation occurs in the crossover regime when $P^a_{des}/P^b_{des} \neq 1$. Under such conditions, we have to include the pre-factor P^a_{des}/P^b_{des} computed from simulations to obtain accurate predictions of separation factors.

- If $fs^{mix} \neq fs^{pure}$, the mixture exhibits a non ideal behavior. Under such conditions, we cannot predict fs^{mix} from the results of pure compounds. However, we can compute PMF from simulations of gas mixtures and use the theoretical model for Λ_{cross} to compute fs^{cross} under gas mixture conditions.

Figure 6.1 shows the values of pre-factor P^a_{des}/P^b_{des} computed from the simulations of pure compound. As mentioned in the previous chapter, the permeation of CO_2, CH_4, $O_2 - UA$, $N_2 - UA$ with Pore-13a and Pore-16a is in the molecular sieving regime. With $P^a_{des} \approx P^b_{des} \approx 1$, the pre-factor is thus approximately equal to 1. For other gas-pore combinations, the permeation of gas is in the crossover regime. Nevertheless, we observe that $O_2/N_2 - UA$ with Pore-24a, as well as O_2/N_2 with Pore-13a, Pore-16a and Pore-24a also exhibit values of pre-factor $P^a_{des}/P^b_{des} \approx 1$ because $O_2/O_2 - UA$ and $N_2/N_2 - UA$ have similar probabilities of desorption with hydrogen-terminated pores. On the other hand, for $CO2/CH4$ with Pore-24a, the pre-factor is obviously less than 1. As discussed above, we may need to account for the term P^a_{des}/P^b_{des} to quantify fs in the crossover regime:

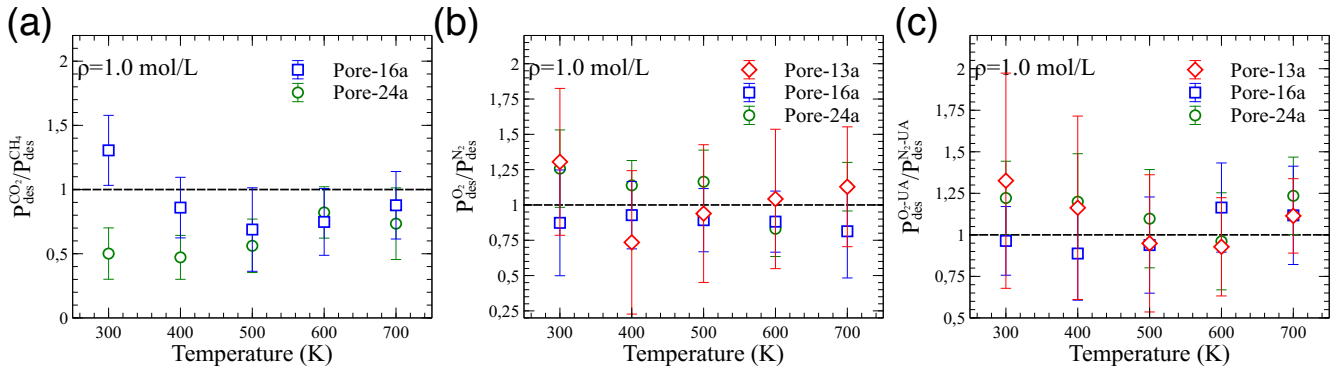

Figure 6.1: (a) $P_{des}^{CO_2}/P_{des}^{CH_4}$ with Pore-16a and Pore-24a, (b) $P_{des}^{O_2}/P_{des}^{N_2}$ with Pore-13a, Pore-16a and Pore-24a, (c) $P_{des}^{O_2-UA}/P_{des}^{N_2-UA}$ with Pore-13a, Pore-16a and Pore-24a.

- For ideal gas mixtures, because the mixing does not affect the gas permeation process, we do not expect the value of P_{des} to be influenced by the mixing.

- For non ideal gas mixtures, in the crossover regime, we assume that the mixing mainly affects Λ_{cross}.

Thus, in this chapter, we use the values of P_{des} computed from simulations of pure compounds to compute P_{des}^a/P_{des}^b in eq 6.5. Herein, we expected to use eq 6.5 to calculate the separation factor of CO_2/CH_4 mixtures through Pore-24a. For other cases, we will use eq 6.6 directly.

6.2 Gas Separation in the Effusive Regime

In the case of large pores, the regime of gas separation is effusive[142, 182]. As described in chapter 5, the permeation of $O_2 - UA$ and $N_2 - UA$ gets close to the effusion regime. Figure 6.2 shows the simulation results of equimolar $O_2/N_2 - UA$ mixtures with Pore-2nm. We can observe that the simulated separation factor can be considered as constant with temperature and is in good agreement with the theoretical prediction $\sqrt{m_{N_2}/m_{O_2}}$. In most cases, gas effusion does not offer sufficient performance in terms of separation. In particular, it does not allow to play on the thermodynamic conditions to control the separation factors In the following, we focus on molecular sieving and crossover regimes which offer more possibilities in terms of gas separation, but we report the $\sqrt{m_b/m_a}$ value as a lower limit of the separation factor.

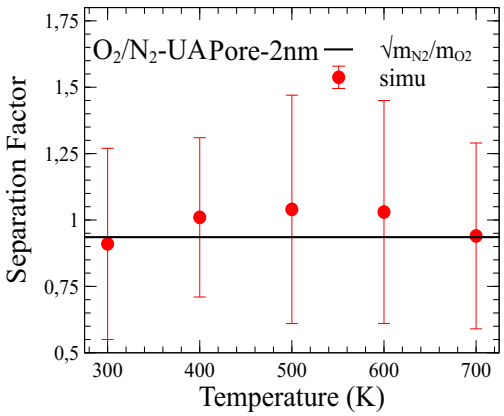

Figure 6.2: Comparison of separation factor between model predictions and simulated results for $O_2/N_2 - UA$ mixtures with Pore-2nm.

6.3 Gas Separation in the Molecular Sieving and Crossover Regimes

Figure 6.3 shows the comparison between fs^{mix} and fs^{pure} for different cases of gas separation. We observed that O_2/N_2 and $O_2 - UA/N_2 - UA$ can be considered as ideal gas mixtures in the conditions of our simulations because $fs^{mix} \approx fs^{pure}$. However, for CO_2/CH_4, significant discrepancies between fs^{mix} and fs^{pure} can be observed at low temperature (close to the critical temperature of CO_2). Under such conditions, CO_2/CH_4 mixtures should be considered as non ideal gas mixtures.

Figure 6.4 and Figure 6.5 show respectively the evolution of flux and transport coefficient with gas compositions at 300K for Pore-16a and Pore-24a. We observed that the trend of flux of $O_2/O_2 - UA$ and $N_2/N_2 - UA$ is linear and the transport coefficient can be considered as constant with the evolution of gas compositions. Therefore, we can confirm that the O_2/N_2 and $O_2 - UA/N_2 - UA$ mixtures behave as ideal mixtures in our simulations. Nevertheless, in CO_2/CH_4 mixtures, the trend of flux of CH_4 is not linear and the transport coefficient of CH_4 increases with molar fraction of CH_4. Under such conditions, the CO_2/CH_4 mixtures can not be considered as ideal gas mixtures as mentioned above.

6.3.1 Separation of Ideal Gas Mixtures

With ideal gas mixtures, we may directly apply our theoretical model for transport coefficients of pure gas to predict the separation factor. Figure 6.6 shows the comparison of separation factors

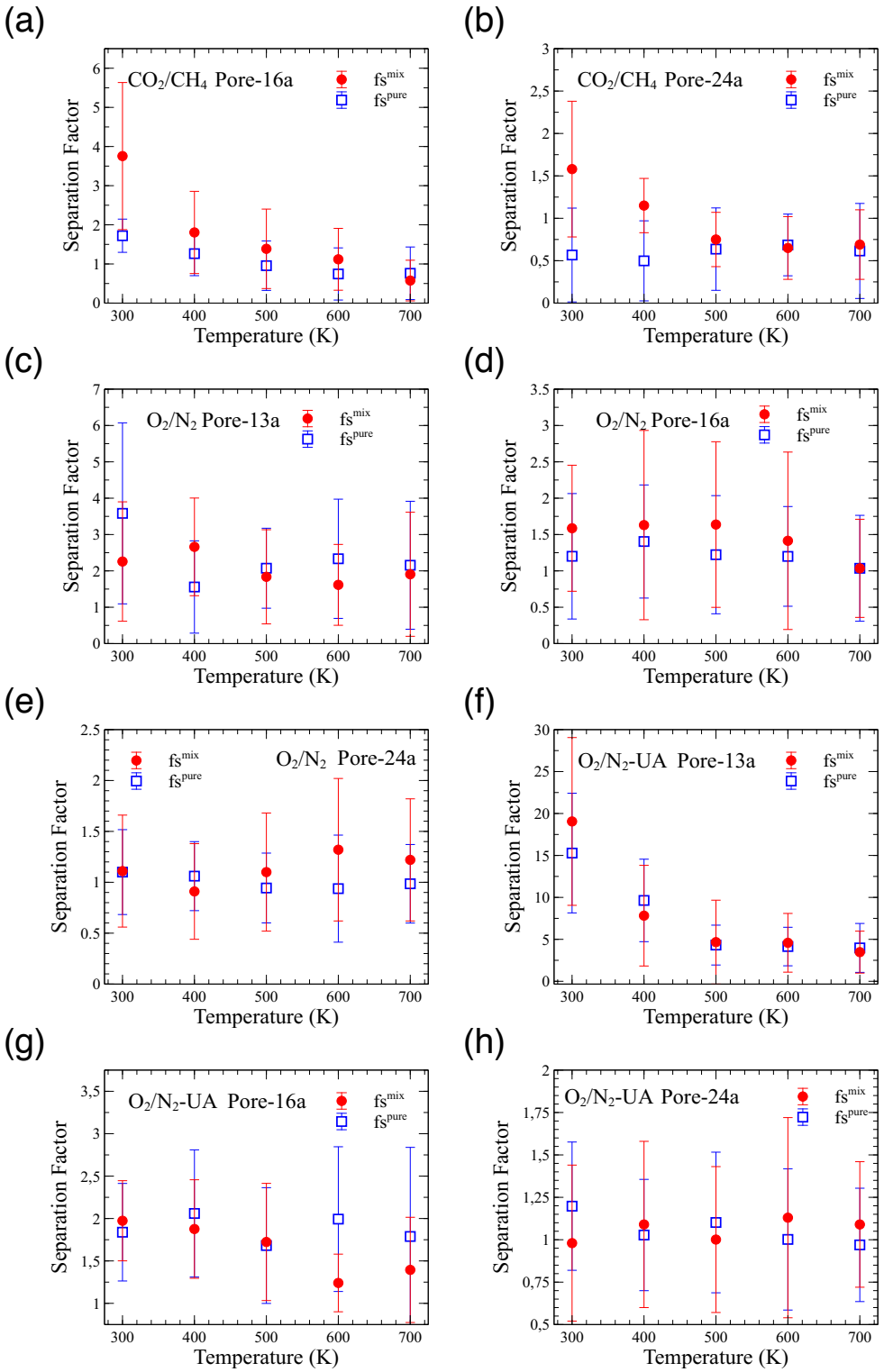

Figure 6.3: Comparison between fs^{mix} and fs^{pure} for $CO_2/CH_4 - 16a$ (a), $CO_2/CH_4 - 24a$ (b), $O_2/N_2 - 13a$ (c), $O_2/N_2 - 16a$ (d), $O_2/N_2 - 24a$ (e), $O_2/N_2 - UA - 13a$ (f), $O_2/N_2 - UA - 16a$ (g) and $O_2/N_2 - UA - 24a$ (h).

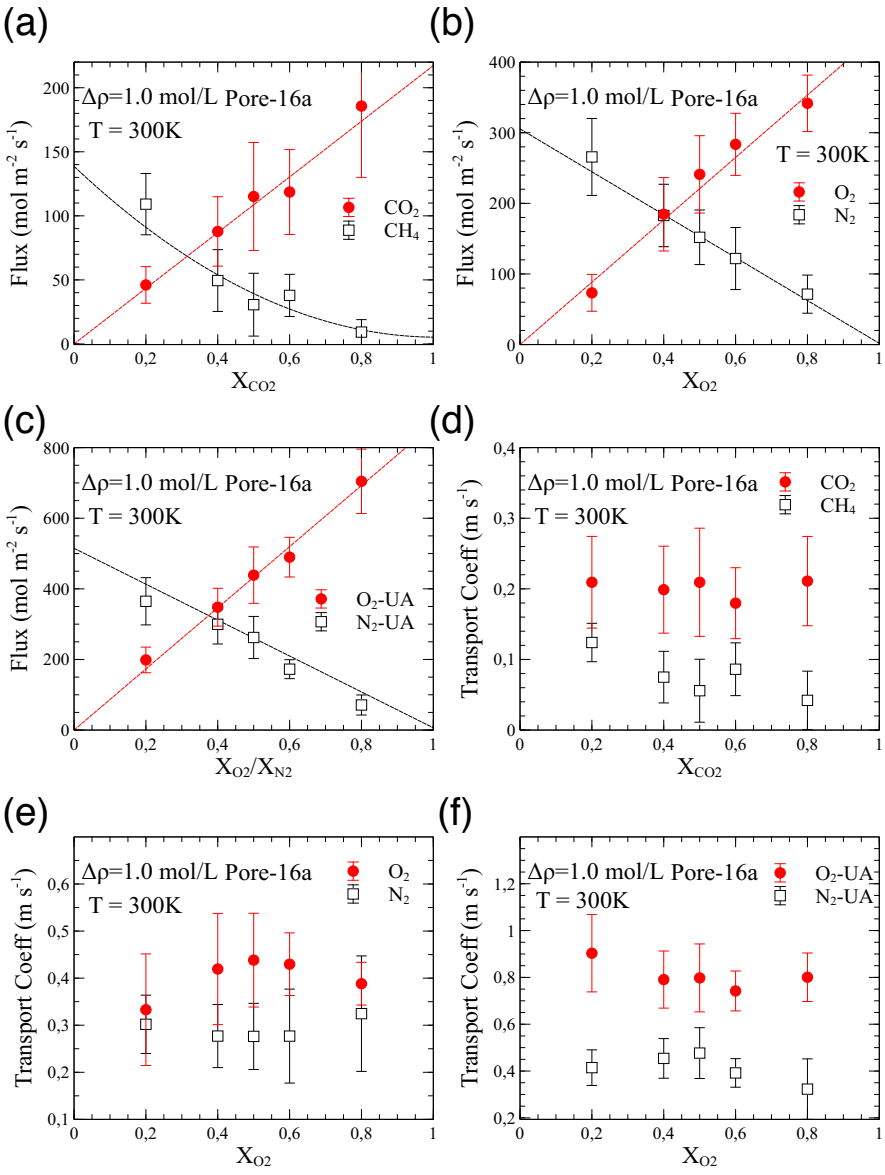

Figure 6.4: The evolution of flux (a) and transport coefficient (d) for CO_2 and CH_4 with gas compositions at 300K for Pore-16a. The evolution of flux (b) and transport coefficient (e) for O_2 and N_2 with gas compositions at 300K with gas gas compositions at 300K for Pore-16a. The evolution of flux (c) and transport coefficient (f) for $O_2 - UA$ and $N_2 - UA$ with gas gas compositions at 300K with gas compositions at 300K for Pore-16a.

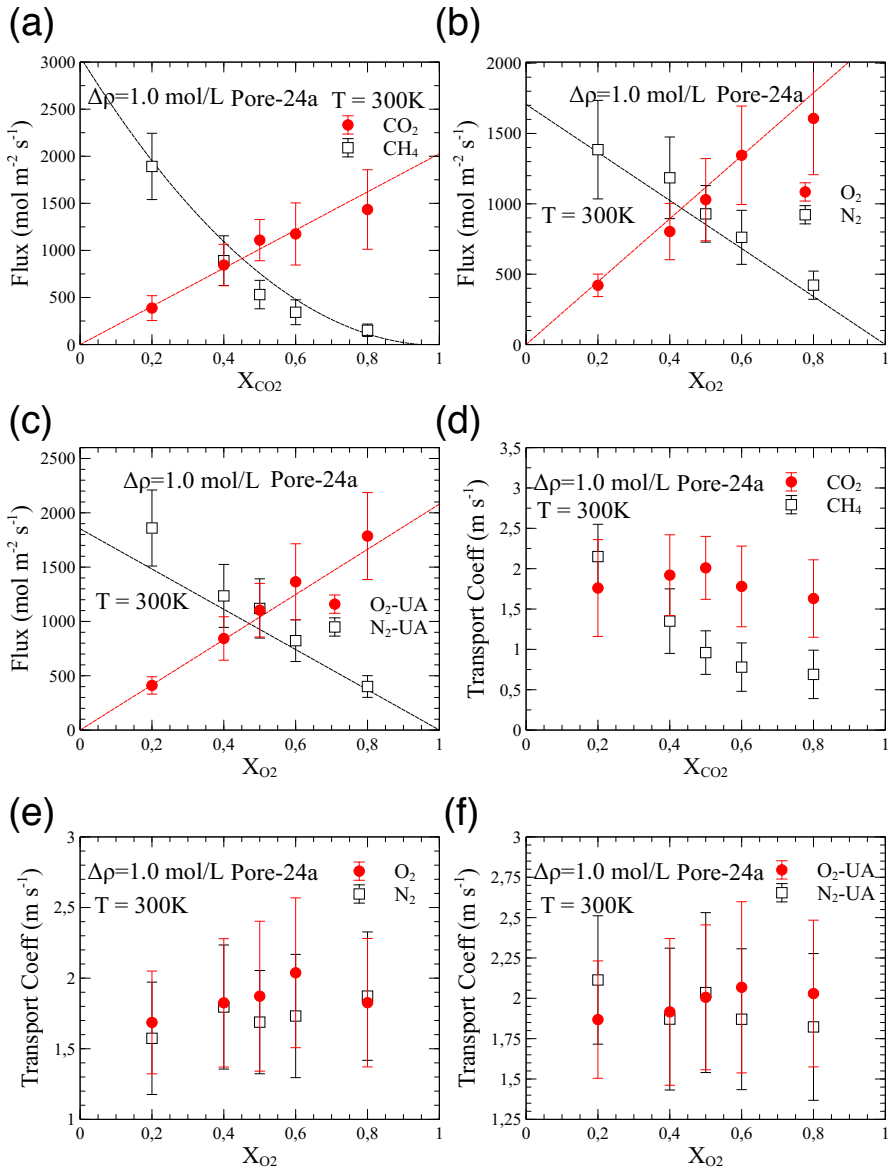

Figure 6.5: The evolution of flux (a) and transport coefficient (d) for CO_2 and CH_4 with gas gas compositions at 300K for Pore-24a. The evolution of flux (b) and transport coefficient (e) for O_2 and N_2 with gas gas compositions at 300K with gas gas compositions at 300K for Pore-24a. The evolution of flux (c) and transport coefficient (f) for $O_2 - UA$ and $N_2 - UA$ with gas gas compositions at 300K with gas compositions at 300K for Pore-24a.

between simulation results and model predictions. In this section, the definition of $(fs^{pure}_{cross})_{model}$ is expressed as

$$(fs^{pure}_{cross})_{model} = \frac{(\Lambda^{a}_{cross})_{model}}{(\Lambda^{b}_{cross})_{model}} \tag{6.7}$$

where $(\Lambda^{a}_{cross})_{model}$ and $(\Lambda^{b}_{cross})_{model}$ are the model predictions of cross transport coefficients for pure compound a and b. The theoretical model and methods to compute theoretical predictions were introduced in chapter 3. In chapter 5, we observed good agreement with simulation results. In this chapter, we therefore directly apply the results obtained in chapter 5 to compute $(fs^{pure}_{cross})_{model}$.

In addition to $(fs^{pure}_{cross})_{model}$, we define $(fs^{pure})_{model}$, expressed as

$$(fs^{pure})_{model} = \frac{P^{a}_{des}}{P^{b}_{des}}(fs^{pure}_{cross})_{model} \tag{6.8}$$

where P_{des} is computed from simulations, as introduced in chapter 5. In this chapter, the values of P^{a}_{des}/P^{b}_{des} can be obtained from Figure 6.1, as we assume that mixing has no influence on the probability of desorption. In Figure 6.6, we observed that both $(fs^{pure})_{model}$ and $(fs^{pure}_{cross})_{model}$ have good agreement with simulation results. It is because $P^{a}_{des} \approx P^{b}_{des} \approx 1$ in the molecular sieving regime, such as observed for $O_2/N_2 - UA$ with Pore-13a and Pore-16a. In the crossover regime, O_2 and N_2 have similar probabilities of desorption with these types of pore.

Figure 6.7 shows the evolution of separation factor with gas compositions. We observed that the separation factor does not exhibit a clear trend with the gas composition. It confirms that the O_2/N_2 mixtures behave as ideal mixtures. Under such conditions, our model is predictive. Note that Pore-24a is not interesting for the O_2/N_2 separation process because its selectivity approached the effusive regime selectivity $\sqrt{m_{N_2}/m_{O_2}}$.

6.3.2 Separation of Non Ideal Gas Mixtures

In previous sections, we proved that CO_2/CH_4 mixtures are non-ideal gas mixtures in the conditions of our simulations, especially at low temperature. Under such conditions, we cannot continue to use the results of pure gas to predict separation factors. In Figure 6.4 and Figure 6.5, we observe that the mixing of CO_2/CH_4 mainly affects the transport coefficient of CH_4. To investigate this effect, we performed NEMD simulations with equimolar CO_2/CH_4 mixtures. We re-computed PMF profiles of CH_4 from simulations with gas mixtures.

For Pore-16a, significant discrepancies between U^{mix}_{∞} and U^{pure}_{∞} at low temperature can be observed. It indicates that the presence of CO_2 molecules is likely to decrease the adsorption of CH_4. For Pore-24a, the pore size is large enough for the local potential minimum to lie in the

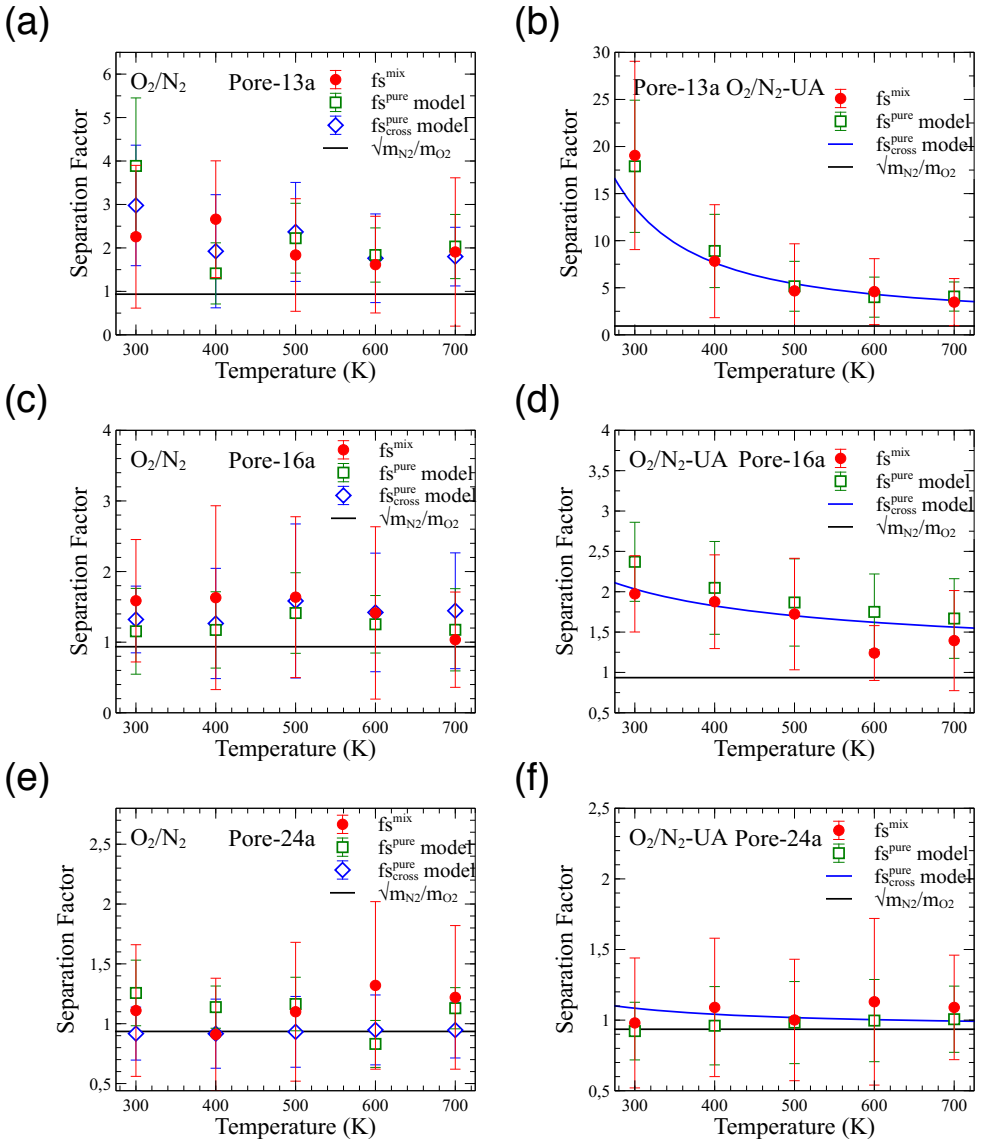

Figure 6.6: Simulation results and model predictions of separation factor for O_2/N_2 with Pore-13a (a), Pore-16a (c) and Pore-24a (e). Simulation and model predictions of separation factor for $O_2/N_2 - UA$ with Pore-13a (b), Pore-16a (d) and Pore-24a (f).

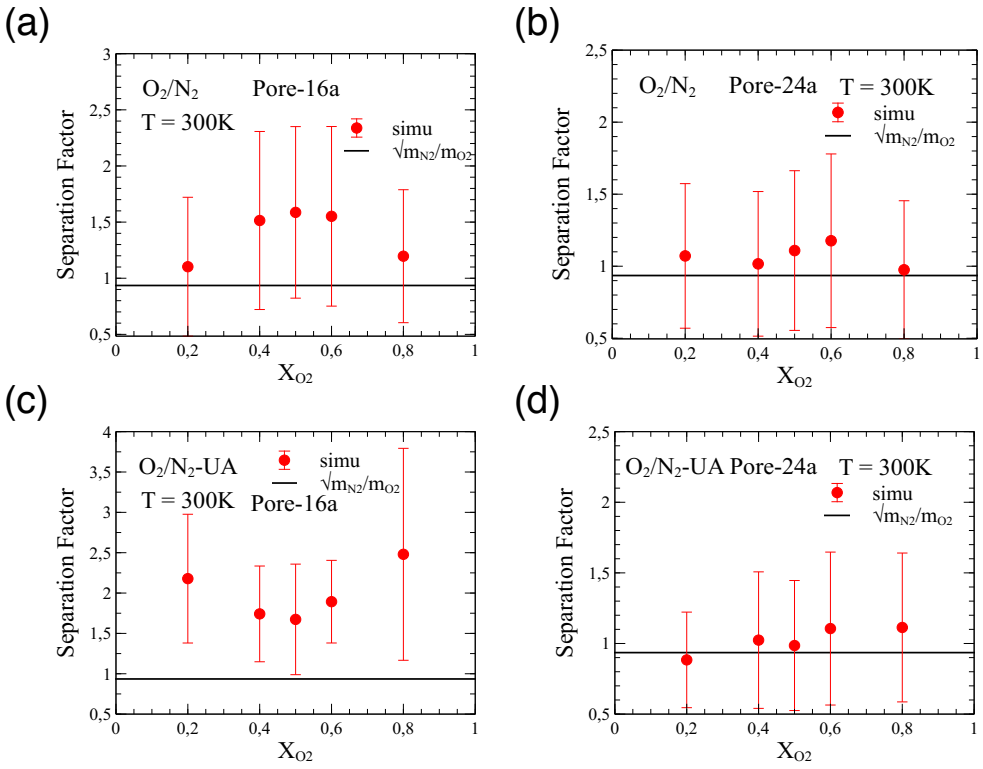

Figure 6.7: The evolution of separation factor with gas composition for O_2/N_2 with Pore-16a (a), Pore-24a (b) at 300K. The evolution of separation factor with gas composition for $O_2/N_2 - UA$ with Pore-16a (c), Pore-24a (d) at 300K.

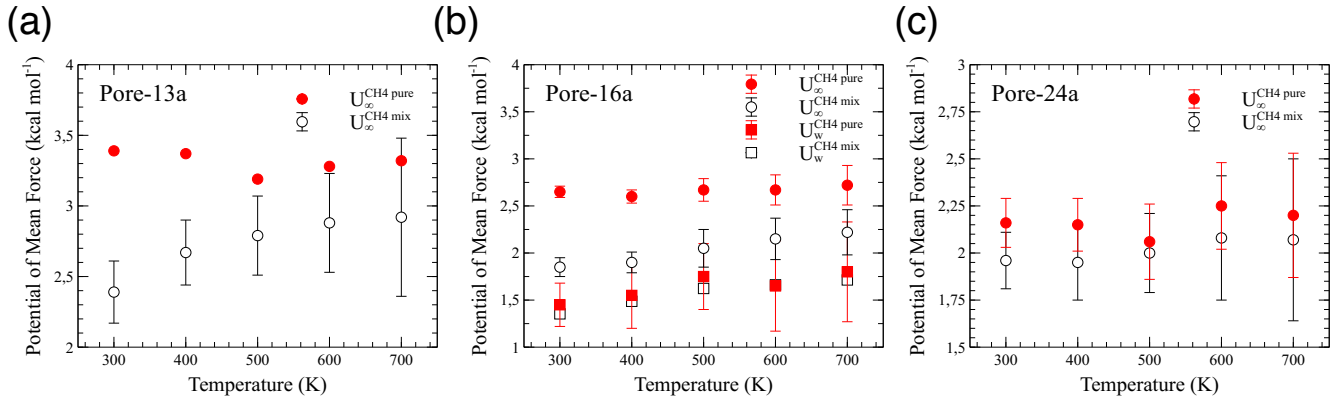

Figure 6.8: Comparison of U_∞ and U_w between pure CH_4 and CH_4 in CO_2/CH_4 mixtures with Pore-13a (a), Pore-16a (b) and Pore-24a (c).

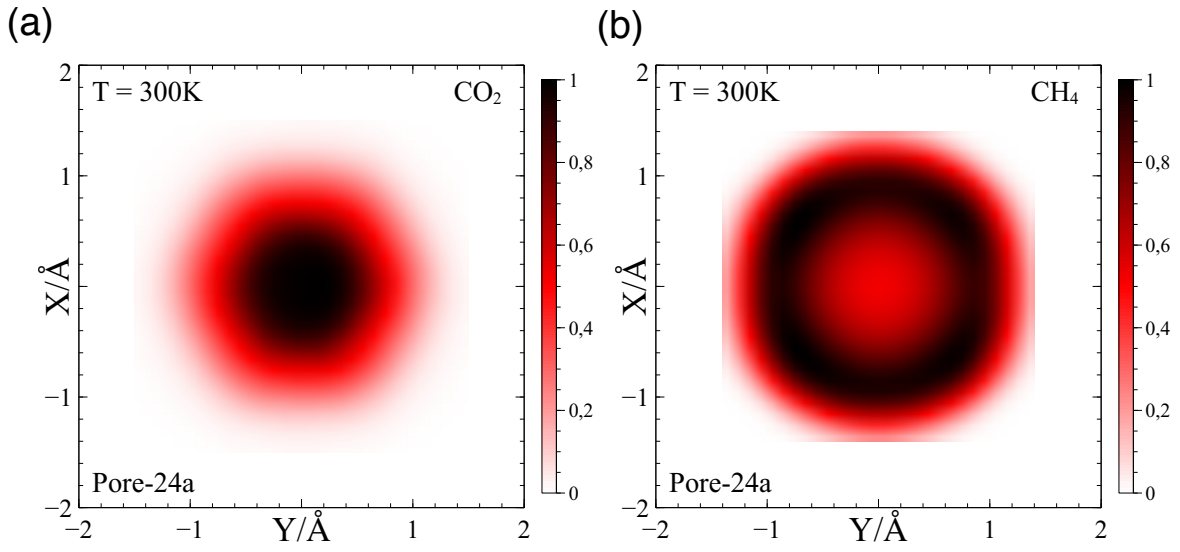

Figure 6.9: Maps of Boltzmann's factors of U_w in the plane of the pore for pure CO_2 (a) and pure CH_4 (b).

plane of the membrane, which means that $U_w = 0$. Thus, the mixing has no effect on U_w for Pore-24a. Furthermore, we observed that the influence on U_∞ is not significant. This is because we computed the PMF profiles along the trajectory corresponding to the most favorable path through the membrane. For sufficient small pore sizes, such as Pore-13a and Pore-16a, the most favorable path coincides with the trajectory crossing the center of the pore. In such cases, CO_2 and CH_4 have the same favorable path and the influence of mixing on U_∞ is obvious. For Pore-24a, Figure 6.9 shows the maps of Boltzmann's factors of U_w in the plane of the pore for CO_2 and CH_4 respectively. We observe that the most favorable paths for CO_2 and CH_4 are different. The most favorable path for CO_2 is in the center of the pore, while the most favorable path for CH_4 is towards the edges of the pore. As a result, the presence of CO_2 molecules has less influence on adsorption of CH_4 at the minimum of PMF.

With PMF profiles computed from gas mixtures, we can obtain model predictions of the cross transport coefficient of CO_2 and CH_4 in CO_2/CH_4 mixtures. The theoretical model of cross transport coefficient in gas mixtures is expressed as:

$$\Lambda_{cross}^{mix} = \frac{\bar{v}}{4}\,\phi^{mix}\,\Gamma^{mix}. \tag{6.9}$$

In equation 6.9, ϕ^{mix} and Γ^{mix} can be deduced from similar expressions as those provided for pure compound in chapter 3. The only difference is that we need to replace U_∞^{pure} and U_w^{pure} by

U_∞^{mix} and U_w^{mix}. ϕ^{mix} and Γ^{mix} are defined as:

$$\phi^{mix} = \frac{1}{HW}\int\int dxdy \exp\left(-\frac{U_w^{mix}(x,y)}{kT}\right) \quad ; \quad \Gamma^{mix} = \exp\left(\frac{U_\infty^{mix}}{kT}\right) . \tag{6.10}$$

With our definition of Λ_{cross}^{mix}, we can obtain model predictions of separation factor by the definition as:

$$(fs^{mix})_{model} = \frac{P_{des}^a}{P_{des}^b}(fs_{cross}^{mix})_{model} \tag{6.11}$$

where the expression of $fs_{cross}^{mix}model$ is shown as:

$$(fs_{cross}^{mix})_{model} = \frac{(\Lambda_{cross}^{mix^a})_{model}}{(\Lambda_{cross}^{mix^b})_{model}} \tag{6.12}$$

With non ideal gas mixtures, we assume that the mixing does not change the permeation regime nor the probability of desorption as mentioned above. We thus use the P_{des} computed from simulations of pure compound and the value of P_{des}^a/P_{des}^b can be found in Figure 6.1. In Figure 6.10 (b), we show the results obtained for Pore-16a. We observe better model predictions of separation factors with PMF profiles obtained in gas mixtures than the separation factor deduced from pure gas simulation results. For Pore-16a, the permeation of CO_2 and CH_4 is in the molecular sieving regime. As $P_{des}^{CO_2} \approx P_{des}^{CH_4} \approx 1$, we observed $fs^{mix}model \approx fs_{cross}^{mix}model$. For Pore-24a, we observed that our theoretical model underestimates the separation factor at low temperature. It is possible that we overestimate the accessible porosity of CH_4 under such conditions. Indeed, the presence of CO_2 molecules can selectively adsorbed in the center of the pore, then decrease the accessible porosity of CH_4. Under such conditions, it is not sufficient to replace U_∞^{pure} and U_w^{pure} by U_∞^{mix} and U_w^{mix}. Further studies are needed to investigate the 2D PMF profiles in the plane of the pore.

For Pore-13a, we observe the same behavior as for Pore-16a. As mentioned in chapter 3, we cannot obtain accurate values of U_w for Pore-13a due to no sufficient gas molecules crossing the pore. Nevertheless, based on the results obtained for Pore-16a, we consider that $U_w^{pure} \approx U_w^{mix}$ for Pore-13a. As the permeation of gas mixtures is still in the molecular sieving regime, we can predict the separation factor with $(fs_{cross}^{mix})_{model}$ even though we don't have comparable simulation results. As shown in Figure 6.10 (a), a high selectivity with an order of 100 can be predicted.

Table 6.1 summarizes the predictability of our theoretical model for gas mixtures with respect to the pore size. In our work, we could obtain a direct prediction of selectivity for most cases. However, for CO_2/CH_4 mixtures close to the critical temperature of CO_2, our model is only semi-predictive, as we have to simulate the mixture to compute the input parameters of the model.

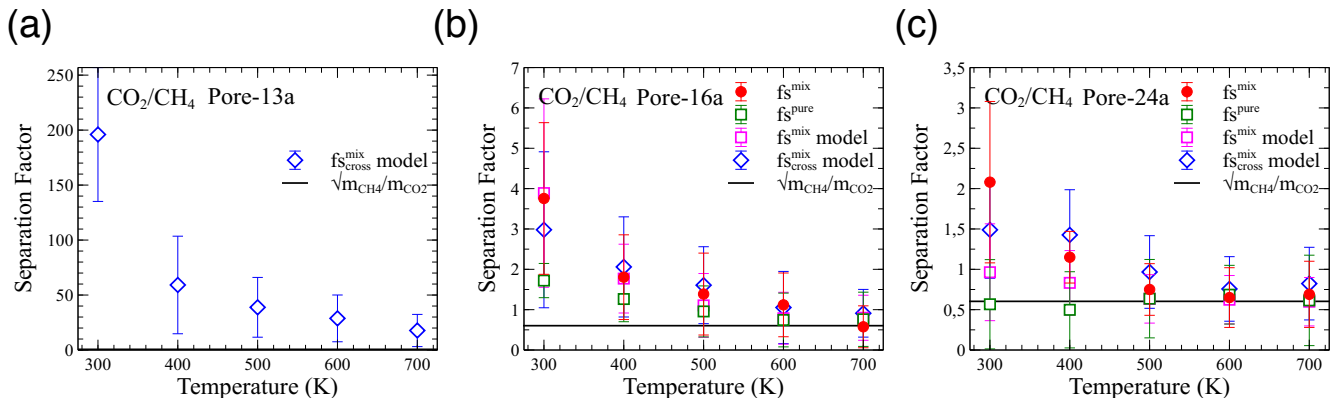

Figure 6.10: Simulation and model predictions of separation factor for CO_2/CH_4 with Pore-13a (a), Pore-16a (b) and Pore-24a (c).

$Gas\ Mixtures - Pore$	$13a$	$16a$	$24a$
CO_2/CH_4	semi-predictive	semi-predictive	semi-predictive
O_2/N_2	predictive	predictive	predictive
$O_2/N_2 - UA$	predictive	predictive	predictive

Table 6.1: Summary of theoretical models for gas mixtures with a range of pore sizes.

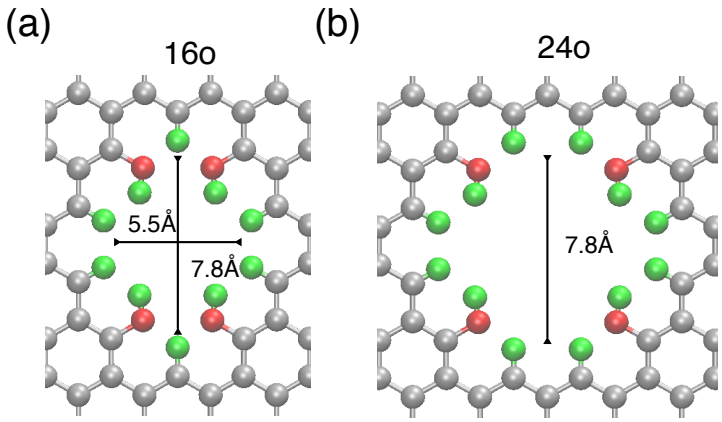

Figure 6.11: Zoomed in view of the Pore-16o (a) and Pore-24o (b) in the xy-plane.

6.4 Influence of Pore Functionalization on Separation

In graphene fabrication process, graphene oxide is considered as one of the most important derivatives of graphene[56]. It can be massively produced in tons via wet chemistry methods and can be assembled through various approaches to form laminar membranes with tailorable performance[183]. In gas separation process, several studies[146, 87] have reported the influence of pore oxide functionalization. In our work, we previously showed that for the separation of O_2/N_2 mixtures, the selectivity of hydrogen-terminated pore was not significant even with a small pore size (Pore-13a). For CO_2/CH_4 mixtures, we can obtain a high selectivity with an order of 100 but the permeability of CO_2 is low. It is necessary to improve the performance of separations for CO_2/CH_4 and O_2/N_2 mixtures. Thus, we designed two types of pores, mentioned as Pore-16o and Pore-24o (see Figure 6.11), each of which contains four hydroxyl groups substituting to four hydrogen atoms. Force field parameters for the hydroxyl groups residing at the edge of the graphene nanopores were approximated by DREIDING force field[162]. With Pore-16o and Pore-24o, we performed NEMD simulations with equimolar O_2/N_2 and CO_2/CH_4 mixtures, respectively.

Figure 6.12 reports the influence of pore functionalization. For O_2/N_2 mixtures, we observe that the transport coefficients of O_2 with Pore-16o and Pore-13a have similar values. Nevertheless, the separation factor with Pore-16o is two times larger than with Pore-13a. For CO_2/CH_4 mixture, we observe an even more interesting behavior. The transport coefficient of CO_2 with Pore-24o is larger than Pore-16a, meanwhile, a significant increase of separation factor is observed with Pore-24o, especially at low temperature. It means that the pore functionalization can improve the trade-off between selectivity and permeability of hydrogen-terminated nanoporous

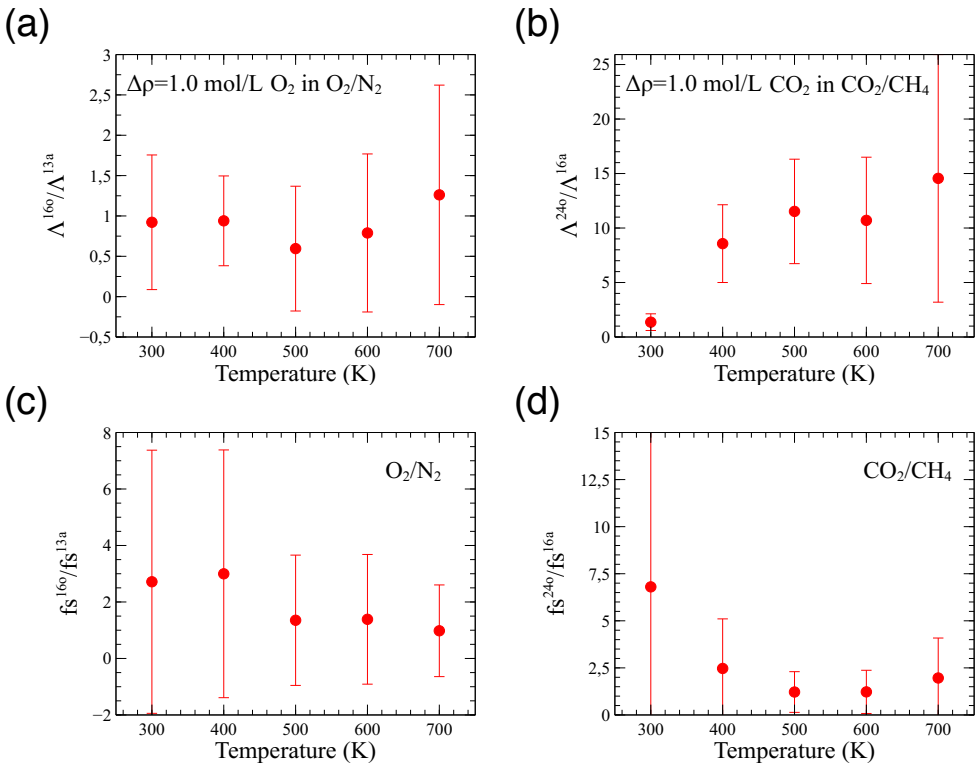

Figure 6.12: (a) Ratio of Λ between Pore-16o and Pore-13a for O_2 in O_2/N_2 mixture. (b) Ratio of Λ between Pore-24o and Pore-16a for CO_2 in CO_2/CH_4 mixture. (c) Ratio of separation factor between Pore-16o and Pore-13a for O_2/N_2 mixture. (d) Ratio of separation factor between Pore-24o and Pore-16a for CO_2/CH_4 mixture.

graphene membranes.

6.5 Robeson Plots

Figure 6.13 is the Robeson plot for CO_2/CH_4 and O_2/N_2 at 300K and 400K. The trade-off between permeability and selectivity with hydrogen-terminated nanoporous graphene is obvious in this plot. As mentioned above, the oxide pore functionalizations have the potential to improve this trade-off. Yuan et al[44] reported similar Robeson plots for the hydrogen-terminated pores at T=300K. In Figure 6.13 (a), we observe that they usually underestimated the separation factor. It is because they neglected the effect of mixing and dealt with CO_2/CH_4 mixtures as ideal gas mixtures. In this work, we proved that the CO_2/CH_4 mixtures behave as non ideal mixture and the mixing effect can improve the selectivity of CO_2/CH_4 gas pairs close to the critical temperature of CO_2. Even with an underestimation of selectivity, Yuan et al proved that hydrogen-terminated nanoporous graphene has better performance in CO_2/CH_4 separation than other membrane material, like Zeolites[184, 185], Silica[186, 187], Polymer[188, 189, 190, 191] and MOF[192] provided the density of pore is large enough ($10^{14}/m^2$).

6.6 Conclusion

In this chapter, we applied the theoretical model developed for pure gas to gas mixtures. With ideal gas mixtures, we proved that simulation results of pure gas can be used to estimate the selectivity of mixtures. Under such conditions, we can apply our theoretical model directly. In the molecular sieving regime, the theoretical model is fully predictive because the probability of desorption can be considered as 1. In the crossover regime, the model may be predictive if the probabilities of desorption of gas pairs are similar. If not, the model is only semi-predictive, yet it provides predictions with correct order. With non ideal gas mixtures, we cannot estimate the selectivity correctly from simulation results obtained for pure gas. Nevertheless, with the help of PMF profiles computed in gas mixtures, our model is able to reproduce the simulated separation factor. In most cases, we could obtain accurate predictions of selectivity for different gas pairs. As a conclusion, our work provides insights into the use of nanoporous 2D material with varying pore sizes for gas separation. We believe our theoretical model can be used as a guide for the design of optimum pore geometries and chemistry.

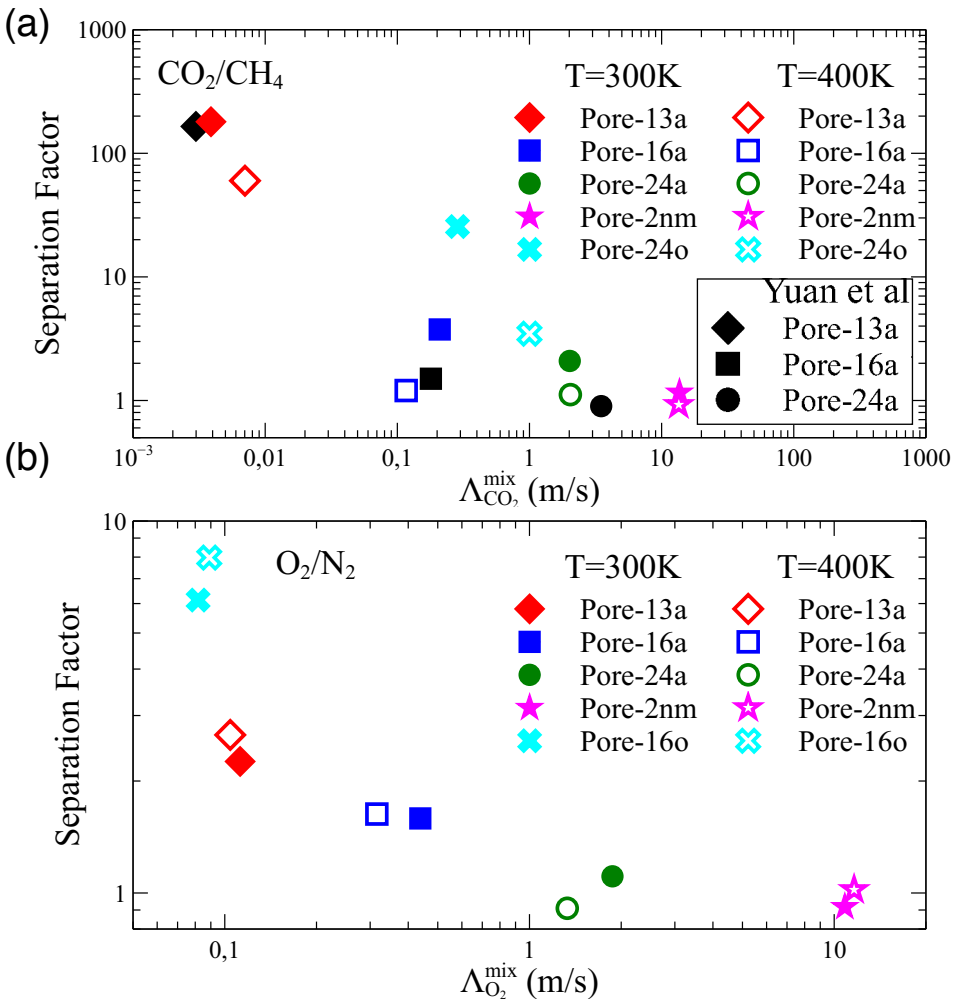

Figure 6.13: Robeson plots for CO_2/CH_4 (a) and O_2/N_2 (b) with a range of pore sizes at 300K (plain symbols) 400K (hollow symbos). The black plain symbol are the predictions of separation factors computed by Yuan et al[44]

Chapter 7

Conclusions and Perspectives

In this chapter, we provide general conclusions and comments about the work reported in this manuscript. Furthermore, perspectives and potential extensions of this work are discussed.

7.1 General Conclusions

In this work, we used molecular simulations to investigate the permeation and separation of gas through single layer nanoporous graphene membranes. We showed that gas permeation can be typically decoupled into two steps: barrier crossing and desorption from the pore mouth region. The combination of EMD and NEMD techniques allowed us to analyze the contributions of barrier crossing and desorption separately. Accounting for these two mechanisms, we proposed the following expression for the transport coefficient: $\Lambda = P_{des}\Lambda_{cross}$, where Λ_{cross} is a transport coefficient related to barrier crossing events, and P_{des} is the probability that a permeating gas molecule desorbs from the pore mouth on the downstream side of the membrane. This formalism is motivated by the results of simulations performed on simplified systems, as reported in chapter 4.

In our molecular simulations, we observed that the permeation regime continuously evolves from the molecular sieving regime (for small pore sizes) to the effusion regime (for the large pore sizes). Our simulation results show that the probability of desorption P_{des} approaches a value of 1 in the molecular sieving regime because of high energy barriers, preventing gas molecules from recrossing the membrane. Even though we did not reach the effusion regime limit in our simulations, when the pore size is several times larger than the diameter of the gas molecules, the ratio of Λ/Λ_{cross} tends to unity as the pore size increases. P_{des} can be theoretically considered as 1 in the effusion regime because the desorption process only concerns a minority of permeating molecules passing near the edge of the pore. In the crossover regime, which fills the gap between

molecular sieving and the effusion, the influence of the kinetics of desorption cannot be neglected as the repulsive energy barrier is less pronounced and gas molecules get adsorbed in the pore's plane. In this regime, P_{des} is significantly less than 1.

For gas separation, in the case of ideal gas mixture, the mixing has no effect on the permeation mechanism. The selectivities of given gas pairs can therefore be predicted from the permeances of pure compounds. In our simulations, O_2/N_2 mixtures behave as ideal gas mixtures. For CO_2/CH_4 mixtures, the mixture exhibits a non-ideal behavior when the temperature is close to the critical point of CO_2. Under such conditions, we cannot predict the selectivity from the results obtained for pure compounds.

Regarding the transport coefficient Λ, we proposed a theoretical framework to compute the value of Λ_{cross}. According to this model, Λ_{cross} depends on the PMF between a unique permeating gas molecule and membrane atoms. As for the probability of desorption, we haven't developed a theoretical model yet. To propose a theoretical framework for P_{des}, we believe that the investigation of 3D PMF on the boundaries of the pore mouth region is necessary.

Based on the formula proposed for Λ_{cross}, our model should be predictive for transport coefficients and separation factors in the molecular sieving regime ($P_{des} = 1$) as long as the dilute gas limit is valid. In the crossover regime, the theoretical framework for the transport coefficient reproduces simulation results well, provided we multiply Λ_{cross} by the value of P_{des} obtained from simulations. We may however predict the separation factors of gas mixtures in the crossover regime when both gas species exhibit similar values of P_{des}.

These results validate the proposed theoretical framework, which pertains to all permeation regimes.

7.2 General Perspectives

In the following, we list several possible extensions of this work:

1. In this wok, we have proposed a theoretical formula for the Λ_{cross}, which accounts fo the barrier crossing mechanism. We have shown that this transport coefficient is not sufficient to predict the permeance of the membrane in the crossover regime. Indeed, when the pore size is comparable to that of the permeating gas molecule, the prediction of the permeance requires an additional parameter: the probability of desorption. To model this parameter, we will investigate the PMF on the boundaries of the pore mouth region defined in chapters 4 and 5. We believe that P_{des} can be deduced from theories addressing first passage times problems.

2. Another possible extension of this work lies in the study of coupling between different driving forces. For instance, we will investigate how combining pressure and temperature gradients

might improve the performance of nanoporous graphene membranes. Depending on the mixture of interest, cooling or heating the graphene sheet may allow to increase the separation by promoting or impending adsorption near the pore while introducing thermo-diffusional separation in the reservoirs (Soret effect).

3. Moreover, as single-layer nanoporous graphene is considered as one of the most favorable membrane material in the separation process, multilayer graphene can be synthesized more economically than the single-layer material. At present, it is largely unknown how the interplay between nanopores on different layers would influence the gas permeation and separation process. Therefore, it is essential to understand the physical mechanisms of gas permeation through multilayer nanoporous graphene. It might improve the technical and industrial viability of graphene membranes.

4. In this work, our theoretical framework has been validated by molecular simulations. To further validate our theory and apply it to industrial separation processes, it is necessary to compare our results to experimental results. We will therefore look for possible collaborations with research teams specialized in nanofluidic experiments.

Finally, it is important to point out that the theoretical framework proposed in this work is not restricted to the graphene membrane. We believe that it can be used to deal with other general 2D membrane material (polymer, MOF, silicene, etc).

Appendices

A Reduced Units

In chapter 4, our simulations data are expressed in standard Lennard-Jones (LJ) reduced units [105] and dimensionless variables are written with an asterisk in superscript. As the LJ parameters of the fluid and solid particles are identical, there is no ambiguity on the units of length, σ, energy, ϵ, and mass, m. Hereafter we provide a list of the dimensionless variables used in this work:

- reduced distances, $r^* = r\sigma^{-1}$;
- reduced energies, $U^* = U\epsilon^{-1}$;
- reduced times, $t^* = t\epsilon^{1/2}m^{-1/2}\sigma^{-1}$;
- reduced number densities, $\rho^* = \rho\sigma^3$;
- reduced temperatures, $T^* = Tk\epsilon^{-1}$, where k is the Boltzmann constant;
- reduced transport coefficients, $\Lambda^* = \Lambda^*\epsilon^{-1/2}m^{1/2}$

B Design of Nanoporous Graphene by VMD/Topotools

In this work, we designed several pore sizes on graphene sheets. This work is achieved by VMD/Topotools[157]. We provide a tutorial of pore designation by VMD:

1. Start VMD. You will notice that VMD opens a terminal window, a "VMD main" window and an "OpenGL Display" window.

2. Use VMD Main$->$ Extensions $->$ Modeling $->$ Nanotube Builder to generate a pristine graphene sheet. Be aware that this builder adjusts the number of carbon atoms so that the structure is contained within the box dimensions that you have specified. Unless the box dimensions have been set to be compatible with periodic boundary conditions, the simulation box will not be periodic (but we will solve this issue later).

3. Use VMD $->$ File$->$ Save Coordinates to save the atoms coordinates to a .xyz (named "graphene-sheet.xyz" in this tutorial).

4. You can now remove the generated "molecule" from VMD. Delete it from the VMD Main window (right click on the "molecule" line and select "delete molecule").

5. Now we must determine which carbon atoms we need to remove from the pristine sheet. We must also determine which remaining carbon atoms (at the edge of the pore) will be replaced by new atoms (typically hydrogen atoms in order to replace the non covalent C-C bonds with covalent C-H bonds. However we can insert other functional groups in the future). For this task

VMD and its scripting capabilities are convenient, we describe how to do this in the following points.

6. Open the Tk Console in VMD by selecting VMD Main− > Extensions − > Tk Console. The Tk Console works a bit like the terminal in Mac OS or Linux. First, open the directory where you have saved the .xyz file (in the Tk Console, type for instance something like cd ./my-desktop/ my-graphene). In this repertory, place the VMD script file "atomselgraphene.tcl".

7. This script contains commands that will help in selecting the carbon atoms directly in the OpenGl Display of VMD. Open the "atomselgraphene.tcl" file in a text editor and take a look at the commands (see http://www.ks.uiuc.edu/Training/Tutorials/vmd/tutorial-html/node4.html for an introduction to VMD scripts). From an approximate pore radius r , it selects carbon atoms within a distance r from the center of the sheet and change their color in the graphical window. These may not be exactly the atoms we want to remove, but it will help in locating them in the sheet. Launch the script by typing the command source atomselgraphene.tcl in the Tk console.

8. We must find the indexes of the carbon atoms we want to remove in the .xyz file. To do that, select VMD Main − > Mouse − > Pick and in the OpenGL Display window click on any carbon atoms. The index of this carbon atoms will appear in the terminal window that opened when you launched VMD. Write down the index of the selected atom and save it for the next steps. Repeat for each carbon atom you want to delete.

9. In the script "atomselgraphene.tcl", there are a bunch of command lines at the end of the file written as comments. Remove the comments symbols # and insert the indexes of the deletable carbon atoms (separated by a space) in the command line set *sel_del* [*atomselect top* {*index...*}]. Then delete the "molecule" from VMD and restart the "atomselgraphene.tcl" script. This will automatically select the carbon atoms that should be replaced by hydrogens and it will output the indexes of these atoms in the Tk Console. Save all the indexes (carbons to delete and carbons to replace) for later.

10. Open the "graphenetolammps.tcl" file in a text editor. This script will generate the porous graphene sheet system and output all the topological parameters (atom types, charges, coordinates, bonds, angle, dihedrals, impropers, box dimensions) to a LAMMPS data file. Copy the indexes of the carbon atoms to delete and to replace in the command lines set *sel_del* [*atomselect top* {*index...*}] and set *sel_h* [*atomselect top index...*] respectively. This will delete the selected carbon atoms and replace the carbon atoms located at dangling bonds with hydrogen atoms. Launch the script by typing the command source graphenetolammps.tcl in the Tk console.

11. This scripts outputs a "data.perforene.txt" data file for LAMMPS. But we are not done yet ! Indeed, we have replaced some carbon atoms by hydrogens and the C-H bond length is

therefore not equilibrated (it should be different from the original C-C bond length). We must minimize the structure with LAMMPS.

12. Open the LAMMPS input script "mingraphene.in.txt". This script performs a simple energy minimization of the porous graphene sheet, with only hydrogen atoms allowed to move. Review all the commands in this script and make sure you understand their meaning. The simulations outputs a "data.perforene-min.txt" LAMMPS data file with the minimized structure and all the relevant topology parameters.

13. You can use VMD and launch the "lammpstopdb.tcl" script from the Tk console. This will read the "data.perforene-min.txt" LAMMPS data file and output a "perforene.pdb" for simple visualization in VMD.

Bibliography

[1] Mariolino Carta. *Gas Separation*, pages 1–3. Springer Berlin Heidelberg, Berlin, Heidelberg, 2015.

[2] David S Sholl and Ryan P Lively. Seven chemical separations to change the world. *Nature*, 532(7600):435–437, 2016.

[3] Anton A Kiss. Distillation technology–still young and full of breakthrough opportunities. *Journal of Chemical Technology & Biotechnology*, 89(4):479–498, 2014.

[4] Henry Z Kister. Distillation design mcgraw-hill. *Boston, USA*, 1992.

[5] Henry Z Kister, PM Mathias, DE Steinmeyer, WR Penney, BB Crocker, and JR Fair. *Equipment for distillation, gas absorption, phase dispersion, and phase separation*. McGraw-Hill, 2008.

[6] Anton A Kiss. *Advanced distillation technologies: design, control and applications*. John Wiley & Sons, 2013.

[7] DC Freshwater. Thermal economy in distillation. *Trans. Inst. Chem. Eng.*, 29:149–160, 1951.

[8] Ross Taylor and Rajamani Krishna. *Multicomponent mass transfer*, volume 2. John Wiley & Sons, 1993.

[9] Gelein De Koeijer and Signe Kjelstrup. Application of irreversible thermodynamics to distillation. *International Journal of Thermodynamics*, 7(3):107–114, 2004.

[10] Felix B Petlyuk. *Distillation theory and its application to optimal design of separation units*. Cambridge University Press, 2004.

[11] K Sampathkumar, TV Arjunan, P Pitchandi, and P Senthilkumar. Active solar distillation—a detailed review. *Renewable and sustainable energy reviews*, 14(6):1503–1526, 2010.

[12] Carsten Buchaly, Peter Kreis, and Andrzej Górak. Hybrid separation processes—combination of reactive distillation with membrane separation. *Chemical Engineering and Processing: Process Intensification*, 46(9):790–799, 2007.

[13] Armin D Ebner and James A Ritter. State-of-the-art adsorption and membrane separation processes for carbon dioxide production from carbon dioxide emitting industries. *Separation Science and Technology*, 44(6):1273–1421, 2009.

[14] Juan de Riva, Jos,àö© Suarez-Reyes, Daniel Moreno, Ismael D,àö,â†az, V,àö,â†ctor Ferro, and Jos,àö© Palomar. Ionic liquids for post-combustion co2 capture by physical absorption: Thermodynamic, kinetic and process analysis. *International Journal of Greenhouse Gas Control*, 61:61 – 70, 2017.

[15] Duong D Do et al. *Adsorption analysis: equilibria and kinetics*, volume 2. Imperial college press London, 1998.

[16] Barry Crittenden and W John Thomas. *Adsorption technology and design*. Elsevier, 1998.

[17] Orhan Talu. Needs, status, techniques and problems with binary gas adsorption experiments. *Advances in Colloid and Interface Science*, 76:227–269, 1998.

[18] Jürgen U Keller and Reiner Staudt. *Gas adsorption equilibria: experimental methods and adsorptive isotherms*. Springer Science & Business Media, 2005.

[19] Phillip C Wankat. *Separation process engineering*. Pearson Education, 2006.

[20] Carlos A Grande. Advances in pressure swing adsorption for gas separation. *ISRN Chemical Engineering*, 2012, 2012.

[21] T Valdés-Solıs, MJG Linders, F Kapteijn, GBFA Marban, and AB Fuertes. Adsorption and breakthrough performance of carbon-coated ceramic monoliths at low concentration of n-butane. *Chemical engineering science*, 59(13):2791–2800, 2004.

[22] Andreas B Gorbach, Matthias Stegmaier, Gerhart Eigenberger, Jochen Hammer, and Hans-Gerhard Fritz. Compact pressure swing adsorption processes-impact and potential of new-type adsorbent-polymer monoliths. *Adsorption*, 11(1):515–520, 2005.

[23] Carlos A Grande, Simone Cavenati, Patrick Barcia, Jochen Hammer, Hans G Fritz, and Alírio E Rodrigues. Adsorption of propane and propylene in zeolite 4a honeycomb monolith. *Chemical Engineering Science*, 61(10):3053–3067, 2006.

[24] Indra Perdana, Derek Creaser, I Made Bendiyasa, Boma Wikan Tyoso, et al. Modelling nox adsorption in a thin nazsm-5 film supported on a cordierite monolith. *Chemical engineering science*, 62(15):3882–3893, 2007.

[25] Fateme Rezaei and Paul Webley. Optimum structured adsorbents for gas separation processes. *Chemical Engineering Science*, 64(24):5182–5191, 2009.

[26] Xiuwu Liu, Li Zhou, Xin Fu, Yan Sun, Wei Su, and Yaping Zhou. Adsorption and regeneration study of the mesoporous adsorbent sba-15 adapted to the capture/separation of co2 and ch4. *Chemical Engineering Science*, 62(4):1101–1110, 2007.

[27] Douglas M Ruthven and FSKKS Pressure. Swing adsorption. *New York: VCH Publishers*, 1(994):235, 1994.

[28] Daniel Tondeur and Phillip C Wankat. Gas purification by pressure swing adsorption. *Separation and Purification Methods*, 14(2):157–212, 1985.

[29] Jeong-Geun Jee, Min-Bae Kim, and Chang-Ha Lee. Adsorption characteristics of hydrogen mixtures in a layered bed: binary, ternary, and five-component mixtures. *Industrial & engineering chemistry research*, 40(3):868–878, 2001.

[30] S Sircar and TC Golden. Purification of hydrogen by pressure swing adsorption. *Separation Science and Technology*, 35(5):667–687, 2000.

[31] KT Chue, JN Kim, YJ Yoo, SH Cho, and RT Yang. Comparison of activated carbon and zeolite 13x for co2 recovery from flue gas by pressure swing adsorption. *Industrial & Engineering Chemistry Research*, 34(2):591–598, 1995.

[32] Jong-Ho Park, Hee-Tae Beum, Jong-Nam Kim, and Soon-Haeng Cho. Numerical analysis on the power consumption of the psa process for recovering co2 from flue gas. *Industrial & engineering chemistry research*, 41(16):4122–4131, 2002.

[33] Alan L Chaffee, Gregory P Knowles, Zhijian Liang, Jun Zhang, Penny Xiao, and Paul A Webley. Co2 capture by adsorption: materials and process development. *International journal of greenhouse gas control*, 1(1):11–18, 2007.

[34] Yaping Lü, Shain-Jer Doong, and Martin Bülow. Pressure-swing adsorption using layered adsorbent beds with different adsorption properties: Ii—experimental investigation. *Adsorption*, 10(4):267–275, 2005.

[35] JC Santos, AF Portugal, FD Magalhaes, and A Mendes. Optimization of medical psa units for oxygen production. *Industrial & engineering chemistry research*, 45(3):1085–1096, 2006.

[36] Kent S Knaebel and Herbert E Reinhold. Landfill gas: from rubbish to resource. *Adsorption*, 9(1):87–94, 2003.

[37] Carlos A Grande and Alírio E Rodrigues. Biogas to fuel by vacuum pressure swing adsorption i. behavior of equilibrium and kinetic-based adsorbents. *Industrial & engineering chemistry research*, 46(13):4595–4605, 2007.

[38] Carlos A Grande and Richard Blom. Utilization of dual-psa technology for natural gas upgrading and integrated co2 capture. *Energy Procedia*, 26:2–14, 2012.

[39] Paola Bernardo, Enrico Drioli, and G Golemme. Membrane gas separation: a review/state of the art. *Industrial & engineering chemistry research*, 48(10):4638–4663, 2009.

[40] FM Dautzenberg and M Mukherjee. Process intensification using multifunctional reactors. *Chemical Engineering Science*, 56(2):251–267, 2001.

[41] Richard W Baker. Future directions of membrane gas separation technology. *Industrial & engineering chemistry research*, 41(6):1393–1411, 2002.

[42] H Strathmann. Membrane separation processes: current relevance and future opportunities. *AIChE journal*, 47(5):1077–1087, 2001.

[43] Tuong-Van Nguyen and Silvio de Oliveira Júnior. System evaluation of offshore platforms with gas liquefaction processes. *Energy*, 144:594–606, 2018.

[44] Zhe Yuan, Ananth Govind Rajan, Rahul Prasanna Misra, Lee W Drahushuk, Kumar Varoon Agrawal, Michael S Strano, and Daniel Blankschtein. Mechanism and prediction of gas permeation through sub-nanometer graphene pores: comparison of theory and simulation. *ACS nano*, 11(8):7974–7987, 2017.

[45] Lloyd M Robeson. Correlation of separation factor versus permeability for polymeric membranes. *Journal of membrane science*, 62(2):165–185, 1991.

[46] Lloyd M Robeson. The upper bound revisited. *Journal of membrane science*, 320(1-2):390–400, 2008.

[47] Zhenxia Zhao, Xiaoli Ma, Alexandra Kasik, Zhong Li, and YS Lin. Gas separation properties of metal organic framework (mof-5) membranes. *Industrial & Engineering Chemistry Research*, 52(3):1102–1108, 2013.

[48] Salman Shahid and Kitty Nijmeijer. Performance and plasticization behavior of polymer–mof membranes for gas separation at elevated pressures. *Journal of membrane science*, 470:166–177, 2014.

[49] Zhen-An Qiao, Song-Hai Chai, Kimberly Nelson, Zhonghe Bi, Jihua Chen, Shannon M Mahurin, Xiang Zhu, and Sheng Dai. Polymeric molecular sieve membranes via in situ cross-linking of non-porous polymer membrane templates. *Nature Communications*, 5(1):1–8, 2014.

[50] Yuri Yampolskii. Polymeric gas separation membranes. *Macromolecules*, 45(8):3298–3311, 2012.

[51] Toshihiro Tomita, Kunio Nakayama, and Hitoshi Sakai. Gas separation characteristics of ddr type zeolite membrane. *Microporous and Mesoporous Materials*, 68(1-3):71–75, 2004.

[52] Katsuki Kusakabe, Takahiro Kuroda, Atsushi Murata, and Shigeharu Morooka. Formation of a y-type zeolite membrane on a porous α-alumina tube for gas separation. *Industrial & engineering chemistry research*, 36(3):649–655, 1997.

[53] Hiroyuki Suda and Kenji Haraya. Gas permeation through micropores of carbon molecular sieve membranes derived from kapton polyimide. *The Journal of Physical Chemistry B*, 101(20):3988–3994, 1997.

[54] Joachim Petersen, Masaji Matsuda, and Kenji Haraya. Capillary carbon molecular sieve membranes derived from kapton for high temperature gas separation. *Journal of membrane science*, 131(1-2):85–94, 1997.

[55] Pei Shi Tin, Tai-Shung Chung, and Anita J Hill. Advanced fabrication of carbon molecular sieve membranes by nonsolvent pretreatment of precursor polymers. *Industrial & engineering chemistry research*, 43(20):6476–6483, 2004.

[56] Tieshan Yang, Han Lin, Xiaorui Zheng, Kian Ping Loh, and Baohua Jia. Tailoring pores in graphene-based materials: from generation to applications. *J. Mater. Chem. A*, 5:16537–16558, 2017.

[57] A. K. Geim. Graphene: Status and prospects. *Science*, 324(5934):1530–1534, 2009.

[58] Annalisa Fasolino, JH Los, and Mikhail I Katsnelson. Intrinsic ripples in graphene. *Nature materials*, 6(11):858–861, 2007.

[59] Konstantin S Novoselov, VI Fal, L Colombo, PR Gellert, MG Schwab, K Kim, et al. A roadmap for graphene. *nature*, 490(7419):192–200, 2012.

[60] Yanwu Zhu, Shanthi Murali, Weiwei Cai, Xuesong Li, Ji Won Suk, Jeffrey R Potts, and Rodney S Ruoff. Graphene and graphene oxide: synthesis, properties, and applications. *Advanced materials*, 22(35):3906–3924, 2010.

[61] Tapas Kuila, Saswata Bose, Partha Khanra, Ananta Kumar Mishra, Nam Hoon Kim, and Joong Hee Lee. Recent advances in graphene-based biosensors. *Biosensors and Bioelectronics*, 26(12):4637 – 4648, 2011.

[62] SV Morozov, KS Novoselov, MI Katsnelson, F Schedin, DC Elias, John A Jaszczak, and AK Geim. Giant intrinsic carrier mobilities in graphene and its bilayer. *Physical review letters*, 100(1):016602, 2008.

[63] Jian-Hao Chen, Chaun Jang, Shudong Xiao, Masa Ishigami, and Michael S Fuhrer. Intrinsic and extrinsic performance limits of graphene devices on sio 2. *Nature nanotechnology*, 3(4):206–209, 2008.

[64] Caterina Soldano, Ather Mahmood, and Erik Dujardin. Production, properties and potential of graphene. *Carbon*, 48(8):2127–2150, 2010.

[65] Kian Ping Loh, Qiaoliang Bao, Priscilla Kailian Ang, and Jiaxiang Yang. The chemistry of graphene. *Journal of Materials Chemistry*, 20(12):2277–2289, 2010.

[66] J Scott Bunch, Scott S Verbridge, Jonathan S Alden, Arend M Van Der Zande, Jeevak M Parpia, Harold G Craighead, and Paul L McEuen. Impermeable atomic membranes from graphene sheets. *Nano letters*, 8(8):2458–2462, 2008.

[67] Masa Ishigami, JH Chen, WG Cullen, MS Fuhrer, and ED Williams. Atomic structure of graphene on sio2. *Nano letters*, 7(6):1643–1648, 2007.

[68] Alfonso Reina, Xiaoting Jia, John Ho, Daniel Nezich, Hyungbin Son, Vladimir Bulovic, Mildred S Dresselhaus, and Jing Kong*. Layer area, few-layer graphene films on arbitrary substrates by chemical vapor deposition. *Nano letters*, 9(8):3087–3087, 2009.

[69] Goki Eda, Giovanni Fanchini, and Manish Chhowalla. Large-area ultrathin films of reduced graphene oxide as a transparent and flexible electronic material. *Nature nanotechnology*, 3(5):270–274, 2008.

[70] Michael D Fischbein and Marija Drndić. Electron beam nanosculpting of suspended graphene sheets. *Applied physics letters*, 93(11):113107, 2008.

[71] D Fox, A O'Neill, D Zhou, M Boese, JN Coleman, and HZ Zhang. Nitrogen assisted etching of graphene layers in a scanning electron microscope. *Applied Physics Letters*, 98(24):243117, 2011.

[72] Kemal Celebi, Jakob Buchheim, Roman M Wyss, Amirhossein Droudian, Patrick Gasser, Ivan Shorubalko, Jeong-Il Kye, Changho Lee, and Hyung Gyu Park. Ultimate permeation across atomically thin porous graphene. *Science*, 344(6181):289–292, 2014.

[73] Steven P Koenig, Luda Wang, John Pellegrino, and J Scott Bunch. Selective molecular sieving through porous graphene. *Nature nanotechnology*, 7(11):728, 2012.

[74] Sean C O'Hern, Michael SH Boutilier, Juan-Carlos Idrobo, Yi Song, Jing Kong, Tahar Laoui, Muataz Atieh, and Rohit Karnik. Selective ionic transport through tunable sub-nanometer pores in single-layer graphene membranes. *Nano letters*, 14(3):1234–1241, 2014.

[75] Sumedh P Surwade, Sergei N Smirnov, Ivan V Vlassiouk, Raymond R Unocic, Gabriel M Veith, Sheng Dai, and Shannon M Mahurin. Water desalination using nanoporous single-layer graphene. *Nature nanotechnology*, 10(5):459–464, 2015.

[76] Marco Bieri, Matthias Treier, Jinming Cai, Kamel Aït-Mansour, Pascal Ruffieux, Oliver Gröning, Pierangelo Gröning, Marcel Kastler, Ralph Rieger, Xinliang Feng, et al. Porous graphenes: two-dimensional polymer synthesis with atomic precision. *Chemical communications*, pages 6919–6921, 2009.

[77] Zhuangjun Fan, Qiankun Zhao, Tianyou Li, Jun Yan, Yueming Ren, Jing Feng, and Tong Wei. Easy synthesis of porous graphene nanosheets and their use in supercapacitors. *Carbon*, 50(4):1699–1703, 2012.

[78] Wenjing Yuan, Ji Chen, and Gaoquan Shi. Nanoporous graphene materials. *Materials Today*, 17(2):77–85, 2014.

[79] PengTao Xu, JiXiang Yang, KeSai Wang, Zhen Zhou, and PanWen Shen. Porous graphene: properties, preparation, and potential applications. *Chinese science bulletin*, 57(23):2948–2955, 2012.

[80] De-en Jiang, Valentino R Cooper, and Sheng Dai. Porous graphene as the ultimate membrane for gas separation. *Nano letters*, 9(12):4019–4024, 2009.

[81] Andreas W Hauser and Peter Schwerdtfeger. Methane-selective nanoporous graphene membranes for gas purification. *Physical Chemistry Chemical Physics*, 14(38):13292–13298, 2012.

[82] Hongjun Liu, Sheng Dai, and De-en Jiang. Insights into co 2/n 2 separation through nanoporous graphene from molecular dynamics. *Nanoscale*, 5(20):9984–9987, 2013.

[83] Huailiang Du, Jingyuan Li, Jing Zhang, Gang Su, Xiaoyi Li, and Yuliang Zhao. Separation of hydrogen and nitrogen gases with porous graphene membrane. *The Journal of Physical Chemistry C*, 115(47):23261–23266, 2011.

[84] Andreas W Hauser, Joshua Schrier, and Peter Schwerdtfeger. Helium tunneling through nitrogen-functionalized graphene pores: pressure-and temperature-driven approaches to isotope separation. *The Journal of Physical Chemistry C*, 116(19):10819–10827, 2012.

[85] Andreas W Hauser and Peter Schwerdtfeger. Nanoporous graphene membranes for efficient 3he/4he separation. *The journal of physical chemistry letters*, 3(2):209–213, 2012.

[86] J. Zhao, G. He, S. Huang, L. F. Villalobos, M. Dakhchoune, H. Bassas, and K. V. Agrawal. Etching gas-sieving nanopores in single-layer graphene with an angstrom precision for high-performance gas mixture separation. *Science Advances*, 5(1), 2019.

[87] Chengzhen Sun, Michael SH Boutilier, Harold Au, Pietro Poesio, Bofeng Bai, Rohit Karnik, and Nicolas G Hadjiconstantinou. Mechanisms of molecular permeation through nanoporous graphene membranes. *Langmuir*, 30(2):675–682, 2014.

[88] J.M. Smith, H.C. Van Ness, and M. Abbott. *Introduction to Chemical Engineering Thermodynamics*. CHEMICAL ENGINEERING SERIES. McGraw-Hill Education, 2005.

[89] Stanley I Sandler. *Chemical, biochemical, and engineering thermodynamics*. John Wiley & Sons, 2017.

[90] Bruce E Poling, John M Prausnitz, John P O'connell, et al. *The properties of gases and liquids*, volume 5. Mcgraw-hill New York, 2001.

[91] Jan Von Plato. Boltzmann's ergodic hypothesis. *Archive for History of Exact Sciences*, 42(1):71–89, 1991.

[92] David Chandler. *Introduction to modern statistical mechanics*. 1987.

[93] Edwin T Jaynes. Information theory and statistical mechanics. *Physical review*, 106(4):620, 1957.

[94] David Ruelle. *Statistical mechanics: Rigorous results*. World Scientific, 1999.

[95] John M Prausnitz, Rudiger N Lichtenthaler, and Edmundo Gomes De Azevedo. *Molecular thermodynamics of fluid-phase equilibria*. Pearson Education, 1998.

[96] Arieh Y Ben-Naim. *Statistical thermodynamics for chemists and biochemists*. Springer Science & Business Media, 2013.

[97] Lloyd L Lee. *Molecular thermodynamics of nonideal fluids*. Butterworth-Heinemann, 2016.

[98] EJ Maginn and JR Elliott. Historical perspective and current outlook for molecular dynamics as a chemical engineering tool. *Industrial & engineering chemistry research*, 49(7):3059–3078, 2010.

[99] Steve Plimpton. Fast parallel algorithms for short-range molecular dynamics. *Journal of computational physics*, 117(1):1–19, 1995.

[100] Nicholas Metropolis, Arianna W Rosenbluth, Marshall N Rosenbluth, Augusta H Teller, and Edward Teller. Equation of state calculations by fast computing machines. *The journal of chemical physics*, 21(6):1087–1092, 1953.

[101] Athanassios Z Panagiotopoulos. Monte carlo methods for phase equilibria of fluids. *Journal of Physics: Condensed Matter*, 12(3):R25, 2000.

[102] Philippe Ungerer, Véronique Lachet, and Bernard Tavitian. Applications of molecular simulation in oil and gas production and processing. *Oil & Gas Science and Technology-Revue de l'IFP*, 61(3):387–403, 2006.

[103] DJ Adams. Grand canonical ensemble monte carlo for a lennard-jones fluid. *Molecular Physics*, 29(1):307–311, 1975.

[104] Attila Malasics, Dirk Gillespie, and Dezső Boda. Simulating prescribed particle densities in the grand canonical ensemble using iterative algorithms. *The Journal of chemical physics*, 128(12):124102, 2008.

[105] Daan Frenkel and Berend Smit. *Understanding molecular simulation: from algorithms to applications*, volume 1. Elsevier, 2001.

[106] Anne Boutin, Bernard Tavitian, Alain H Fuchs, et al. Grand canonical monte carlo simulations of adsorption of mixtures of xylene molecules in faujasite zeolites. *Faraday Discussions*, 106:307–323, 1997.

[107] Franz. Mandl. *Statistical Physics*. Manchester Physics Series. Wiley, Hoboken, 2nd ed. edition.

[108] Loup Verlet. Computer "experiments" on classical fluids. i. thermodynamical properties of lennard-jones molecules. *Phys. Rev.*, 159:98–103, Jul 1967.

[109] K.E. Atkinson. *AN INTRODUCTION TO NUMERICAL ANALYSIS, 2ND ED*. Wiley India Pvt. Limited, 2008.

[110] Uri M. Ascher and Linda R. Petzold. *Computer Methods for Ordinary Differential Equations and Differential-Algebraic Equations*. Society for Industrial and Applied Mathematics, USA, 1st edition, 1998.

[111] John Charles Butcher and Nicolette Goodwin. *Numerical methods for ordinary differential equations*, volume 2. Wiley Online Library, 2008.

[112] William G. Hoover and Brad Lee Holian. Kinetic moments method for the canonical ensemble distribution. *Physics Letters A*, 211(5):253 – 257, 1996.

[113] Ratna Katiyar and Prateek Jha. Molecular simulations in drug delivery: Opportunities and challenges. *Wiley Interdisciplinary Reviews: Computational Molecular Science*, page e1358, 02 2018.

[114] Michael P Allen and Dominic J Tildesley. *Computer simulation of liquids*. Oxford university press, 2017.

[115] Aksel A Bothner-By. Nuclear magnetic resonance. applications to organic chemistry. *Journal of the American Chemical Society*, 81(18):5013–5014, 1959.

[116] Aaron Filler. The history, development and impact of computed imaging in neurological diagnosis and neurosurgery: Ct, mri, and dti. *Nature precedings*, pages 1–1, 2009.

[117] J. E. Jones and Sydney Chapman. On the determination of molecular fields. —ii. from the equation of state of a gas. *Proceedings of the Royal Society of London. Series A, Containing Papers of a Mathematical and Physical Character*, 106(738):463–477, 1924.

[118] Scott J Weiner, Peter A Kollman, David A Case, U Chandra Singh, Caterina Ghio, Guliano Alagona, Salvatore Profeta, and Paul Weiner. A new force field for molecular mechanical simulation of nucleic acids and proteins. *Journal of the American Chemical Society*, 106(3):765–784, 1984.

[119] H. A. Lorentz. Ueber die anwendung des satzes vom virial in der kinetischen theorie der gase. *Annalen der Physik*, 248(1):127–136, 1881.

[120] Ben Widom. Some topics in the theory of fluids. *The Journal of Chemical Physics*, 39(11):2808–2812, 1963.

[121] Kurt Binder. Applications of monte carlo methods to statistical physics. *Reports on Progress in Physics*, 60(5):487, 1997.

[122] Roel PA Dullens*, Dirk GAL Aarts, Willem K Kegel, and Henk NW Lekkerkerker. The widom insertion method and ordering in small hard-sphere systems. *Molecular Physics*, 103(21-23):3195–3200, 2005.

[123] An-hui Wang, Zhi-chao Zhang, and Guo-hui Li. Advances in enhanced sampling molecular dynamics simulations for biomolecules. *Chinese Journal of Chemical Physics*, 32(3):277–286, 2019.

[124] Eric Darve, David Rodríguez-Gómez, and Andrew Pohorille. Adaptive biasing force method for scalar and vector free energy calculations. *The Journal of chemical physics*, 128(14):144120, 2008.

[125] Jerome Henin, Giacomo Fiorin, Christophe Chipot, and Michael L Klein. Exploring multidimensional free energy landscapes using time-dependent biases on collective variables. *Journal of chemical theory and computation*, 6(1):35–47, 2009.

[126] Giacomo Fiorin, Michael L Klein, and Jerome Hénin. Using collective variables to drive molecular dynamics simulations. *Molecular Physics*, 111(22-23):3345–3362, 2013.

[127] Lee W Drahushuk and Michael S Strano. Mechanisms of gas permeation through single layer graphene membranes. *Langmuir*, 28(48):16671–16678, 2012.

[128] Zhe Yuan, Jesse D. Benck, Yannick Eatmon, Daniel Blankschtein, and Michael S. Strano. Stable, temperature-dependent gas mixture permeation and separation through suspended nanoporous single-layer graphene membranes. *Nano Letters*, 18(8):5057–5069, 2018. PMID: 30044919.

[129] Frank Van Swol and Grant S. Heffelfinger. Gradient-driven diffusion using dual control volume grand canonical molecular dynamics (dcv-gcmd). *MRS Proceedings*, 408:299, 1995.

[130] Pu Liu, Edward Harder, and BJ Berne. On the calculation of diffusion coefficients in confined fluids and interfaces with an application to the liquid- vapor interface of water. *The Journal of Physical Chemistry B*, 108(21):6595–6602, 2004.

[131] Daniel Duque, Pedro Tarazona, and Enrique Chacón. Diffusion at the liquid-vapor interface. *The Journal of Chemical Physics*, 128(13):134704, 2008.

[132] Alexandru Botan, Benjamin Rotenberg, Virginie Marry, Pierre Turq, and Beno^Noetinger. Hydrodynamics in clay nanopores. *The Journal of Physical Chemistry C*, 115(32):16109–16115, 2011.

[133] Hai Hoang and Guillaume Galliero. Grand canonical-like molecular dynamics simulations: Application to anisotropic mass diffusion in a nanoporous medium. *The Journal of Chemical Physics*, 136(18):184702, 2012.

[134] Rajamani Krishna and Jasper M. van Baten. In silico screening of metal-organic frameworks in separation applications. *Physical Chemistry Chemical Physics*, 13:10593–10616, 2011.

[135] Jörg Kärger, Douglas M Ruthven, and Doros N Theodorou. *Diffusion in nanoporous materials*. John Wiley & Sons, 2012.

[136] Fangqiang Zhu, Emad Tajkhorshid, and Klaus Schulten. Collective diffusion model for water permeation through microscopic channels. *Physical Review Letters*, 93:224501, 2004.

[137] Steven E. Strong and Joel D. Eaves. Atomistic hydrodynamics and the dynamical hydrophobic effect in porous graphene. *The Journal of Physical Chemistry Letters*, 7(10):1907–1912, 2016.

[138] Romain Vermorel, Fouad Oulebsir, and Guillaume Galliero. Communication: A method to compute the transport coefficient of pure fluids diffusing through planar interfaces from equilibrium molecular dynamics simulations. *The Journal of chemical physics*, 147(10):101102, 2017.

[139] J.J. Erpenbeck and W.W. Wood. Molecular dynamics techniques for hard core particles. In B. J. Berne, editor, *Statistical Mechanics B. Modern Theoretical Chemistry*. Plenum New York, 1977.

[140] David Chandler. Statistical mechanics of isomerization dynamics in liquids and the transition state approximation. *The Journal of Chemical Physics*, 68(6):2959–2970, 1978.

[141] Scott M Auerbach. Theory and simulation of jump dynamics, diffusion and phase equilibrium in nanopores. *International reviews in physical chemistry*, 19(2):155–198, 2000.

[142] Zhe Yuan, Rahul Prasanna Misra, Ananth Govind Rajan, Michael S Strano, and Daniel Blankschtein. Analytical prediction of gas permeation through graphene nanopores of varying sizes: Understanding transitions across multiple transport regimes. *ACS nano*, 13(10):11809–11824, 2019.

[143] Ziqi Tian, Shannon M Mahurin, Sheng Dai, and De-en Jiang. Ion-gated gas separation through porous graphene. *Nano letters*, 17(3):1802–1807, 2017.

[144] Fouad Oulebsir, Romain Vermorel, and Guillaume Galliero. Diffusion of supercritical fluids through single-layer nanoporous solids: Theory and molecular simulations. *Langmuir*, 34(2):561–571, 2018. PMID: 29244508.

[145] Karl-Philipp Schlichting and Dimos Poulikakos. Selective etching of graphene membrane nanopores: From molecular sieving to extreme permeance. *ACS Applied Materials & Interfaces*, 12(32):36468–36477, 2020.

[146] Fernando Vallejos-Burgos, François-Xavier Coudert, and Katsumi Kaneko. Air separation with graphene mediated by nanowindow-rim concerted motion. *Nature Communications*, 9, 12 2018.

[147] Zhe Yuan, Rahul Prasanna Misra, Ananth Govind Rajan, Michael S. Strano, and Daniel Blankschtein. Analytical prediction of gas permeation through graphene nanopores of varying sizes: Understanding transitions across multiple transport regimes. *ACS Nano*, 13(10):11809–11824, 2019.

[148] Zhe Yuan, Ananth Govind Rajan, Rahul Prasanna Misra, Lee W. Drahushuk, Kumar Varoon Agrawal, Michael S. Strano, and Daniel Blankschtein. Mechanism and prediction of gas permeation through sub-nanometer graphene pores: Comparison of theory and simulation. *ACS Nano*, 11(8):7974–7987, 2017.

[149] Fouad Oulebsir, Romain Vermorel, and Guillaume Galliero. Diffusion of supercritical fluids through single-layer nanoporous solids: Theory and molecular simulations. *Langmuir*, 34(2):561–571, 2018.

[150] David M Ford and Eduardo D Glandt. Molecular simulation study of the surface barrier effect. dilute gas limit. *The Journal of Physical Chemistry*, 99(29):11543–11549, 1995.

[151] Ernesto S. Loscar, C. Gastón Ferrara, and Tomás S. Grigera. Spinodals and critical point using short-time dynamics for a simple model of liquid. *The Journal of Chemical Physics*, 144(13):134501, 2016.

[152] Romain Vermorel, Fouad Oulebsir, and Guillaume Galliero. Communication: A method to compute the transport coefficient of pure fluids diffusing through planar interfaces from equilibrium molecular dynamics simulations. *The Journal of Chemical Physics*, 147(10):101102, 2017.

[153] Grant S. Heffelfinger and Frank van Swol. Diffusion in lennard,Äêjones fluids using dual control volume grand canonical molecular dynamics simulation (dcv,Äêgcmd). *The Journal of Chemical Physics*, 100(10):7548–7552, 1994.

[154] J. M. D. MacElroy. Nonequilibrium molecular dynamics simulation of diffusion and flow in thin microporous membranes. *The Journal of Chemical Physics*, 101(6):5274–5280, 1994.

[155] Denis J. Evans and Gary P. Morriss. Shear thickening and turbulence in simple fluids. *Phys. Rev. Lett.*, 56:2172–2175, May 1986.

[156] Yehan Tao, Qingzhong Xue, Zilong Liu, Meixia Shan, Cuicui Ling, Tiantian Wu, and Xiaofang Li. Tunable hydrogen separation in porous graphene membrane: first-principle and molecular dynamic simulation. *ACS applied materials & interfaces*, 6(11):8048–8058, 2014.

[157] William Humphrey, Andrew Dalke, and Klaus Schulten. VMD – Visual Molecular Dynamics. *Journal of Molecular Graphics*, 14:33–38, 1996.

[158] Wendy D. Cornell, Piotr Cieplak, Christopher I. Bayly, Ian R. Gould, Kenneth M. Merz, David M. Ferguson, David C. Spellmeyer, Thomas Fox, James W. Caldwell, and Peter A. Kollman. A second generation force field for the simulation of proteins, nucleic acids, and organic molecules. *Journal of the American Chemical Society*, 117(19):5179–5197, 1995.

[159] G. J. Kramer, N. P. Farragher, B. W. H. van Beest, and R. A. van Santen. Interatomic force fields for silicas, aluminophosphates, and zeolites: Derivation based on ab initio calculations. *Phys. Rev. B*, 43:5068–5080, Feb 1991.

[160] Almudena García-Sánchez, Conchi O. Ania, JoséB. Parra, David Dubbeldam, Thijs J. H. Vlugt, Rajamani Krishna, and Sofía Calero. Transferable force field for carbon dioxide adsorption in zeolites. *The Journal of Physical Chemistry C*, 113(20):8814–8820, 05 2009.

[161] H. Sun. Compass:,Äâ an ab initio force-field optimized for condensed-phase applicationsoverview with details on alkane and benzene compounds. *The Journal of Physical Chemistry B*, 102(38):7338–7364, 1998.

[162] Stephen L. Mayo, Barry D. Olafson, and William A. Goddard. Dreiding: a generic force field for molecular simulations. *The Journal of Physical Chemistry*, 94(26):8897–8909, 1990.

[163] William L Jorgensen, David S Maxwell, and Julian Tirado-Rives. Development and testing of the opls all-atom force field on conformational energetics and properties of organic liquids. *Journal of the American Chemical Society*, 118(45):11225–11236, 1996.

[164] Jeffrey J Potoff and J Ilja Siepmann. Vapor–liquid equilibria of mixtures containing alkanes, carbon dioxide, and nitrogen. *AIChE journal*, 47(7):1676–1682, 2001.

[165] Marcos E. Perez-Blanco and Edward J. Maginn. Molecular dynamics simulations of co2 at an ionic liquid interface: Adsorption, ordering, and interfacial crossing. *The Journal of Physical Chemistry B*, 114(36):11827–11837, 2010. PMID: 20687572.

[166] Ubaya Higgoda, Robert Hellmann, Thomas Koller, and Andreas Fröba. Self-diffusion coefficient and viscosity of methane and carbon dioxide via molecular dynamics simulations based on new ab initio-derived force fields. *Fluid Phase Equilibria*, 481, 10 2018.

[167] M. Krishnamurthy, Sohail Murad, and J. Olson. Molecular dynamics simulation of henry's constant of argon, nitrogen, methane and oxygen in ethylene oxide. *Molecular Simulation - MOL SIMULAT*, 32:11–16, 01 2006.

[168] Luda Wang, Lee W Drahushuk, Lauren Cantley, Steven P Koenig, Xinghui Liu, John Pellegrino, Michael S Strano, and J Scott Bunch. Molecular valves for controlling gas phase transport made from discrete ångström-sized pores in graphene. *Nature nanotechnology*, 10(9):785, 2015.

[169] Shiqi Huang, Mostapha Dakhchoune, Wen Luo, Emad Oveisi, Guangwei He, Mojtaba Rezaei, Jing Zhao, Duncan Alexander, Andreas Züttel, Michael Strano, and Kumar Varoon Agrawal. Single-layer graphene membranes by crack-free transfer for gas mixture separation. *Nature Communications*, 9, 12 2018.

[170] Michael S. H. Boutilier, Chengzhen Sun, Sean C. O,ÄöÄôHern, Harold Au, Nicolas G. Hadjiconstantinou, and Rohit Karnik. Implications of permeation through intrinsic defects in graphene on the design of defect-tolerant membranes for gas separation. *ACS Nano*, 8(1):841–849, 2014. PMID: 24397398.

[171] Lee Drahushuk, Luda Wang, Steven Koenig, Joseph Bunch, and Michael Strano. Analysis of time-varying, stochastic gas transport through graphene membranes. *ACS nano*, 10, 12 2015.

[172] L. Mart,àö,â†nez, R. Andrade, E. G. Birgin, and J. M. Mart,àö,â†nez. Packmol: A package for building initial configurations for molecular dynamics simulations. *Journal of Computational Chemistry*, 30(13):2157–2164, 2009.

[173] Andrew I. Jewett, Zhuoyun Zhuang, and Joan-Emma Shea. Moltemplate a coarse-grained model assembly tool. *Biophysical Journal*, 104(2):169a, jan 2013.

[174] Hongjun Liu, Zhongfang Chen, Sheng Dai, and De-en Jiang. Selectivity trend of gas separation through nanoporous graphene. *Journal of Solid State Chemistry*, 224:2–6, 2015.

[175] Yong Wang, Qingyuan Yang, Jinping Li, Jiangfeng Yang, and Chongli Zhong. Exploration of nanoporous graphene membranes for the separation of n 2 from co 2: a multi-scale computational study. *Physical Chemistry Chemical Physics*, 18(12):8352–8358, 2016.

[176] Benedict Leimkuhler, Christophe Chipot, Ron Elber, Aatto Laaksonen, Alan Mark, Tamar Schlick, Christoph Schütte, and Robert Skeel. *New algorithms for macromolecular simulation*, volume 49. Springer Science & Business Media, 2006.

[177] Johannes Kästner. Umbrella sampling. *Wiley Interdisciplinary Reviews: Computational Molecular Science*, 1(6):932–942, 2011.

[178] Benny D Freeman. Basis of permeability/selectivity tradeoff relations in polymeric gas separation membranes. *Macromolecules*, 32(2):375–380, 1999.

[179] Joshua Schrier. Helium separation using porous graphene membranes. *The Journal of Physical Chemistry Letters*, 1(15):2284–2287, 2010.

[180] Stephan Blankenburg, Marco Bieri, Roman Fasel, Klaus Müllen, Carlo A Pignedoli, and Daniele Passerone. Porous graphene as an atmospheric nanofilter. *Small*, 6(20):2266–2271, 2010.

[181] Myung E Suk and Narayana R Aluru. Water transport through ultrathin graphene. *The Journal of Physical Chemistry Letters*, 1(10):1590–1594, 2010.

[182] Luda Wang, Michael SH Boutilier, Piran R Kidambi, Doojoon Jang, Nicolas G Hadjiconstantinou, and Rohit Karnik. Fundamental transport mechanisms, fabrication and potential applications of nanoporous atomically thin membranes. *Nature nanotechnology*, 12(6):509, 2017.

[183] Yang Li, Wang Zhao, Matthew Weyland, Shi Yuan, Yun Xia, Huiyuan Liu, Meipeng Jian, Jindi Yang, Christopher D Easton, Cordelia Selomulya, et al. Thermally reduced nanoporous graphene oxide membrane for desalination. *Environmental science & technology*, 53(14):8314–8323, 2019.

[184] Shiguang Li, John L. Falconer, and Richard D. Noble. Sapo-34 membranes for co2/ch4 separations: Effect of si/al ratio. *Microporous and Mesoporous Materials*, 110(2):310 – 317, 2008.

[185] Moises A. Carreon, Shiguang Li, John L. Falconer, and Richard D. Noble. Alumina-supported sapo-34 membranes for co2/ch4 separation. *Journal of the American Chemical Society*, 130(16):5412–5413, 2008. PMID: 18376813.

[186] Toshiharu Okui, Yuriko Saito, Tatsuya Okubo, and Masayoshi Sadakata. Gas permeation of porous organic/inorganic hybrid membranes. *Journal of Sol-Gel Science and Technology*, 5(2):127–134, Jan 1995.

[187] B.-K. Sea, K. Kusakabe, and S. Morooka. Pore size control and gas permeation kinetics of silica membranes by pyrolysis of phenyl-substituted ethoxysilanes with cross-flow through a porous support wall. *Journal of Membrane Science*, 130(1):41 – 52, 1997.

[188] S. Sridhar, R. Suryamurali, B. Smitha, and T.M. Aminabhavi. Development of crosslinked poly(ether-block-amide) membrane for co2/ch4 separation. *Colloids and Surfaces A: Physicochemical and Engineering Aspects*, 297(1-3):267–274, 2007.

[189] Chuigen Guo, Lin Zhou, and Jianxiong Lv. Effects of expandable graphite and modified ammonium polyphosphate on the flame-retardant and mechanical properties of wood flour-polypropylene composites. *Polymers and Polymer Composites*, 21:449–456, 09 2013.

[190] Tymen Visser, N. Masetto, and Matthias Wessling. Materials dependence of mixed gas plasticization behavior in asymmetric membranes. *Journal of membrane science*, 306(1-2):16–28, 2007.

[191] S. Sridhar, T. M. Aminabhavi, S. J. Mayor, and M. Ramakrishna. Permeation of carbon dioxide and methane gases through novel silver-incorporated thin film composite pebax membranes. *Industrial & Engineering Chemistry Research*, 46(24):8144–8151, 2007.

[192] F. Fallahi and H. Mohammadi-Manesh. Molecular dynamics simulations of carbon monoxide self-diffusion in the nanoporous of the cu-btc. *Procedia Materials Science*, 11:449 – 453, 2015. 5th International Biennial Conference on Ultrafine Grained and Nanostructured Materials, UFGNSM15.